ABSTRACT

Title of Dissertation: SPATIOTEMPORAL OPTICAL VORTICES

Scott Wesley Hancock,
Doctor of Philosophy, 2023

Dissertation directed by: Professor Howard Milchberg
Department of Physics

Light beams carrying orbital angular momentum (OAM) have become a mainstay of optical science and technology. In these beams, well-known examples of which are the Laguerre-Gaussian (LG_{pm}) and Bessel-Gaussian (BG_m) beams, the OAM vector points parallel or anti-parallel to propagation, and is associated with a phase winding $2\pi m$ in the plane transverse to the propagation direction, where integer m is the winding order or the "topological charge". Such beams can be monochromatic.

Recently, our group discovered a new type of OAM structure that naturally emerges from nonlinear self-focusing, which we dubbed the spatio-temporal optical vortex (STOV). Here, the phase winding exists in a spatiotemporal plane, with the OAM pointing transverse to propagation. In this dissertation, we extend the generation of STOV-carrying pulses to the linear regime, demonstrating their generation using a $4f$ pulse shaper and measuring their free-space propagation using a new ultrafast single-shot space- and time-resolving diagnostic, TG-SSSI (transient-grating single-shot

supercontinuum spectral interferometry). We then demonstrate that transverse OAM is a property of photons by experimentally confirming the conservation of transverse OAM in second harmonic generation. Because the field of STOVs is so new, a first principles theory for their transverse OAM was lacking. We developed such a theory for transverse OAM that predicts half integer values of OAM and the existence of a STOV polariton in dispersive media. The surprise of half-integer OAM values launched a debate in the OAM community, which has been resolved in favor of our theory by our most recent experiments. These explore how phase and amplitude perturbations can impart spatiotemporal torques to light. We find that transverse OAM can be imparted to light pulses only for (1) sufficiently fast transient phase perturbations or (2) energy removal from a pulse already possessing transverse OAM.

SPATIOTEMPORAL OPTICAL VORTICES

by

Scott Wesley Hancock

Dissertation submitted to the Faculty of the Graduate School of the
University of Maryland, College Park, in partial fulfillment
of the requirements for the degree of
Doctor of Philosophy
2023

Advisory Committee:
Professor Howard Milchberg, Chair
Professor Julius Goldhar
Professor Phillip Sprangle
Dr. Eric Rosenthal
Professor Timothy Koeth

Dedication

To Amy Yaich and Prince

Acknowledgements

The research presented in this thesis and the associated knowledge learned would not have been possible without the help, guidance, discussions, and support of many wonderful people. First, I would like to extend a special thanks to my advisor Howard Milchberg. He always goes the extra mile for his students, and he may have gone an extra mile after that for me by taking a chance on a non-traditional student with an undergraduate degree in an unrelated field. Beyond the opportunities and support Howard provided, none of this work would have been possible without the innumerable technical discussions and debates with him throughout my time here.

My journey as a non-traditional student (an undergraduate degree in economics and international affairs) would also not have been possible without Dr. Jennifer L. Burris and Dr. Brooke C. Hester, who provided me the opportunity to pursue my master's degree in engineering physics at Appalachian State University, academic guidance and research projects.

I owe special thanks Dr. Eric Rosenthal, for initially recruiting me to join the Intense Laser Matter Interactions group, and Dr. Sina Zahedpour, with whom I worked for a majority of my time in this group and whose advice, guidance and assistance was indispensable.

The discussions and help of my fellow graduate students, past and present, in the Intense Laser Matter Interactions group. Discussions with Lucas Railing and Andrew Goffin, Dr. Ilia Larkin, and now Dr. Robert Schwartz about our respective projects,

experimental hurdles, and research papers immeasurably enhanced my learning experience (and often resulted in fun but overly elaborate ideas for experiments). I would also like to thank all the other members, past and present, of Big Lab, Small Lab, New Lab, and New-New Lab, Dr. Bo Miao, Dr. Linus Feder, Dr. Daniel Woodbury, Dr. Fatholah Salehi, Dr. Anthony Zingale, Manh Le, Andrew Tartaro, Jaron Shrock and Stefan Waczynski who have also improved my experience here by sharing about their research and projects as have the rest of the group, Ela Rockafellow, Nishchal Tripathi, Michael Parker, and Frederica Liu.

Additionally, I would like to thank all the technical staff of IREAP; Shawn Fickes for his assistance in maintaining environmental control equipment in the labs, Don Schmadel for always making sure we are safe and fulfilling our environmental safety requirements and for handling various HVAC and electrical tasks in the labs, and Bryan Quinn for his tireless efforts in maintaining the energy research facility and its associated operations. I also must acknowledge Nolan Ballew and Tom Weimar for their help in the machine shop and the administrative staff of IREAP past and present, Nancy Boone, Taylor Prendergast, Dottie Brosius, Judi Gorski, Julie Johnson, Meredith Pettit, and Leslie Delabar for ensuring paperwork, travel, orders and all the other myriad details were handled. Josiland Chambers was indispensable in navigating the academic landscape.

Lastly, but certainly not least, I must acknowledge the support, assistance and patience of my wife, Amy Yaich. Without her constant encouragement, love and understanding I would not have been able to be where I am and who I am today. I also

must thank my dog, Prince, for making sure I got out and went for walks during the pandemic.

Table of Contents

List of Abbreviations

1D	One dimensional
2D	Two dimensional
3D	Three dimensional
BG	Bessel Gaussian
c.c.	Complex Conjugate
d-scan	Dispersion scan
FROG	Frequency Resolved Optical Gating
FS	Fused Silica
GDD	Group Delay Dispersion
GVD	Group Velocity Dispersion
GVM	Group Velocity Mismatch
HG	Hermite Gaussian
LG	Laguerre Gaussian
MgF_2	Magnesium Fluoride
N_2	Molecular Nitrogen
NL	Nonlinear
O_2	Molecular Oxygen
OAM	Orbital Angular Momentum
SC	Supercontinuum
SF_6	Sulfur Hexafluoride

SEA-SPIDER	Spatially Encoded Array Spectral Phase Interferometry for Direct Electric field Reconstruction
SHG	Second Harmonic Generation
SLM	Spatial Light Modulator
SPIDER	Spectral Phase Interferometry for Direct Electric field Reconstruction
SPM	Self-Phase Modulation
SSSI	Single-shot Supercontinuum Spectral Interferometry
STOV	Spatiotemporal Optical Vortex
STPWE	Space-Time Paraxial Wave Equation
STRIPED FISH	Spatially and Temporally Resolved Intensity and Phase Evaluation Device: Full Information from a Single Hologram
TG	Transient-Grating
TG-SSSI	Transient-Grating Single-shot Supercontinuum Spectral Interferometry
Xe	Xenon
XPM	Cross-Phase Modulation

Chapter 1: Introduction

1.1 Outline and Motivation

The study of light carrying longitudinal orbital angular momentum (OAM) has been an increasingly active field since it was first realized that Laguerre-Gaussian (LG_{pm}) electromagnetic modes with integer radial and azimuthal indices p and m have an OAM of $m\hbar$ per photon [1]. OAM carrying light beams such as LG_{pm} [1–4] and Bessel-Gaussian (BG_m) modes of nonzero azimuthal index m have found uses in optical trapping [5–7], super-resolution microscopy [8], generation of air waveguides using LG_{01} beams [9], and plasma waveguides using BG_m beams [10]. Other proposed uses of longitudinal OAM beams include turbulence-resilient free-space communications [11–14], quantum key distribution [15,16], and driving rotating wakefields in laser wakefield accelerators [17]. Optical vortex formation is also ubiquitously observed in the speckle pattern of randomly scattered coherent light [18] and has found other uses in plasma waveguides [19]. Other proposed uses of longitudinal OAM beams include generating large magnetic fields in intense laser-plasma interaction [20]. Note that all of these standard OAM vortices can, in principle, be supported by monochromatic beams and hence are fundamentally continuous wave (CW) phenomena. Standard OAM vortices embedded in short pulse beams [21–23], which are necessarily polychromatic, have also been experimentally and theoretically studied.

The fact that light could carry OAM oriented transverse to its propagation direction was first revealed by a high field nonlinear optics experiment [24]. In this seminal work, the transverse OAM density was carried by spatiotemporal optical vortices (STOVs). In this case, the STOVs were generated from the spatiotemporal phase shear found in filamentation and self-guiding of intense laser pulses in air [24]. STOVs form naturally in this process and moreover are necessary electromagnetics structures that control the flow of optical energy density during self-guided propagation. In fact, STOVs are a universal consequence of any arrested self-focusing process [25]. Since STOVs are carried in the spatiotemporal domain, they are necessarily polychromatic. Once it was determined that STOVs were generated by spatiotemporal phase shear, it was proposed that they could be generated linearly and controllably, using a $4f$ pulse shaper to modify the spatiospectral domain and then return the pulse to the spatiotemporal domain. [26] This technique was verified through the free-space propagation measurements of pulse-shaper-generated STOV pulses, captured by transient-grating single-shot supercontinuum spectral interferometry (TG-SSSI) [27,28], and later replicated using a scanning probe technique [29].

This dissertation presents the first demonstration of linear generation of STOVs, their free space propagation, and their orbital angular momentum dynamics. In order to perform the measurements of this thesis, a new single shot diagnostic was developed, capable of ultrafast time and space-resolved maps of a pulse's phase and amplitude, with special application to pulses with phase singularities: Transient Grating Single-

Shot Supercontinuum spectral Interferometry (TG-SSSI) [28]. This is described in Chapter 2.

In Chapter 3, we identify a class of modal solutions for STOV electromagnetic pulses propagating in dispersive media with OAM orthogonal to propagation. [30] The intrinsic OAM carried by symmetric STOVs in vacuum is half-integer and for general asymmetric STOVs in dispersive media, the OAM is quantized in integer multiples of a parameter that depends on STOV symmetry and the group velocity dispersion [30]. This result suggests that STOVs propagating in dispersive media are accompanied by a polariton-like quasiparticle. Additionally, the modal theory is compared to experimental measurements of the free space propagation of STOVs.

Linear generation of STOVs and their free-space propagation is studied experimentally and with theory and simulation in Chapter 4. These measurements and simulations demonstrate STOV mediation of space-time energy flow within the pulse and conservation of OAM in space-time.

Chapter 5 presents the first demonstration of second harmonic generation (SHG) of STOVs. This experiment demonstrates that transverse OAM is conserved in nonlinear processes and confirms that transverse OAM is a property of single photons [31].

Chapter 6 examines the effect of transient perturbations on the transverse OAM of light. Here we demonstrate the controlled transfer of transverse OAM to electromagnetic waves: the *spatiotemporal* torquing of light. This is distinctly different from the transfer of OAM to longitudinal, spatially-defined OAM light by stationary or slowly varying refractive index structures such as phase plates and turbulence. We

show that transverse OAM can be imparted to a short light pulse only for (1) sufficiently fast transient phase perturbations overlapped with the pulse in spacetime, or (2) energy removal from a pulse without flat phase fronts. Additionally, this chapter shows that the OAM theory presented in Chapter 3 correctly quantifies the light-matter interaction of this experiment and provides a torque-based explanation for the first measurement of STOVs [24].

Due to the transverse nature of the OAM carried by STOVs many of the uses found for beams with spatial OAM may not necessarily be feasible—so finding ways to fully utilize this new feature of light requires a more complete understanding of transverse OAM and its behavior. Chapter 7 summarizes the results of the previous chapters and lays out paths for future work in STOV research.

The remainder of this chapter provides technical background for the chapters that follow, including the prior pioneering work on STOVs done in this lab.

1.2 Maxwell's Equations

Electromagnetic field evolution is described by Maxwell's Equations [32],

$$\nabla \cdot \mathbf{D} = \rho, \tag{1.1a}$$

$$\nabla \cdot \mathbf{B} = 0, \tag{1.1b}$$

$$\nabla \times \mathbf{H} = \mathbf{J} + \frac{\partial \mathbf{D}}{\partial t}, \tag{1.1c}$$

$$\nabla \times \mathbf{E} = -\frac{\partial \mathbf{B}}{\partial t}, \tag{1.1d}$$

where $\mathbf{E}$ is the electric field, $\mathbf{B}$ is the magnetic field, $\mathbf{D} = \varepsilon_0\mathbf{E} + \mathbf{P}$ is the electric displacement field, $\mathbf{P}$ is the electric polarization density, $\mathbf{H} = \mu_0^{-1}\mathbf{B} - \mathbf{M}$ is the magnetic field strength, $\mathbf{M}$ is the magnetization, ε_0 is the permittivity of free space, μ_0 is the permeability of free space, $c = (\varepsilon_0\mu_0)^{-\frac{1}{2}}$ is the speed of light in vacuum, $\mathbf{J}$ is the free current density and ρ is the free charge density.

In this work, we consider linear and nonlinear propagation of electromagnetic fields in a medium that is nonmagnetic, uniform, isotropic, and dispersive, where $\mathbf{M} = 0$ and we take $\rho = 0$. Contributions from free and bound charges and currents, including plasmas and dielectric materials, are taken up by $\mathbf{P}$ and $\mathbf{J} = \partial\mathbf{P}/\partial t$. The response of dispersive media (both linear and nonlinear) is determined by $\mathbf{P}$ and $\mathbf{J}$.

1.3 Beamlike solutions to Maxwell's equations

As preparation for our later development of a spatiotemporal wave equation and its beamlike solutions, we first review the more common and well-known beamlike solutions to Maxwell's equations. Manipulation of Maxwell's equations (1.1) yields:

$$\nabla^2\mathbf{E} - \frac{1}{c^2}\frac{\partial^2\mathbf{E}}{\partial t^2} - \mu_0\frac{\partial^2\mathbf{P}}{\partial t^2} = \nabla(\nabla\cdot\mathbf{E}) + \frac{\partial\mathbf{J}}{\partial t} + \nabla\times\frac{\partial\mathbf{M}}{\partial \mathrm{t}} \quad . \tag{1.3}$$

The medium is assumed to be uniform and isotropic, so

$$\nabla^2\mathbf{E} - \frac{1}{c^2}\frac{\partial^2\mathbf{E}}{\partial t^2} - \mu_0\frac{\partial^2\mathbf{P}}{\partial t^2} = 0 \tag{1.4}$$

and

$$k^2\tilde{\mathbf{E}} = \omega^2\mu_0\varepsilon(\omega)\tilde{\mathbf{E}}, \tag{1.5}$$

in the Fourier domain, where $\varepsilon(\omega) = \varepsilon_0\big(1 + \chi(\omega)\big)$ is the dielectric function, giving the dispersion relation $k^2(\omega) = \omega^2\mu_0\varepsilon(\omega)$**.** Then given a monochromatic field ($k_0 = k(\omega_0) = \big(\omega_0^2\mu_0\varepsilon(\omega_0)\big)^{1/2}$) propagating in the z direction with spatial dependence $\mathbf{E}(\mathbf{r}, t) = \mathbf{A}(\mathbf{r})\exp(ik_0 z - i\omega_0 t) + c.c.$ and $\mathbf{r} = \{x, y, z\}$, using the dispersion relation and taking $|\partial^2\mathbf{A}/\partial z^2| \ll |i2k_0\,\partial\mathbf{A}/\partial z|$ gives

$$i2k_0\frac{\partial\mathbf{A}}{\partial z} = -\nabla_\perp^2\mathbf{A}, \tag{1.6}$$

Beamlike modal solutions to this equation in rectangular coordinates are the well-known Hermite-Gaussian (HG) modes

$$\begin{aligned} HG_{mn}(x, y, z) = {} & A_{mn}\frac{w_0}{w(z)}H_m\left(\frac{x\sqrt{2}}{w(z)}\right)H_n\left(\frac{y\sqrt{2}}{w(z)}\right) \\ & \times\exp\left(-\frac{x^2 + y^2}{w^2(z)} + ik_0\frac{x^2 + y^2}{2R(z)} - i\psi_{mn}(z)\right), \end{aligned} \tag{1.7}$$

where A_{mn} is a normalization constant, H_m is a Hermite polynomial of order m, $w(z) = w_0\sqrt{1 + (z/z_R)^2}$ is the propagation dependent beam waist, w_0 is the transverse beam waist, $R(z) = z(1 + (z_R/z)^2)$ is the radius of curvature, $\psi_{mn}(z) = (m + n + 1)\arctan(z/z_R)$ is the Gouy phase, and $z_R = k_0 w_0^2/2$ is the Rayleigh length.

In cylindrical coordinates $x = \rho\cos\phi$ and $y = \rho\sin\phi$ the same equation has Laguerre-Gaussian beamlike mode solutions

$$LG_{pm}(\rho,\phi,z) = A_{pm}\left(\frac{1}{w(z)}\right)\left(\frac{\rho\sqrt{2}}{w(z)}\right)^{|m|} L_{pm}\left(\frac{2\rho^2}{w^2(z)}\right) \times \exp\left(-\frac{\rho^2}{w^2(z)} + ik_0\frac{\rho^2}{2R(z)} + il\phi - i\psi_{pm}(z)\right), \quad (1.8)$$

where A_{pm} is a normalization constant, L_{pm} is the associated Laguerre polynomial of

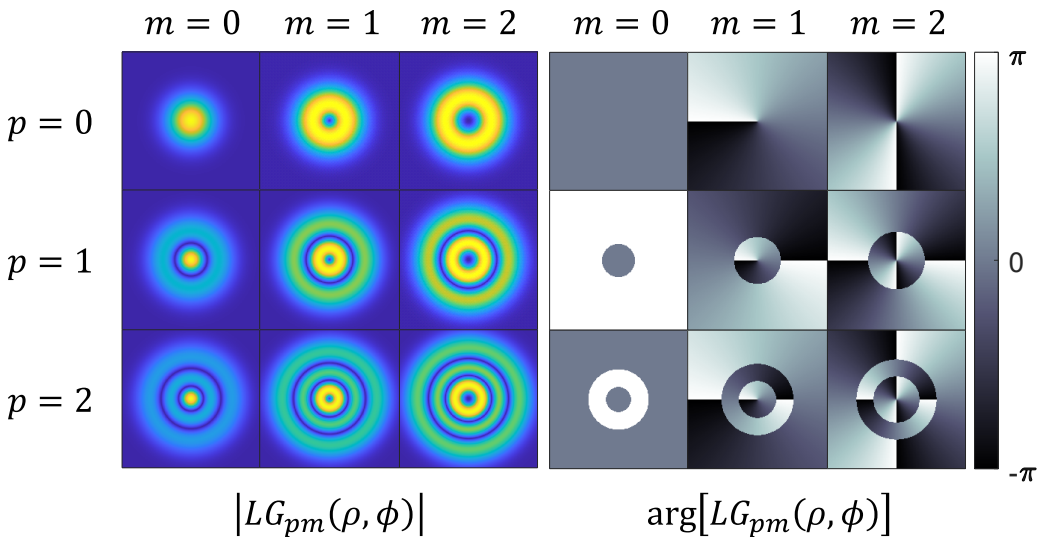

Figure 1.1 Shows the amplitudes $|LG_{pm}(\rho,\phi)|$ and phase $\arg[LG_{pm}(\rho,\phi)]$ for Laguerre-Gaussian modes of radial orders $p = 0,1,2$ and azimuthal orders $m = 0,1,2$.

radial order p and azimuthal order m, and $\psi_{pm}(z) = (|m| + 2p + 1)\arctan(z/z_R)$. Figure 1.1 shows the amplitude and phase of the first few orders of LG_{pm} modes. The plots in Fig. 1.1 for $LG_{p,|m|>0}$ show optical vortices in the transverse spatial plane where there is a discontinuity in the phase and an accompanying null in the amplitude. The

phase fronts for LG beams exhibit a screw-dislocation [33] whereas in STOV pulses, the winding is about an edge dislocation [24,34].

The Laguerre-Gaussian and Hermite-Gaussian modes each form a complete basis and can be used to decompose any paraxial field into a superposition of LG_{pm} or HG_{mn} modes [35] which will be of particular interest in Chapter 3.

1.5 Orbital Angular Momentum of Light

It was only relatively recently realized that pure LG_{pm} modes (Eq. (1.8)) carry orbital angular momentum (OAM) of $m\hbar$ per photon [1]. Computing the OAM expectation value per photon using the operator $L_z = -i\,\partial/\partial\phi$ gives, for LG_{pm} beams

$$\langle L_z \rangle = \frac{1}{U}\int \rho d\rho d\phi \; LG_{pm}^{*}\, L_z\, LG_{pm} = m, \tag{1.10}$$

Such OAM-carrying modes have found numerous uses, some of which are described in Refs. [5,6,8–12,15,17].

1.6 Nonlinear Electric Susceptibility

Here, we briefly review low order perturbative nonlinear optics in anticipation of our second harmonic generation experiment with STOV pulses. The polarization density can be separated into linear and nonlinear parts:

$$\mathbf{P} = \mathbf{P^{L}} + \mathbf{P^{NL}} = \mathbf{P}^{(1)} + \mathbf{P}^{(2)} + \mathbf{P}^{(3)} \ldots \; . \tag{1.12}$$

Fourier transforming just the time domain in Eq. (1.4), taking $\mathbf{E}(\boldsymbol{r},t) = \mathbf{A}(\boldsymbol{r},t)\exp\left(ik_q z\right)$, using the dispersion relation $k_q^2 = \omega_q^2\mu_0\varepsilon\left(\omega_q\right)$, and assuming $|\partial^2\mathbf{A}/\partial z^2| \ll \left|k_q\,\partial\mathbf{A}/\partial z\right|$ gives coupled paraxial equations

$$\frac{\partial}{\partial z}\mathbf{A} = i\frac{\omega_q^2}{2k_q\varepsilon_0 c^2}\mathbf{P}^{\boldsymbol{NL}}\left(\boldsymbol{r},\omega_q\right)\exp\left(-ik_q z\right), \tag{1.13}$$

where q is the qth frequency component of the field.

SHG was first demonstrated using a ruby (Cr:Sapphire) laser in crystalline quartz [36] and was later demonstrated for beams carrying OAM in the doubling of LG_{01} modes to LG_{02} in lithium triborate (LBO) and potassium trianyl phosphate (KTP) [37,38]. Assuming the fundamental field is y polarized, the equations describing the fundamental and second-harmonic polarization densities are

$$P_y(\omega) = \chi^{(2)}_{yxx}(-\omega;2\omega,\omega)E_x E_y^*\exp\left(i\left(k_x - k_y\right)z\right), \tag{1.14a}$$

$$P_x(\omega) = \frac{1}{2}\chi^{(2)}_{xyx}(-\omega;2\omega,\omega)E_x^2\exp\left(i2k_y z\right), \tag{1.14b}$$

The second order electric susceptibility is a rank 3 tensor and accounts for the response to two frequency components: $\chi^{(2)}_{jkl}\left(-\omega_j;\omega_k,\omega_l\right)$. While this process also gives rise to optical rectification $\chi^{(2)}_{jkl}(0;-\omega,\omega)$ used in terahertz generation [39–41] and difference frequency generation $\chi^{(2)}_{jkl}\left(-\omega_j;-\omega_k,\omega_l\right)$ used in optical parametric amplification to achieve tunable infrared (IR) wavelengths [42–44], we are primarily concerned here with sum frequency generation ($\chi^{(2)}_{jkl}\left(-\omega_j;\omega_k,\omega_l\right)$) and its special

case of second harmonic generation (SHG) $\chi^{(2)}_{jkl}(-2\omega;\omega,\omega)$, with application to the experiments of Chapter 5.

Using Eq. (1.13) the coupled amplitude equations are given by

$$\frac{\partial A_y}{\partial z} = i\frac{\omega^2}{2k_y\varepsilon_0 c}\chi^{(2)}_{yxy}A_x A_y^* \exp(-i\Delta kz), \tag{1.15a}$$

$$\frac{\partial A_x}{\partial z} = i\frac{2\omega^2}{k_x\varepsilon_0 c}\chi^{(2)}_{xyy}A_y^2 \exp(i\Delta kz), \tag{1.15b}$$

where $\Delta k = 2k_y - k_x$. From these equations, the Manley-Rowe relations [45] for SHG can be obtained, $2\frac{d}{dz}\left(\frac{I^{\omega}}{\hbar\omega}\right) = -\frac{d}{dz}\left(\frac{I^{2\omega}}{\hbar\omega}\right)$, which show that generation of one photon at 2ω requires the extinction of 2 photons at ω.

Another feature of Eq. (1.15) is the phase matching requirement $\Delta k = 0$, which can only be achieved for a limited bandwidth due to group velocity mismatch (GVM) and group velocity dispersion. The phase matching bandwidth can be found by taking $\Delta\omega = 4\ln(2)/\Delta\tau$ where $\Delta\tau = (\mathrm{GVM})L$, $\mathrm{GVM} = \partial k_y/\partial\omega\big|_{k_{y,0}} - \partial k_x/\partial\omega|_{k_{x,0}} = v_{g,y}^{-1} - v_{g,x}^{-1}$, and L is the propagation length.

The third order susceptibility is a rank 4 tensor and is the response of three input frequencies $\chi^{(3)}_{jklm}(-\omega_j;\omega_k,\omega_l,\omega_m)$. It is responsible for self-focusing in filamentation via self-phase modulation [46,47], supercontinuum generation [48] and cross-phase modulation. The latter is leveraged in measurement techniques such as single-shot supercontinuum spectral interferometry (SSSI) [49]. Self-phase modulation (SPM) is the nonlinear effect of a single field modulating its own phase while cross-phase

modulation (XPM) is the result of two or more fields (typically with slightly different center frequencies) interacting to modify the phases of the fields. In the case of self-phase modulation, the polarization for a linearly polarized field in an isotropic material is

$$P(\omega) = \varepsilon_0 \left(\chi^{(1)} + \frac{3}{4} \chi^{(3)} |E(\omega)|^2 \right) E(\omega), \tag{1.16}$$

where the degeneracy factor for SPM is ¾. We can then relate this to the total refractive index by

$$n^2 = 1 + \chi^{(1)} + \frac{3}{4} \chi^{(3)} |E(\omega)|^2 = n_0^2 + \frac{3}{4} \chi^{(3)} |E(\omega)|^2. \tag{1.17}$$

Then assuming that the linear refractive index $n_0 \gg \chi^{(3)} |E(\omega)|^2$, gives

$$n \cong n_0 + \frac{3}{8 n_0} \chi^{(3)} |E(\omega)|^2 = n_0 + \frac{3 \chi^{(3)}}{4 \varepsilon_0 n_0^2 c} I, \tag{1.18}$$

where $I = \varepsilon_0 n_0 c |E(\omega)|^2 / 2$ is the intensity and we identify

$$n_2 = \frac{3 \chi^{(3)}}{4 \varepsilon_0 n_0^2 c} I. \tag{1.19}$$

The degeneracy factor for XPM is twice that of SPM and thus the nonlinear refractive index for XPM $n_2^{\times} = 2 n_2$. It is immediately apparent that higher intensity portions of the beam accumulate more nonlinear phase, causing a self-focusing effect on the beam.

1.7 Single-Shot Supercontinuum Spectral Interferometry

Ultrafast pulses from modern mode-locked oscillators and chirped pulse amplification systems have pulse durations on the femtosecond scale, which rules out direct measurement methods such as the use of photodiodes. Instead, the nonlinear

polarization is used in characterization methods such as autocorrelators [50], frequency resolved optical gating (FROG) [51], and spectral phase interferometry for direct electric-field reconstruction (SPIDER) [52]. Single-shot supercontinuum spectral interferometry (SSSI) [49] measures the change in phase imparted on a strongly chirped supercontinuum (SC) probe $E_{probe}^{in}(t)$ by cross-phase modulation in some medium with a strong pump pulse $E_p(t)$ by spectrally interfering $E_{probe}^{out}(t)$ with a preceding unperturbed duplicate reference pulse $E_{ref}(t)$. This gives a resulting spectral interferogram

$$\left|\tilde{E}(\omega)\right|^2 = \left|\tilde{E}_{ref}(\omega)\right|^2 + \left|\tilde{E}_{probe}^{out}(\omega)\right|^2 + 2\left|\tilde{E}_{ref}(\omega)\right|\left|\tilde{E}_{probe}^{out}(\omega)\right|\cos(\Delta\phi(\omega) + \omega\tau), \tag{1.20}$$

where $\tilde{E}_{ref}(\omega)$ and $\tilde{E}_{probe}(\omega)$ are the Fourier transformations of $E_{ref}(t)$ and $E_{probe}(t)$, τ is the temporal separation of $E_{ref}(t)$ and $E_{probe}(t)$, and $\Delta\phi(\omega) = \phi_{probe}(\omega) - \phi_{ref}(\omega)$. This, along with an background interferogram $\left|\tilde{E}_0(\omega)\right|^2$, which is the same as $\left|\tilde{E}(\omega)\right|^2$ but with $\Delta\phi(\omega) = 0$, can then be used to directly compute the time dependent phase shift

$$\Delta\phi(t) = \mathrm{Im}\left[\ln\left[\frac{\mathcal{F}^{-1}\left\{\left|\tilde{E}_{probe}^{out}(\omega)\right|\exp(i\phi_F(\omega) + i\Delta\phi(\omega)\right\}}{\mathcal{F}^{-1}\left\{\left|\tilde{E}_{probe}^{in}(\omega)\right|\exp\left(i\phi(\omega)\right)\right\}}\right]\right], \tag{1.21}$$

where $\mathcal{F}^{-1}$ represents the inverse Fourier transform and $\phi_F(\omega)$ is the spectral phase. This allows for time resolved measurement of the nonlinear properties of media using a pump pulse of known energy and scale widths [53,54]. It can also be used to measure a pump pulse of unknown energy and scale widths when the nonlinear response of a

medium are known [55,56], and for the characterization of intensity envelopes in media of known nonlinear response [57].

Generation of the SC for E_{pr} and E_{ref} is typically accomplished by lens assisted filamentation of a portion of E_p in gasses with high n_2 such as Xe and SF_6. This can also be done in solids but at the cost of reduced SC energy [49].

SSSI requires knowledge of the spectral phase of E_{pr} and E_{ref}. While this could be determined using methods such as FROG or SPIDER, it is convenient to utilize the existing SSSI setup to collect shadowgrams of E_{pr} modulated by E_p at a series of known time delays, $\Delta\tau$ with respect to E_{pr}. As long as the derivative of the spectral phase $\phi_s'(\omega)$ is monotonic, then $\phi_s'(\omega_0) = \Delta\tau(\omega_0)$ is single-valued and a simple polynomial fit can be used to find the dispersion coefficients $\beta_j = (j!)^{-1}\left(\partial^j\phi/\partial\omega^j\right)\big|_{\omega_c}$, for $j > 2$ where ω_c is the center frequency and β_j is the jth order spectral phase term [58].

For implementations on laser systems with low repetition rates, obtaining shadowgrams at enough time delays to accurately recover the spectral phase of E_{pr} and E_{ref} may prove impractical. In that scenario, one may utilize the so called simplified SSSI [59], where interferometric data at only two delays are necessary (possibly one if E_{ref} and E_{pr} are sufficiently overlapped), and then employing a genetic algorithm to find where the temporal profile of the extracted change in phase is the same at both delays [59].

An example of a typical experimental setup for SSSI is shown in Fig. 1.2. This setup was used to measure the nonlinear refractive index n_2 of air constituents in the mid-far IR [56]. In this scenario, a delay stage (Fig. 1.2(b)) controls the arrival time of E_{pr}, a $\lambda/2$ waveplate (c) is used to rotate the polarization of the SC, a dichroic mirror (e) clips the NIR and higher frequencies leaving a visible SC, and a Michelson

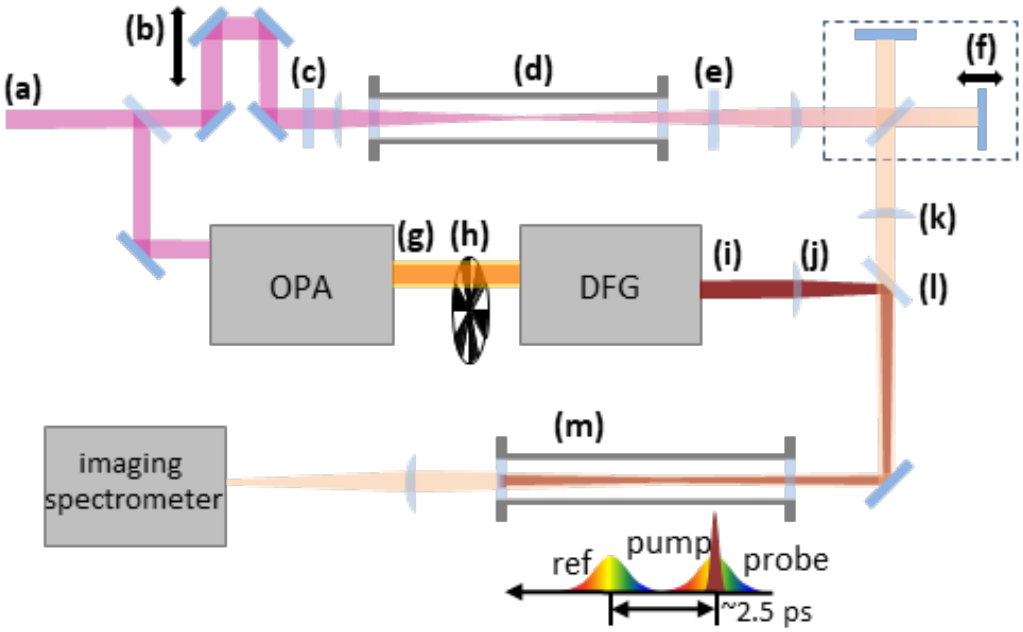

Figure 1.2. (a) Ti:Sapphire pump, ~806nm, 36fs, 10mJ; 8mJ is split and used to pump OPA; (b) delay line for timing of supercontinuum (SC) reference/probe with respect to MIR-LWIR pump pulse; (c) $\lambda/2$ plate for rotating SC polarization; (d) 2.5 atm xenon SC cell; (e) dichroic mirror, rejects 806nm pump, transmits 400nm-750nm SC pulses; (f) Twin reference and probe SC pulses separated by ~2.5ps produced by Michelson interferometer; (g) signal (1.1-1.6 μm) and idler (1.6-2.6 μm) pulses out of OPA; (h) chopper to block pump for measuring background phase; (i) MIR-LWIR pump out of DFG, (j) BaF_2 pump focusing lens (k) BK7 reference/probe SC focusing lens (l) gold dichroic mirror, transmits 400-700nm, reflects 3-12μm (m) test gas cell (up to 42 atm) with BaF2 entrance window, and fused silica exit window to absorb the pump. For each data set, the weak window response induced on the probe is measured by evacuating the cell. Each phase image is composed of 1-2×10^4 shots.

interferometer (f) is used to generate E_{pr} and E_{ref} from the SC. Then E_{pr} and E_{ref} and placed on the same beam path as E_p and XPM from E_p on E_{pr} in the target gas in (m) causes a measurable phase shift when interfering E_{ref} and E_{pr} in an imaging spectrometer, shown in Fig. 1.3.

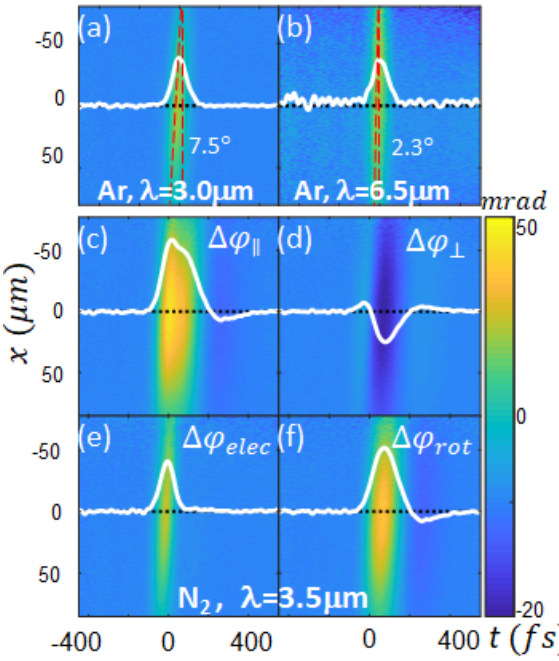

Figure 1.3. 2D spatiotemporal intensity traces from SSSI. (a) and (b): $\Delta\varphi_{elec}(x,t) \propto I(x,t)$ in Ar for pump pulses at λ=3.0μm and λ=6.5μm, showing pulse front tilt of 7.5° and 2.3°. White curves are central lineouts, with FWHM pulsewidths 77 fs and 92 fs. (c) and (d): probe phase shifts $\Delta\varphi_{\parallel}(x,t)$ and $\Delta\varphi_{\perp}(x,t)$ in N2 perpendicular and parallel to λ=3.5μm pump. (e) and (f): $\Delta\varphi_{elec}(x,t) = 3(\Delta\varphi_{\parallel}(x,t) + 2\Delta\varphi_{\perp}(x,t))/5$ (lineout FWHM = 81 fs) and $\Delta\varphi_{rot}(x,t) = 2(\Delta\varphi_{\parallel}(x,t) - 3\Delta\varphi_{\perp}(x,t))/5$ extracted from $\Delta\varphi_{\parallel}$ and $\Delta\varphi_{\perp}$.

Chapter 2: Measuring Spatiotemporal Optical Vortices

2.1 Introduction

The need to characterize ultrashort laser pulses has spawned a large and increasing number of single-shot techniques, including autocorrelation [60], multiple versions of frequency resolved optical gating (FROG) [51,61–64], spectral phase interferometry for direct electric field reconstruction (SPIDER) and related methods [52,65–69], STRIPED FISH [70], d-scan [71], plus single-shot supercontinuum spectral interferometry (SSSI) [49,58,59], and other spectral interferometry methods [72,73]. While the basic FROG and SPIDER techniques extract only the space-independent temporal amplitude and phase, more complicated techniques [69–71] have recovered the *spatiotemporal* phase and amplitude of a laser pulse in a single-shot, albeit only with single features such as pulse front tilt. STRIPED-FISH [70] and d-scan [71] methods use iterative algorithms which have not been demonstrated to converge for complicated structured light containing singularities, and SEA-SPIDER requires ancillary assumptions in determining the timing of spatial slices [69]. While SSSI does not recover the spatiotemporal phase of a pulse, it does recover the spatiotemporal pulse envelope, which has enabled measurement of ionization rates and ultrafast plasma evolution [54], electronic, vibrational, and rotational nonlinearities [53,74], as well as nonlinear refractive indices and pulse front tilt [56].

In this chapter, a new method, transient-grating single-shot supercontinuum spectral interferometry (TG-SSSI), that can measure, in a single-shot, the

spatiotemporal phase and amplitude of an ultra-fast laser pulse is presented. It was developed for recent measurements [27,30,31] of pulses embedded with spatiotemporal optical vortices (STOVs) [24] and is well suited for characterizing ultrashort laser pulses that contain singularities associated with spin/orbit angular momentum [1,21,30,75] or polarization [76].

2.2 Single-shot Supercontinuum Spectral Interferometry

We first discuss the experimental setup in the context of SSSI by examining three of the beams in Fig. 2.1(a): the "structured pulse" E_S which we want to measure, the reference pulse E_{ref}, and the probe pulse E_{pr}. Here the structured pulse has spatiotemporal phase and amplitude imposed by the zero-dispersion $4f$ pulse shaper [77–79] in Fig. 2.1(b). The reference and probe supercontinuum (SC) pulses are generated upstream of Fig. 2.1(a) by filamentation in a 2 atm SF_6 cell followed by a Michelson interferometer (not shown), with E_{ref} preceding E_{pr} by $\sim$2 ps. The transient amplitude of E_S is measured via the cross-phase modulation it induces in a spatially and temporally overlapped SC probe pulse E_{pr} in an instantaneous Kerr "witness plate," here a thin (100-500 μm) fused silica window. E_S is sufficiently weak and/or the witness plate is sufficiently thin that it does not propagate nonlinearly. (Its own phase fronts are negligibly perturbed.) The resulting spatio-spectral phase shift $\Delta\phi(x,\omega)$ imposed on the probe is extracted from interfering $E_{pr}^{out} \propto \chi^{(3)} E_S E_S^* E_{pr}^{in}$ with E_{ref} in an imaging spectrometer. Here E_{pr}^{in} and E_{pr}^{out} are the probe fields entering and exiting the witness plate, $\chi^{(3)}$ is the fused silica nonlinear susceptibility, and x is the

position within a 1D transverse spatial slice through the pump pulse at the witness plate (axes shown in Fig. 2.1). Fourier analysis of the extracted $\Delta\phi(x,\omega)$ [54] then determines the spatiotemporal phase shift $\Delta\phi(x,\tau) \propto |E_S(x,\tau)|^2 \propto I_s(x,\tau)$, yielding the 1D space + time spatiotemporal intensity envelope I_S.

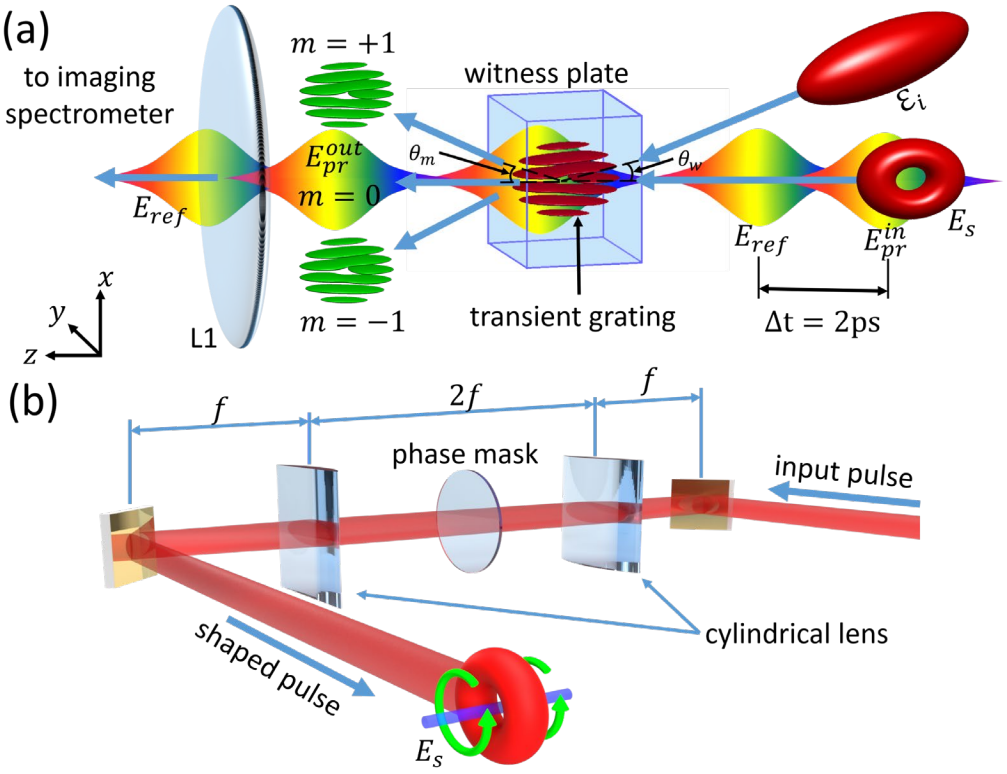

Figure 2.1. (a) Setup for transient grating single-shot spectral interferometry (TG-SSSI). The structured pulse E_S and the interferometric reference pulse $\mathcal{E}_i$ cross at angle θ_w in a fused silica witness plate, forming a transient grating. The grating is probed by a supercontinuum (SC) probe E_{pr}^{in} , preceded ~2ps earlier by a reference SC pulse E_{ref}. Imaged by L1, E_{ref} and E_{pr}^{out} interfere at an imaging spectrometer and the interferogram is analyzed in the Fourier domain, yielding a single-shot time and space resolved image of amplitude and phase of E_S. (b) $4f$ pulse shaper [77-79] for generating spatiotemporally structured pulses E_S, here STOVs [26,27,57] imposed on a 50 fs, λ=800nm input pulse. The STOV phase windings are imposed by $l = \pm 1$, and $l = -2$ spiral phase plates in the Fourier plane of the pulse shaper. The phase plates are etched on fused silica and have 16 levels (steps) every 2π.

2.3 Transient-grating Single-shot Supercontinuum Spectral Interferometry

2.3.1 Theory

Measurement of the spatiotemporal phase of E_S is enabled by the addition of an interferometric reference pulse $\mathcal{E}_i$, which is crossed with E_S at a small angle θ_i. ($\theta_w = 3.15°$ in the witness plate.) This forms a nonlinear transient refractive index grating, where $\mathcal{E}_i$ has the same center wavelength as E_S, but is bandpassed to be temporally longer while maintaining flat spectral phase. The transient grating (TG) is now the signal probed by SSSI (yielding the new method we call transient grating single-shot supercontinuum spectral interferometry [TG-SSSI]), where the output probe pulse from the witness plate becomes $E_{pr}^{out} \propto \chi^{(3)}(|E_S|^2 + |\mathcal{E}_i|^2 + E_S^*\mathcal{E}_i + E_S\mathcal{E}_i^*)E_{pr}^{in}$. A chopper on the E_S beam path (but not on the $\mathcal{E}_i$ beam path) enables to $\chi^{(3)}|\mathcal{E}_i|^2$ signal contribution to be subtracted out as background every other shot. The interference of E_{pr}^{out} and E_{ref} in the imaging spectrometer then enables extraction of $\Delta\phi(x,\omega)$, yielding $\Delta\phi(x,\tau)$ as before. We note that $\Delta\phi(x,\tau) \propto |E_S(x,\tau)|^2 + 2|E_S||\mathcal{E}_i|f(x,\tau)$, where the TG is $f(x,\tau) = \cos\left(2k_w x \sin\left(\frac{\theta_w}{2}\right) + \Delta\Phi(x,\tau)\right)$, $k_w = n_0 k$ is the central wavenumber in the witness plate, $n_0 = 1.45$, and $\Delta\Phi(x,\tau)$ is the spatiotemporal phase of E_S with respect to $\mathcal{E}_i$ (reference phase is flat in out case). In the analysis of the 2D $\Delta\phi(x,\tau)$ images, $\Delta\Phi(x,\tau)$ is extracted using standard interferometric techniques [49,80], and $I_s(x,\tau)$ is extracted using a low-pass image filter (suppressing

the sidebands imposed by the TG). Due to group velocity mismatch (GVM) in the witness plate between E_s (center wavelength $\lambda_0 = 800$ nm) and the SC probe ($\lambda_{pr} = 600$ nm), the extracted phase shift is smeared slightly in time by ~ 4 fs per 100 μm of fused silica. The temporal resolution (here ~ 7 fs) determines the shortest measurable pulse and depends on this GVM and the on the sampled bandwidth of E_{pr}. The longest measurable pulse is determined by the duration of the chirped E_{pr}, here ~ 1 ps. For weak E_S pulses, the focusing can be adjusted and/or the thickness of the witness plate can be increased. In this chapter, the minimum E_S pulse energy was 3 μJ (~ 150 GW/cm^2).

2.3.2 Experimental Setup

The laser used in the experiments is a 4 mJ/pulse, 50 fs FWHM, $\lambda_0 = 800$ nm, 1kHz Ti:sapphire system. The beam is split three ways, with ~ 100 μJ directed to SC generation (400-700 nm) for E_{pr} and E_{ref}, and a portion of the res for E_S and $\mathcal{E}_i$, whose energies were controlled using $\lambda/2$ waveplates and thin-film polarizers. The structured pulse E_S was embedded with spatiotemporal phase windings (discussed in more detail in Chapter 3) by placing $l = \pm 1$ or $l = -2$ spiral phase plates at the Fouier plane of the $4f$ pulse shaper [27,81].

As depicted in Fig. 2.1, the SC reference and probe pulses, E_{ref} and E_{pr}^{in}, are combined collinearly with the pulse E_S using a dichroic mirror, with E_S, $\mathcal{E}_i$, and E_{pr}^{in} overlapping temporally in the witness plate, while E_{ref} precedes them (by 2 ps). From

the output face of the witness plate, E_{ref} and E_{pr} were magnified and relay imaged onto the spectrometer slit using a high numerical aperture (NA) telescope with achromatic lenses. A high NA is necessary to collect the first-order diffraction ($m = \pm 1$) of E_{pr}^{out} from the TG. Achromatic imaging is essential for all SC wavelengths to in focus at the spectrometer slit and to minimize spherical aberration, which could spatially offset the diffracted orders of E_{pr}^{out} from the zero order. Background and signal data were collected at 40 Hz by placing a chopper in the bath of E_S, which enabled the subtraction of the phase shift induced by $|\mathcal{E}_i|^2$ in the witness plate.

In principle, achromatic imaging of all diffracted orders precludes the need for detailed analysis of the diffraction. However, it is interesting to note that in this experiment, only the zero order ($m = 0$) and the $m = -1$ order diffraction of the probe were observed. To understand this, the regime (Bragg or Raman-Nath) [82] of the probe diffraction was assessed by considering the dimensionless parameter $Q = 2\pi\lambda_i L/\Lambda^2\bar{n}$, where λ_i is the vacuum wavelength of incident light, Λ is the interference grating period, $\bar{n}$ is the mean refractive index, and L is the grating thickness. From Ref. [82], diffraction is in the Raman-Nath regime for $Q \leq 1$, and in the Bragg regime for $Q \gg 1$. The TG-SSSI configuration for this experiment (with a $l = 500\mu m$ fused

silica witness plate, $\Lambda(\theta_w = 3.15°) = 10\ \mu m$, $n_2 = 2.5 \times 10^{-16}\ cm^2/W$, and $\bar{n} = n_0 + n_0 n_2 I = n_0 + \Delta\phi_{TG}/kL$, where $\Delta\phi_{TG}$ is the modulated phase shift amplitude of the TG) gives $Q \cong 13.0$, which is in the Bragg regime. (Both $\Delta\phi_{TG}$ and Λ are measured values form the experiment.) This explains the observation of only one diffracted order.

This result is confirmed with simulations of scattering of E_{pr} from the nonlinear grating formed by the interference of E_s and $\mathcal{E}_i$. The simulation uses our an implementation of the unidirectional pulse propagation equation method [83,84], where all three beams intersect in the $500\mu m$ thick fused silica plate (with E_s and $\mathcal{E}_i$

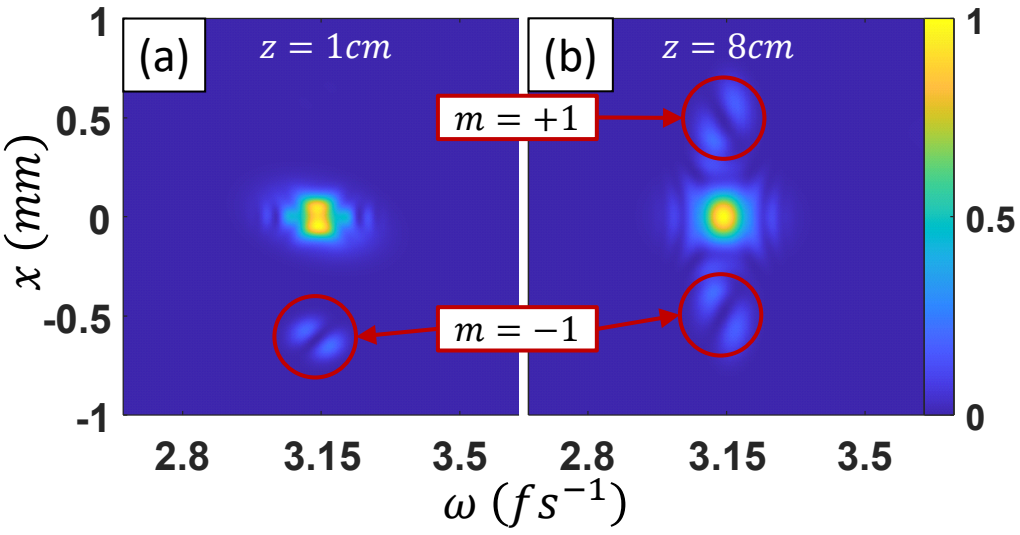

Figure 2.2. Simulated spectrally resolved scatting of SC probe pulse E_{pr} from a transient nonlinear grating in a $500\ \mu m$ thick fused silica plate, generated by interference of pulses E_s and $\mathcal{E}_i$, where z is the distance from the output face of the plate. Plotted as $|\Delta E_{pr}|^2 = |E_{pr}^{out} - E_{pr}^{in}|^2$. (a) Bragg regime transient grating: $\theta_w = 3.15°$, grating period $\Lambda = 10\ \mu m$, and $Q = 13.0$. Here the scattering is captured at $z = 1\ cm$ owing to the rapid escape of the single diffracted order ($m = -1$) from the simulation window. (b) Raman-Nath regime: $\theta_w = 0.31°$, $\Lambda = 100\ \mu m$, and $Q = 0.13$, showing $m = \pm 1$ diffracted orders.

crossing at an angle θ_w and E_{pr}^{in} normal to the surface). The beam parameters are E_s ($\lambda = 800\,nm$, 50 fs FWHM, $w_0 = 100\,\mu m$, $I_{s,peak} = 28\,GW/cm^2$, $l = +1$ STOV), $\mathcal{E}_i$ ($\lambda = 800\,nm$, $300\,fs$ FWHM, $w_0 = 300\,\mu m$, $I_{i,peak} = 28\,GW/cm^2$), and E_{pr}^{in} ($\lambda = 600\,nm$, $\Delta\lambda = 350\,nm$, $2.4\,ps$ FWHM, $w_0 = 500\,\mu m$, $GDD = 1200\,fs^2$, $TOD = 200\,fs^3$). The output electric field is numerically propagated beyond the witness plate in air and then E_s and $\mathcal{E}_i$ are spectrally filtered out, leaving the field E_{pr}^{out}. Figure 2.2 shows simulation results of probe diffraction for conditions similar to the experimental parameters ($\theta_w = 3.15°$ and $Q = 13.0$), where only the $m = -1$ diffraction order is present (Bragg regime), agreeing with the experiments. As a comparison, the crossing angle for Fig. 2.2 was chosen to be $\theta_w = 0.31°$, giving $Q = 0.13$, in the Raman-Nath regime, and the $m = \pm 1$ orders are both present. Note that the TG-SSSI setup used could be adjusted to operate in the Raman-Nath regime by increasing the grating period Λ (to $\Lambda \geq \sqrt{2\pi\lambda_i L/\bar{n}}$), but increasing the intensity of E_s or $\mathcal{E}_i$ to increase n_1 could result in non-negligible plasma formation in the witness plate and refractive distortion of E_{pr}.

Additionally, the crossing angle of $\mathcal{E}_i$ with respect to E_s, θ_w, will result in the measured TG outpacing the measured intensity envelope in time. The temporal offset of the TG with respect to the intensity envelope given by $\Delta\tau = \left(\frac{1}{v_{\text{off}}} - \frac{1}{v_{\text{g}}}\right) L$, where v_g is the group velocity of E_s in the witness plate, L is the thickness of the witness plate and $v_{\text{off}} = v_{\text{g}}(1 + \sin\theta_w)$. The best strategy to minimize this effect is of course to minimize the angle θ_w, and/or minimize the witness plate thickness.

2.3.3 Data Processing

The steps used for processing the interferograms are outlined in Fig. 2.3 and go as: SSSI extraction, separation of TG and intensity envelope, extraction of spatiotemporal phase from the measured TG. Figure 2.3(a) shows an example of a raw TG-SSSI interferogram frame recorded on the imaging spectrometer camera (Allied Vision Prosilica GT 2750). Here the pulse shaper generates E_s as a $l = -2$ STOV pulse [24,27]. The vertical spectral fringe spacing is set by the Michelson-imposed time delay between the E_{ref} and E_{pr}^{out} pulses. The 2D phase shift $\Delta\phi(x,\omega)$ is extracted in the same way as that of all other SSSI interferograms [49,58], yielding $\phi(x,\tau)$, as plotted in Fig. 2.3(b). The spatiotemporal pulse intensity envelope is recovered by low-pass image filtering of $\Delta\phi(x,\tau)$ to remove $f(x,\tau)$, yielding $I_s(x,\tau)$ in Fig. 2.3(c).

Extraction of the spatiotemporal phase $\Delta\Phi(x,\tau)$ is performed by Fourier analysis along x [80]:

$$\Delta\Phi(x,\tau) = \arg(\mathcal{F}_k^{-1}\{\mathcal{F}_x\{\Delta\phi(x,\tau)\}\Theta(k)\}), \tag{2.1}$$

where $\mathcal{F}_x\{\Delta\phi(x,\tau)\} = \Delta\tilde{\phi}(k,\tau)$ is the Fourier transform along x, $\mathcal{F}_k^{-1}\{\cdot\}$ is the inverse Fourier transform along k, $\Theta(k)$ is a sideband windowing and shifting ($k \to k - 2\pi/\Lambda$) function, and k is the x-component of the spatial frequency. This is shown in Figure 2.3(d) and (e). If the sideband is too close to the k-spectrum of the pulse envelope (which is centered at $k = 0$), $\Theta(k)$ cannot separate the TG from the pulse envelope. This necessitates a larger spatial sample and/or finer TG period, considerations which have informed the pump-probe beam geometry of the experiment.

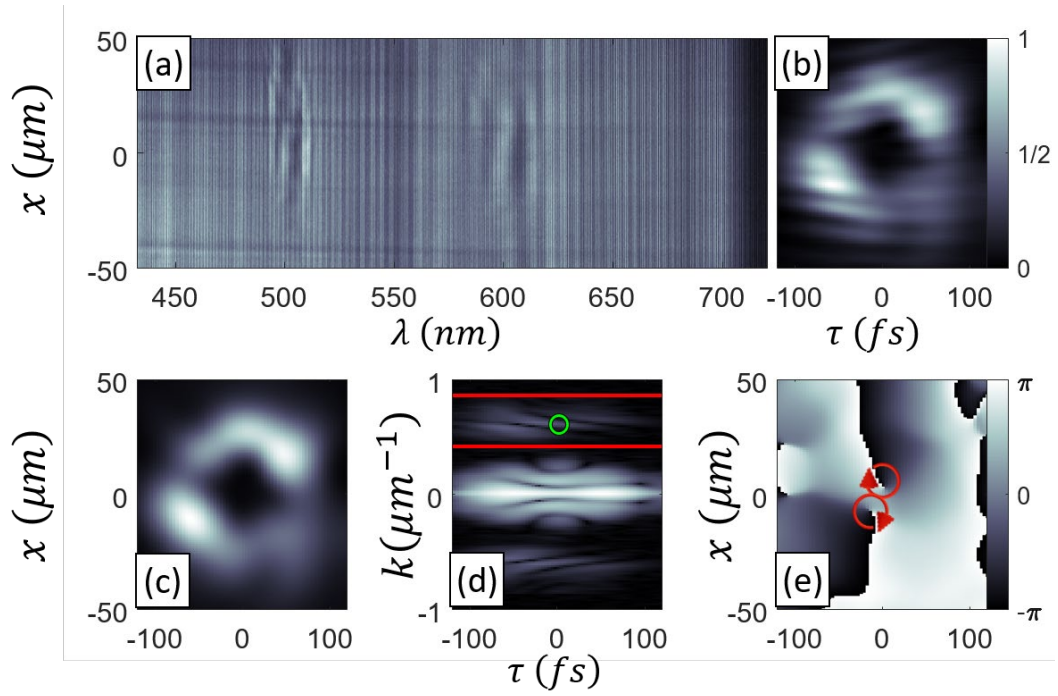

Figure 2.3. Measurement of a $l = -2$ STOV-carrying pulse (interferometric reference $\mathcal{E}_i$ at 800nm and 10nm FWHM bandwidth); **(a)** Raw 1D space-resolved spectral interferogram; **(b)** extracted $\Delta\phi(x,\tau)$; **(c)** pulse envelope $I_S(x,\tau)$ from low pass filtering of $\Delta\phi(x,\tau)$; **(d)** $\log(|\mathcal{F}_x\{\Delta\phi(x,\tau)\}| + 1)$. The red lines show the region to be spectrally windowed and the green circle identifies (k_c, τ_c) for frame averaging; **(e)** extracted spatiotemporal phase of the pulse, $\Delta\Phi(x,\tau)$.

While the single-shot signal-to-noise ratio is ~4: 1, here 500 frames are averaged to enhance it to ~80: 1. Before averaging, however, the shot-to-shot shifting of the spatial interference fringes (from mechanical vibrations in the optical setup) must be compensated. The fringes are effectively forced into common alignment by adding a constant phase $\Delta\tilde{\phi}_n(k_c,\tau_c)$ to each frame, giving

$$\Delta\Phi(x,\tau) = \arg\left(\frac{1}{N}\sum_{n=1}^{N}\mathcal{F}_k^{-1}\left\{\left[\Delta\tilde{\phi}_n(k,\tau)\exp\left(-i\Delta\tilde{\phi}(k_c,\tau_c)\right)\right]\right\}\right), \tag{2.2}$$

where $\Delta\tilde{\phi}_n(k,\tau) = \mathcal{F}_x\{\Delta\phi_n(x,\tau)\}$, $\Delta\tilde{\phi}_n(k_c,\tau_c)$ is the constant phase added to frame n to align the fringes, (k_c,τ_c) is a common point across all N frames, and $\Delta\Phi(x,\tau)$ is the mean spatiotemporal phase. The point (k_c,τ_c) is chosen at a location in the sideband where the signal is sufficiently larger than the phase noise; otherwise, each frame would be offset by a random phase factor.

2.3.4 Experimental Results

To demonstrate TG-SSSI, a $4f$ pulse shaper was used to generate (a) a Gaussian pulse ($l = 0$, no phase plate) and STOV-carrying pulses with topological charge (b) $l = +1$, (c) $l = -1$, and (d) $l = -2$, using corresponding spiral phase plates in the Fourier plane of the shaper. The columns of Fig. 2.4 show $\Delta\phi(x,\tau)$, $I_s(x,\tau)$, $f(x,\tau)$ and $\Delta\Phi(x,\tau)$ for pulses carrying $l = 0, \pm 1$, and -2. For $l = 0$, (row (a)), there is a slight fringe curvature in the TG $f(x,\tau)$, indicating a dispersion mismatch between E_s and $\mathcal{E}_i$. For the $l = \pm 1$ STOVs in rows (b) and (c), $f(x,\tau)$ clearly shows the transient fringe fusing or splitting, identifying the opposite phase windings shown in the $\Delta\Phi(x,\tau)$ column. For $l = -2$, (row (d)), one fringe in $f(x,\tau)$ splits into three at the center of the pulse. Upon phase extraction, $\Delta\Phi(x,\tau)$ has two nearby $l = -1$ phase windings rather than a single $l = -2$ winding. This is attributed to a mismatch between the ratio of the scale widths describing the phase plate phase and the ratio of the scale widths of the pulse at the Fourier plane of the shaper. Since the profile of the beam in the Fourier plane of the pulse shaper (itself dictated by the grating periodicity and focal length of the cylindrical lens) is elliptical, one of the phase plate axes should ideally be

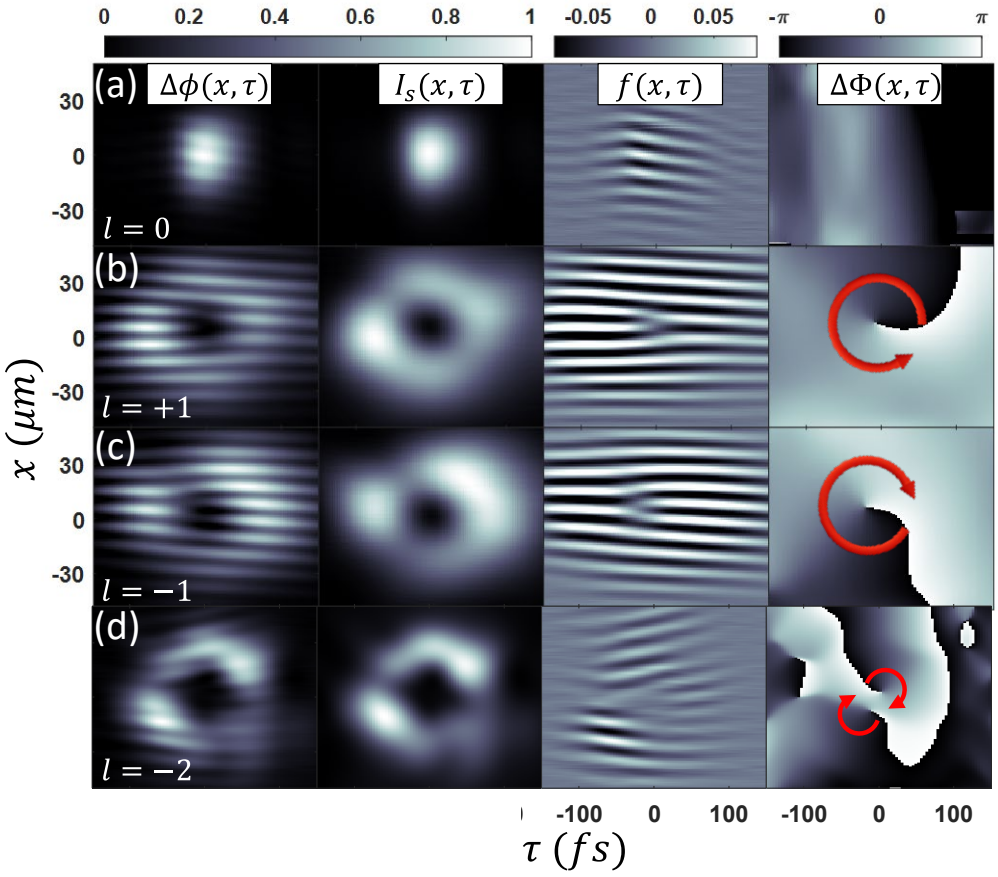

Figure 2.4. Experimental results from TG-SSSI after fringe alignment. Columns show the extracted full TG-SSSI signal $\Delta\phi(x,\tau)$, which is low-pass filtered to yield the pulse intensity envelope $I_s(x,\tau)$, or high-pass filtered to give the transient grating $f(x,\tau)$, from which the spatiotemporal phase $\Delta\Phi(x,\tau)$ is extracted. The rows show results for (a) a Gaussian pulse ($l = 0$), (b) a $l = +1$ STOV, (c) a $l = -1$ STOV, and (d) results from an $l = -2$ phase plate. The red arrows denote the direction of increasing spatiotemporal phase.

scaled to match the ellipticity of the beam. Utilization of a programmable spatial light modulator (SLM) rather than a fixed phase plate would enable scaling of the phase plate to match the beam profile, making possible the generation of $l = \pm 2$ and even higher-order STOVs.

2.3.6 2D space + 1D time TG-SSSI

For experiments where E_s is highly repetitive and highly reproducible, TG-SSSI can be extended to two spatial dimensions (x and y) by transversely scanning E_{pr}^{out} across the spectrometer entrance slit in the y-direction, as is done in $2D+1$ SSSI [54], to obtain $I_s(x,y,\tau)$ and $\Delta\Phi(x,y,\tau)$. Figure 2.5 shows $2D+1$ TG-SSSI data plotted as a surface of constant intensity, $I_s(x,y,\tau) = 1/\mathrm{e}^2$, onto which the measured phase of the pulse at the surface has been overlaid. Figure 2.5 row (a) shows a Gaussian pulse

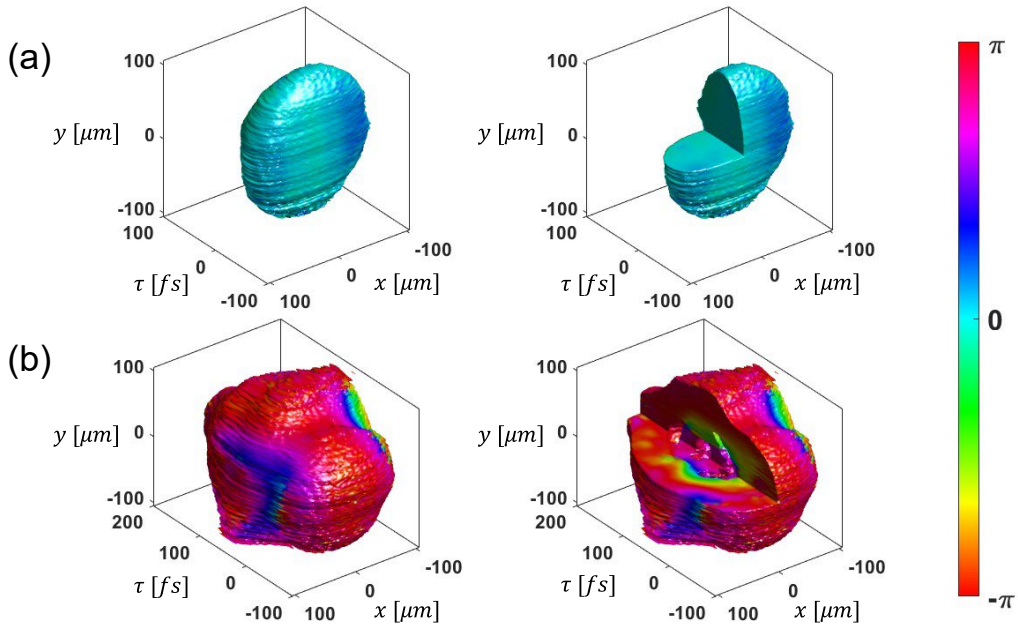

Figure 2.5. Row (a) Shows the measured 2D space + time TG-SSSI of a Gaussian pulse at an isosurface of $1/e^2$ of the intensity (right) and (left) shows the same pulse with a cutaway. Row (b) shows the same Gaussian pulse but with enough energy for it to propagate nonlinearly in a 1 mm piece of c-cut sapphire. The output of the sapphire was imaged into the witness plate of TG-SSSI (due to the use of glass lenses, only the spatial domain is imaged, while the temporal domain is distorted due to dispersion in the lenses).

(∼10μJ) and a cutaway while row (b) shows a pulse (∼20μJ) that has propagated nonlinearly in 1 mm of c-cut sapphire and accumulated a large amount of dispersion from imaging lenses and a cut away of it as well.

2.5 Conclusion

A new single-shot diagnostic for ultrashort spatiotemporally structured laser pulses has been presented, TG-SSSI, which has been used to measure simple Gaussian and STOV-carrying pulses generated by a $4f$ pulse shaper. Among multiple possible applications, TG-SSSI should prove useful in the study of nonlinear propagation, collapse, and collapse arrest of intense laser pulses in transparent media, where spatiotemporal optical pulse structures naturally emerge [24]. Additionally, a full two transverse dimension extension of TG-SSSI has been demonstrated, $2D + 1$ TG-SSSI.

Chapter 3: Mode Structure and Orbital Angular Momentum of Spatiotemporal Optical Vortices

3.1 Introduction

In the previous chapter, we presented a measurement technique capable of single-shot characterization of STOVs (TG-SSSI) however prior to applying this experimental methodology it is important to develop a theoretical basis for STOVs and their transverse OAM. In this chapter, a theoretical description of STOV-carrying pulses in both vacuum and in dispersive material media is presented, with an emphasis on their mode structure, propagation, and spatiotemporal orbital angular momentum. We find symmetric STOVs carry half-integer intrinsic transverse OAM and in dispersive media, asymmetric STOVs carry transverse OAM that depends on the STOV symmetry and the material group velocity dispersion. This material property dependence suggests the existence of a polaritonlike quasiparticle that propagates with STOVs in dispersive media. Previously, the possibility of measuring spatiotemporal vortices has been suggested [85] and dispersionless vortices have been considered in the spatiotemporal domain [86]. Recent theoretical work has also considered spatiotemporal vortex pulses, but without a full modal analysis in dispersive media [87].

3.2 Mode Structure of Spatiotemporal Optical Vortices

To begin, we look for STOV-supporting modal solutions of the paraxial wave equation. In order to account for possible medium dispersion, we use the Fourier transformed wave equation for a uniform isotropic medium with dielectric function $\varepsilon(\omega)$ and wave number given by $k^2(\omega) = \omega^2\varepsilon(\omega)/c^2$,

$$\left(\nabla_\perp^2 + \frac{\partial^2}{\partial z^2} + k^2(\omega)\right)\widetilde{\boldsymbol{\mathcal{A}}}(\mathbf{r}_\perp, z, \omega) = 0, \tag{3.1}$$

where $\widetilde{\boldsymbol{\mathcal{A}}}$ is the $t \to \omega$ Fourier-transformed vector potential, pulse propagation is along $\hat{\mathbf{z}}$, $\mathbf{r}_\perp$ represents transverse coordinates orthogonal to $\hat{\mathbf{z}}$, and $\nabla_\perp^2$ is the corresponding transverse Laplacian. We assume $\widetilde{\boldsymbol{\mathcal{A}}}(\mathbf{r}_\perp, z, \omega) = \widehat{\mathbf{A}}(\mathbf{r}_\perp, z, \omega - \omega_0)e^{ik_0 z}$, where $\widehat{\mathbf{A}}$ is a slowly varying envelope and $k_0 = k(\omega_0)$ is the wave number at the central frequency. For $k_0\left|\partial\widehat{\mathbf{A}}/\partial z\right| \gg \left|\partial^2\widehat{\mathbf{A}}/\partial z^2\right|$, this yields, $(\nabla_\perp^2 + i2k_0\,\partial/\partial z)\widehat{\mathbf{A}} + [k^2(\omega) - k_0^2]\widehat{\mathbf{A}} = 0$. Then using $k^2(\omega) - k_0^2 \approx 2k_0[k(\omega) - k_0]$ and expanding $k(\omega) = k_0 + k_0'(\omega - \omega_0) + k_0''(\omega - \omega_0)/2 + \cdots$ gives $i2k_0\,\partial\widehat{\mathbf{A}}/\partial z = -\nabla_\perp^2\widehat{\mathbf{A}} - 2k_0(k_0'\omega + k_0''\omega^2 + \cdots)\widehat{\mathbf{A}}$, where $k_0' = (\partial k/\partial\omega)_0 = v_g^{-1}$ is the inverse group velocity at ω_0, and $k_0'' = (\partial^2 k/\partial\omega^2)_0 = \left(\partial v_g^{-1}/\partial\omega\right)_0$ is the group velocity dispersion (GVD). Assuming that the pulse bandwidth is not too large ($\Delta\omega/\omega_0 \ll 1$), keeping terms in the $k(\omega)$ expansion to second order is an excellent approximation. This gives, after transforming back to the time domain, $i2k_0\,\partial\mathbf{A}/\partial z = -(\nabla_\perp^2 + i2k_0k_0'\,\partial/\partial t - k_0k_0''\,\partial^2/\partial t^2)\mathbf{A}$, where $\mathbf{A} = \mathbf{A}(\mathbf{r}_\perp, z, t)$. Finally, the substitutions, $\xi = v_g t - z$ and $\beta_2 = v_g^2 k_0 k_0''$ are made to give

$$i2k_0 \frac{\partial}{\partial z}\mathbf{A}(\mathbf{r}_\perp,\xi;z) = \left(-\nabla_\perp^2 + \beta_2 \frac{\partial^2}{\partial \xi^2}\right)\mathbf{A}(\mathbf{r}_\perp,\xi;z) = H\mathbf{A}(\mathbf{r}_\perp,\xi;z). \tag{3.2}$$

Here, ξ is a (local timelike) space coordinate in the frame of the pulse, β_2 is the dimensionless GVD, $H = (-\nabla_\perp^2 + \beta_2\,\partial^2/\partial\xi^2)$ is the spacetime propagator, and z is separated with a semicolon as it plays the role of a timelike running parameter.

Next we assume a uniformly polarized beam $\mathbf{A}(\mathbf{r}_\perp,\xi;z) = A(\mathbf{r}_\perp,\xi;z)\hat{\mathbf{e}}$, where $\hat{\mathbf{e}}$ is the complex polarization (here we take $\hat{\mathbf{e}} = \hat{\mathbf{y}}$ as in the experiments [27], where there are no effects of spin angular momentum [87]), and find modal solutions to Eq. (3.2) for $\mathbf{r}_\perp = (x,y)$:

$$A_{mpq}(x,y,\xi;z) = A^{(0)}_{mpq} u^x_m(x;z) u^y_p(y;z) u^\xi_q(\xi;z), \tag{3.3}$$

where

$$u^\xi_q(\xi;z) = \frac{C_q}{\sqrt{w_\xi(z)}} H_q\left(\frac{\sqrt{2}\xi}{w_\xi(z)}\right) e^{-\frac{\xi^2}{w^2_\xi(z)}} e^{-ik_0\frac{\xi^2}{2\beta_2 R_\xi(z)}} e^{i\left(q+\frac{1}{2}\right)\psi_\xi(z)}, \tag{3.4a}$$

and

$$u^x_m(x;z) = \frac{C_m}{\sqrt{w_x(z)}} H_m\left(\frac{\sqrt{2}x}{w_x(z)}\right) e^{-\frac{x^2}{w^2_x(z)}} e^{ik_0\frac{x^2}{2R_x(z)}} e^{-i\left(m+\frac{1}{2}\right)\psi_x(z)}. \tag{3.4b}$$

Here, $C_m = (2/\pi)^{\frac{1}{4}}(2^m m!)^{-\frac{1}{2}}$ is a normalization constant, H_m is a Hermite polynomial of order m, $w_x(z) = w_{0x}[1 + (z/z_{0x})^2]^{\frac{1}{2}}$, $R_x(z) = z[1 + (z_{0x}/z)^2]$, $\psi_x(z) = \tan^{-1}(z/z_{0x})$, and $z_{0x} = k_0 w_{0x}^2/2$ is the x-based Rayleigh range. The expression for $u^y_p(y;z)$ is identical to Eq. (3.4b) with the substitution $x \to y$ everywhere. Associated

with $u_q^{\xi}(\xi;z)$ are $z_{0\xi} = k_0 w_{0\xi}^2/2|\beta_2|$, $w_\xi(z) = w_{0\xi}\left[1+\left(z/z_{0\xi}\right)^2\right]^{\frac{1}{2}}$, $R_\xi(z) = z\left[1+\left(z_{0\xi}/z\right)^2\right]$, and $\psi_\xi(z) = \mathrm{sgn}(\beta_2)\tan^{-1}\left(z/z_{0\xi}\right)$. The quantities $w(z)$, $R(z)$, and $\psi(z)$ express the z variation in beam size, phase front curvature and Gouy phase shift as they do for standard transverse modes, except that here they also apply in the ξ domain.

The "spot sizes" w_{0x}, w_{0y}, and $w_{0\xi}$ describe the transverse space and temporal shape of the beam envelope of the lowest order mode $[(m,p,q) = (0,0,0)]$ at $z = 0$, $A_{000}(x,y,\xi;z=0) = A_{000}^{(0)} e^{-x^2/w_{0x}^2 - y^2/w_{0y}^2 - \xi^2/w_{0\xi}^2}$, which approximates the input beam to the pulse shaper. The effective wave number k_0/β_2 associated with $u_q^{\xi}(\xi;z)$ accounts for the different rate of spreading in temporal dispersion compared to transverse beam diffraction. We have allowed the beam to have elliptical envelopes in both the x-y (space) as well as x-ξ and y-ξ (spacetime) planes, and different phase curvatures in x, y, and ξ. The choice of Hermite-Gaussian (HG) basis functions for the solution of Eq (3.2) is motivated by the experimental generation of STOV-carrying pulses using a $4f$ pulse shaper [27], which imposes rectilinearly-oriented ellipticity and astigmatism in both the space and spacetime domains.

Now we consider propagation of the simplest STOV-carrying pulse generated by a pulse shaper, one with a spatiotemporal winding of topological charge $l = 1$ or $l = -1$. At $z = 0$, this pulse is constructed as

$$A_\alpha^{l=\pm 1}(x,y,\xi;z=0) = A_0\left(\frac{\xi}{w_{0\xi}} \pm i\frac{x}{w_{0x}}\right) e^{-x^2/w_{0x}^2 - y^2/w_{0y}^2 - \xi^2/w_{0\xi}^2}, \qquad (3.5)$$

where A_0 is a normalization constant.

As we will see, the spacetime eccentricity, $\alpha \equiv w_{0\xi}/w_{0x}$, is extremely important and will show up throughout these calculations. In the experiments, the y direction is orthogonal to the pulse shaper grating rulings, and so after pulse reconstruction at the shaper output, the y-dependent envelope of the input pulse is reproduced [27].

In vacuum or in the very dilute medium (air) of the experiments of [27], $\beta_2 = 0$ and $v_g = c$, $u_q^{\xi}(\xi; z=0) = C_q w_{0\xi}^{\frac{1}{2}} H_q\left(\frac{\sqrt{2}\xi}{w_{0\xi}}\right) e^{-\frac{\xi^2}{w_{0\xi}^2}}$, and Eq. (3.5) can be written as a linear combination of spacetime modes [Eqs. (3.4)] at $z = 0$:

$$A_{\alpha}^{l=\pm 1}(x, y, \xi; z=0) = u_0^{y}(y; 0)\left[u_0^{x}(x; 0)u_1^{\xi}(\xi; 0) \pm i\, u_1^{x}(x; 0)u_0^{\xi}(\xi; 0)\right]. \quad (3.6)$$

Given this initial STOV field at $z = 0$, the propagator $H = (-\nabla_{\perp}^2 + \beta_2\, \partial^2/\partial\xi^2)$ of Eq. (3.2) generates the full z-dependent evolution,

$$A_{\alpha}^{l=\pm 1}(x, y, \xi; z) = A_0 u_0^{y}(y; z)\left[u_0^{x}(x; z)u_1^{\xi}(\xi; z) \pm i\, u_1^{x}(x; z)u_0^{\xi}(\xi; z)\right]. \quad (3.7)$$

For the case $w_{0x} = w_{0\xi}$, ($\alpha = 1$), the factor $u_0^{x}(x; z)u_1^{\xi}(\xi; z) \pm i\, u_1^{x}(x; z)u_0^{\xi}(\xi; z)$ is analogous to the superposition of the 0th and 1st order Hermite-Gaussian (HG) transverse modes (HG_0 and HG_1) to give the Laguerre-Gaussian (LG) spatial mode $\mathrm{LG}_{\mathrm{space}}^{0\pm 1} = \mathrm{HG}_0(x)\mathrm{HG}_1(y) \pm i\, \mathrm{HG}_1(x)\mathrm{HG}_0(y)$.

Figure 3.1 compares theory and experiment, where Fig. 3.1(a) shows the amplitude and phase of $A_{\alpha}^{l=\pm 1}(x, y = 0, \xi; z)$ from $z = -0.85 z_{0x}$ to $z = 0.24 z_{0x}$, computed with Eq (3.7). It is seen that the field is a donut at the beam waist ($z = 0$)(as constructed) and evolves into spatiotemporally offset lobes with opposite spacetime tilt on either

side of $z = 0$, with transverse diffractive spreading widening the beam. Here, we have used $\alpha = w_{0\xi}/w_{0x} = 0.3$ to match the measured eccentricity. The experimental results are shown in Fig. 3.1(b). To capture the in-flight amplitude and phase profiles of these pulsed spatiotemporal structures, we have employed transient-grating single-shot supercontinuum spectral interferometry (TG-SSSI) which was discussed in Chapter 2 and described in [28]. The measurements are in excellent agreement with our mode-based calculation, capturing the STOV field's evolution from a donut into spatiotemporally offset lobes, and matching the phase winding in each panel.

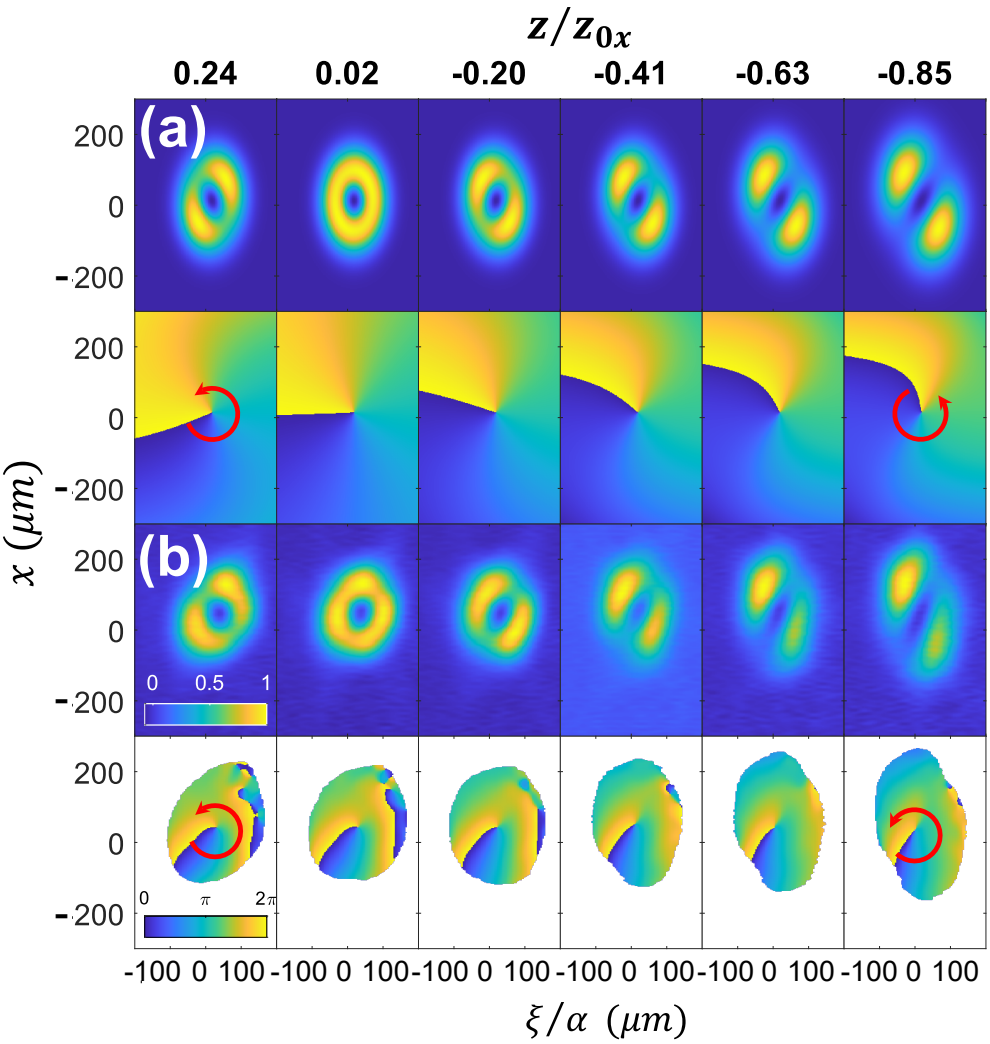

Figure 3.1. (a) Propagation evolution from $z/z_{0x} = -0.85$ to 0.24 of the $l = 1$ STOV $A(x, y = 0, \xi; z)_{(l=+1)}$, plotted using the modal solution, Eq. (3.7). Top row: Normalized intensity $|A_{\alpha}^{l=+1}(x, y = 0, \xi; z)|^2$. Bottom row: Phase $\Phi(x, \xi) = \tan^{-1}[\mathrm{Im}\,(a)/\mathrm{Re}(a)]$, where $a = A_{\alpha}^{l=+1}(x, y = 0, \xi; z)$. The phase colourmap and red arrows show the direction of increasing phase Φ. (b) Experiment: An $l = 1$ STOV is generated by passing a near-Gaussian pulse through a $4f$ pulse shaper with an $l = +1$ spiral phase plate at the shaper's Fourier plane (experimental details in [27]), and the STOV amplitude and phase is captured in flight by TG-SSSI (details in [27,28]). The experimental Rayleigh length is $z_{0x} = 46$mm. The horizontal axis for both (a) and (b) is normalized to the experimental spacetime eccentricity $\alpha = w_{0\xi}/w_{0x} = 0.3$. The phase plots in (b) are blanked out in regions of low intensity where phase extraction fails [28]. Within each panel, the pulse propagates from right to left.

For a more direct analysis of angular momentum of STOVs, the HG-based mode solutions can be expressed in spacetime polar coordinates (ρ, Φ), where $x = \rho \sin \Phi$ and $\xi = \rho \cos \Phi$. Here, we can describe the spacetime phase winding by the topological charge l and the single function Φ, even for the general case of elliptical and astigmatic STOV pulses. The fundamental rectangular mode based on Eq. (3.3) is now written as,

$$
\begin{aligned}
&A_{000}(\rho, y, \Phi; z) \\
&\quad = A_0 \sqrt{\frac{w_{0x} w_{0y} w_{0\xi}}{w_x(z) w_y(z) w_\xi(z)}} \exp\left(-\frac{\rho^2 \sin^2 \Phi}{w_x^2(z)} - \frac{y^2}{w_y^2(z)} - \frac{\rho^2 \cos^2 \Phi}{w_\xi^2(z)}\right) \\
&\qquad \times \exp\left[ik_0 \left(\frac{\rho^2 \sin^2 \Phi}{2R_x(z)} + \frac{y^2}{2R_y(z)} - \frac{\rho^2 \cos^2 \Phi}{2\beta_2 R_\xi(z)}\right)\right] \\
&\qquad \times \exp\left[-\frac{i}{2}\Big(\psi_x(z) + \psi_y(z) - \psi_\xi(z)\Big)\right],
\end{aligned} \tag{3.8}
$$

and the $l = \pm 1$ STOV pulse from the pulse shaper is given as

$$
A_\alpha^{l=\pm 1}(\rho, y, \Phi; z) = A_{000}(\rho, y, \Phi; z)\left(\frac{\rho \cos \Phi}{w_\xi(z)} e^{i\psi_{xi}(z)} \pm \frac{i\rho \sin \Phi}{w_x(z)} e^{-i\psi_x(z)}\right). \tag{3.9}
$$

In the associated experiments, the y-dependent beam envelope shape, aside from transverse diffractive spreading, is preserved in propagation. So henceforth, variations in y are neglected by setting $y = 0$, noting that any 3D mode can be constructed by multiplying the (x, ξ)-dependent results by $u_p^y(y; z)$.

3.3 Orbital Angular Momentum of Spatiotemporal Optical Vortices

3.3.1 Spacetime OAM Operator

Application of the traditional orbital angular momentum operator, $\boldsymbol{L} = \nabla\phi$, to find the transverse OAM of a STOV implies super luminal energy flow. In order to evaluate the STOV angular momentum $\hat{\mathbf{y}}L_y$, which is orthogonal to the the x-ξ plane of spatiotemporal phase circulation, we must first find the appropriate angular momentum operator $\boldsymbol{L}$. This is accomplished by considering Eq. (3.2) along with the conservation of energy density flux, $\mathbf{j}$ [88], $\partial|A|^2/\partial z = -\nabla\cdot\mathbf{j}$, where $\mathbf{j} = \mathbf{j}_\perp + \mathbf{j}_\parallel$, $\mathbf{j}_\perp = -i(2k_0)^{-1}(A^*\nabla_\perp A - A\nabla_\perp A^*)$, and $\mathbf{j}_\parallel = i\beta_2(2k_0)^{-1}[A^*(\partial/\partial\xi)A - A(\partial/\partial\xi)A^*]\hat{\boldsymbol{\xi}}$, where $\hat{\boldsymbol{\xi}}$ is the unit vector along increasing ξ. This gives $\mathbf{j} = k_0^{-1}|A|^2\left[\nabla_\perp\Phi - \beta_2\,(\partial\Phi/\partial\xi)\hat{\boldsymbol{\xi}}\right] = k_0^{-1}|A|^2\nabla_{st}\Phi$, where $A = |A|e^{i\Phi}$ and we identify $\nabla_{st}\equiv\nabla_\perp - \hat{\boldsymbol{\xi}}\beta_2(\partial/\partial\xi)$ as the spacetime gradient. Therefore, the spacetime linear momentum operator is $\hat{\mathbf{p}} = -i\nabla_{st}$, giving $\hat{\boldsymbol{L}} = -i\mathbf{r}\times\nabla_{st}$ so,

$$L_x = i\left(\xi\frac{\partial}{\partial y} + y\beta_2\frac{\partial}{\partial\xi}\right), \tag{3.10a}$$

$$L_y = -i\left(\xi\frac{\partial}{\partial x} + x\beta_2\frac{\partial}{\partial\xi}\right), \tag{3.10b}$$

and, as usual,

$$L_z = -i\left(x\frac{\partial}{\partial y} - y\frac{\partial}{\partial x}\right). \tag{3.10c}$$

In spacetime polar coordinates, L_y becomes

$$L_y = -i\left[\rho \sin\Phi \cos\Phi\,(1+\beta_2)\frac{\partial}{\partial\rho} + (\cos^2\Phi - \beta_2 \sin^2\Phi)\frac{\partial}{\partial\Phi}\right]$$

$$= L_y^e + L_y^i, \tag{3.11}$$

where we identify the first term as the extrinsic STOV angular momentum L_y^e, and the second term as the intrinsic STOV angular momentum L_y^i. Here, *intrinsic* refers to the origin-independent spatiotemporal angular momentum contribution, and *extrinsic* refers to the origin-dependent contribution which integrates to zero, $\langle L_y^e \rangle = 0$, when calculating the expectation value ($\langle\ \ \rangle$) of L_y by integrating over $\rho\ (0 \to \infty)$ and $\Phi\ (0 \to 2\pi)$.

3.3.2 Expectation Values for STOV OAM

To calculate the STOV OAM associated with $A_\alpha^l(\rho, y, \Phi; z)$, we note that it is sufficient to do so at the beam waist, $z = 0$. This is because $\langle L_y \rangle$ is invariant with propagation, namely $(d/dz)\langle L_y \rangle = i(2k_0)^{-1}\langle [H, L_y] \rangle = 0$, owing to the fact that $[H, L_y] = 0$; L_y commutes with the propagation operator. It is also worth noting here that the traditional OAM operator, $L_y^{\text{trad}} = -i(\xi\,\partial/\partial x - x\,\partial/\partial\xi)$, does not commute with H, $[H, L_y^{\text{trad}}] = (1-\beta_2)\partial^2/\partial x \partial\xi$, and as such is not a conserved quantity. This procedure greatly simplifies the calculation, especially for nonzero β_2, where we consider the beam waist to be placed just inside the material interface ($z = 0^+$) without additional chirp from the material yet induced. At $z = 0$, Eq. (3.9) becomes

$$A_\alpha^{l=\pm1} = A_\alpha^{l=\pm1}(\rho, y=0, \Phi; z=0)$$

$$= A_{000}(\rho, 0, \Phi; 0)\left(\frac{\rho\cos\Phi}{w_{0\xi}} \pm \frac{i\rho\sin\Phi}{w_{0x}}\right)$$

$$= A_0\frac{\rho}{w_{0\xi}}\exp\left(-\frac{\rho^2}{w_{0\xi}^2}(\cos^2\Phi + \alpha^2\sin^2\Phi)\right)$$

$$\times\left(\frac{(1+\alpha)}{2}e^{i\Phi} + \frac{(1\mp\alpha)}{2}e^{-i\Phi}\right). \tag{3.12}$$

This is nearly a linear combination of $\mathrm{LG}^{0\pm1}$ modes except for the Φ-dependent exponential prefactor, which loses its angle dependence for $\alpha = 1$, yielding the symmetric spacetime Laguerre Gaussian mode $A_{\alpha=1}^{l=\pm1} = \mathrm{LG}_{\text{spacetime}}^{0\pm1} = A_0\left(\rho/w_{0\xi}\right)\exp\left(-\rho^2/w_{0\xi}^2\right)e^{\pm i\Phi}$.

For arbitrary topological charge l, the lth order STOV pulse is

$$A_\alpha^l = A_\alpha^l(\rho, y=0, \Phi; z=0)$$

$$= A_0\left(\frac{\rho}{w_{0\xi}}\right)^{|l|}\exp\left[-|l|\left(\frac{\rho^2}{w_{0\xi}^2}(\cos^2\Phi + \alpha^2\sin^2\Phi)\right)\right]$$

$$\times(\cos\Phi + i\alpha\,\mathrm{sgn}(l)\sin\Phi)^{|l|}. \tag{3.13}$$

For a STOV with a phase winding of charge l and eccentricity $\alpha = 1$, and for general α,

$$\langle L_y\rangle_{l,\alpha=1} = \langle A_{\alpha=1}^l|L_y^i + L_y^e|A_{\alpha=1}^l\rangle$$

$$= \langle A_{\alpha=1}^l|L_y^i|A_{\alpha=1}^l\rangle = \frac{1}{2}l(1-\beta_2), \tag{3.14a}$$

$$\langle L_y \rangle_{l,\alpha} = \langle A_\alpha^l | L_y^i + L_y^e | A_\alpha^l \rangle$$

$$= \langle A_\alpha^l | L_y^i | A_\alpha^l \rangle = \frac{1}{2} l \left(\alpha - \frac{\beta_2}{\alpha} \right), \quad (3.14b)$$

where $\langle L_y^e \rangle = 0$, and where $\langle L_y \rangle$ depends explicitly on topological charge l, STOV eccentricity α, and material dispersion β_2.

This is a remarkable result, for which we will first consider the case $\alpha = 1$, a space-time symmetric STOV. For the case of vacuum ($\beta_2 = 0$), $\langle L_y \rangle = l/2$; STOV OAM is quantized in half integer units. For dispersive media ($\beta_2 \neq 0$), a quantum interpretation of the role of β_2 is strongly suggested, where one might consider the material disturbance induced by a STOV-encoded photon field as a new type of quasiparticle, a "STOV polariton."

A physical explanation for half-integer STOV orbital angular momentum in vacuum is that electromagnetic energy density flow in the pulse frame is purely along $\pm x$, or along $\nabla_\perp$. In these local coordinates, for $l = +1$, energy density flows along $-x$ in advance of the STOV singularity and along $+x$ behind it, as seen in experiments and calculations in Fig. 3.1 and in Ref. [27]. Because $\beta_2 = 0$ or is negligible in vacuum or extremely dilute media, there is no energy flow along ξ. This is in contrast to a standard $\mathrm{LG}_{\mathrm{space}}^{0\pm1}$ mode, where electromagnetic energy density circulates clockwise or counterclockwise around the singularity.

3.3.3 Physical Interpretation of β_2 and α

We now examine the physical meanings of β_2 and α in Eqs. (3.14). For simplicity, we first consider $\alpha = 1$ and later return to the interpretation of α. Note that in Eq. (3.13) we used the vacuum STOV ($\beta_2 = 0$) – with its original spectral phase -- implicitly at $z = 0^+$ (just inside the material) to calculate $\langle L_y \rangle_l$. But in reality, even at $z = 0^+$, the STOV spectral phase would have been modified by the dispersive material. Therefore, for a given phase winding l, the added term $-(l/2)\beta_2$ in $\langle L_y \rangle_l$, which is imposed by the β_2-dependent L_y^i operator, [Eq. (3.11)], represents sharing of the pulse OAM with the material. This suggests that the material has an electromagnetic OAM response quantized in half integer steps of β_2 – we identify this object as a bulk medium STOV polariton. For the case of $\beta_2 = 1$, $\langle L_y \rangle_l = 0$ and the medium has apparently taken up $l/2$ units of angular momentum from the STOV field. It is interesting to note that $\beta_2 = 1$ for materials with a quadratic dispersion relation ($\omega \propto k^2$) or effective mass for photons. This is a known dispersion dependence for polaritons [89,90]. For a negatively dispersive material with $\beta_2 = -1$, we get $\langle L_y \rangle_l = l$, which can be interpreted as a splitting of STOV OAM between photon and polariton field, or as the self-consistent electromagnetic object in the dispersive material having integer spatiotemporal OAM. Other values of β_2 give a range of OAM contributions between photons and polaritons.

But what of the asymmetry parameter α? In the context of spatial OAM [1], there is nothing sacrosanct about circular symmetry except that the OAM for such beams coincides with the topological charge l of the vortex. It has been demonstrated that the

intrinsic spatial OAM per photon of monochromatic beams with $w_{x0} \neq w_{y0}$ is determined by the ratio w_{0y}/w_{0x} [91,92]. That is, the transverse beam shape is encoded onto the photon OAM. Although the spacetime paraxial equation (STPWE) [Eq. (3.2)] is different than the spatial PWE, and the spacetime OAM operator is different than the spatial OAM operator, our conclusions in regards to the STOV eccentricity parameter, $\alpha = w_{0\xi}/w_{0x}$, is the same: α is encoded onto the intrinsic STOV OAM. In vacuum, STOV OAM is quantized in integer steps of $\alpha/2$ (or half-integer steps of α), while in a dispersive medium, it is quantized in integer steps of $(\alpha - \beta_2/\alpha)/2$. For normally dispersive material with $\beta_2 > 0$, $\langle L_y \rangle_l = 0$ for $\alpha = \sqrt{\beta_2}$; the polariton most efficiently takes up STOV OAM when the eccentricity is tuned to the materials normalized GVD.

Considering the limit $\alpha \to 0$ in vacuum [and ignoring the breakdown in the slowly varying envelope approximation used to obtain Eq. (3.2)], $\langle L_y \rangle_l \to 0$ as is appropriate: the pulse loses the timelike contribution to its vorticity. In a dispersive medium, $\alpha \to 0$ corresponds to a shrinking temporal pulse width accompanied by increasing bandwidth, for which dispersion and the phase gradient contribution of $\hat{\boldsymbol{\xi}}\beta_2 \partial\Phi/\partial\xi$ to $\langle L_y \rangle_l$ increase significantly. In classical terms, electromagnetic energy flow in $\hat{\boldsymbol{\xi}}$ dominates that in $\hat{\mathbf{x}}$. To be consistent with the *given* topological charge l, $\left|\langle L_y \rangle_l\right|$ must become large. For $\alpha \to \infty$, the pulse becomes very long and effect of dispersion goes away ($\beta_2/\alpha \to 0$). Then, to be consistent for a given l, the phase gradient $\hat{\mathbf{x}}\partial\Phi/\partial x$

must become very large, as does $\langle L_y \rangle_l$. In general, heuristic electromagnetic energy flow arguments like these provide good physical insight into the effects of varying α and β_2.

Figure 3.2(a) shows plots of STOV intensity, $\left|A_{\alpha=1}^{l=1}(x, y=0, \xi; z)\right|^2$, and energy density flux **j,** computed using Eq. (3.7), for $l = 1$, $\alpha = 1$, and $\beta_2 = 1, 0.5, 0, -0.5, -1$, and Fig. 3.2(b) shows similar results for spacetime-eccentric $l = 1$ STOV with $\alpha = 0.5$. For each row of Fig. 3.2, $\langle L_y \rangle = \frac{1}{2}(\alpha - \beta_2/\alpha)$ is a constant. The purely diffractive contributions to **j** have been subtracted out, leaving the flow contributing to OAM (See Sec. 3.5). The red arrows show the direction of the spatiotemporal phase gradient $\nabla\Phi(x, \xi)$, and the red diagonals mark the boundary across which there is a phase jump of π. In the panels with red diagonal lines, even though the phase winding has disappeared, $\langle L_y \rangle$ remains constant for that particular row. It is seen that for a STOV propagating in a medium with $\beta_2 > 0$, the energy density flow exhibits a "saddle" pattern with respect to the singularity, while for $\beta_2 < 0$, the flow is spiral, and for $\beta_2 = 0$, the flow is restricted to $\pm x$. Note that for $\beta_2 = 1$, where $\langle L_y \rangle = \frac{1}{2}(1 - \beta_2) \propto \int dx d\xi \, (\mathbf{r} \times \mathbf{j})_y = 0$ and OAM is shared equally by the electromagnetic and polariton response, **j** vanishes everywhere at $z = z_{0x}$.

A range of interesting behavior is observed in Fig. 3.2, with the main points summarized as follows: (1) In normally dispersive materials ($\beta_2 > 0$), the directions of the OAM and the phase gradient are not always consistent; the phase winding

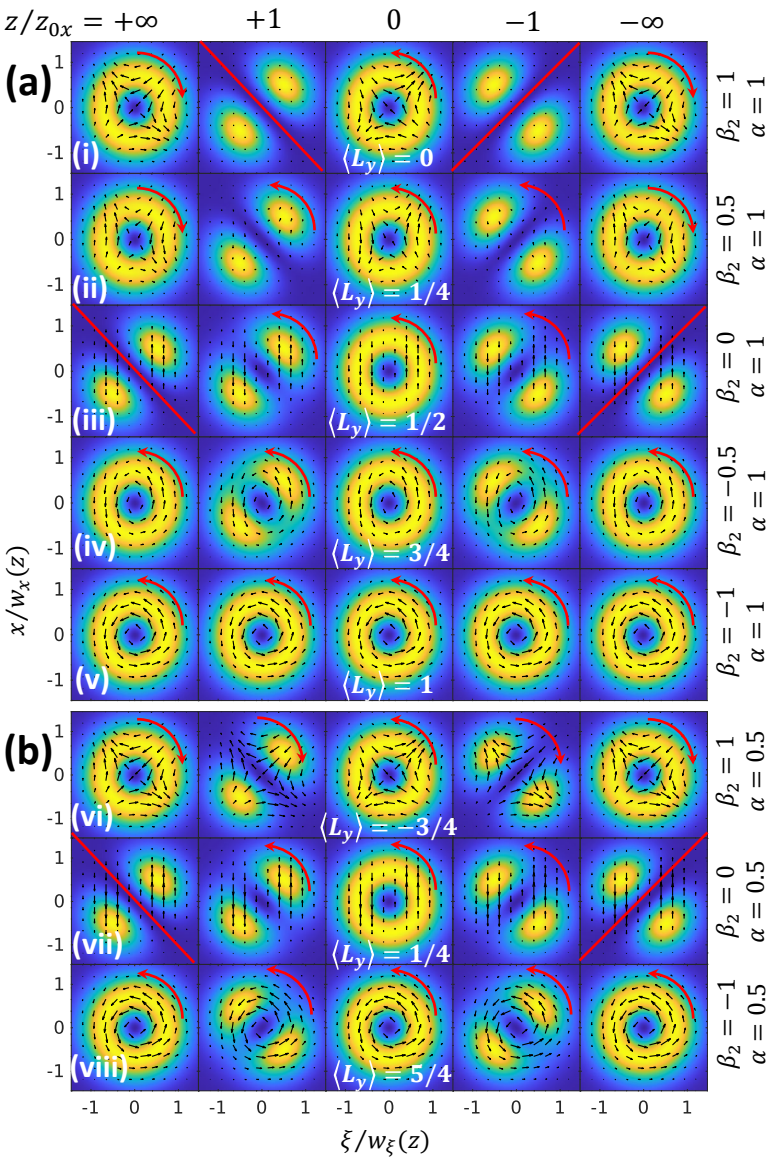

Figure 3.2. (a) Plots of STOV intensity $\left|A^{l=1}_{\alpha=1}(x, y = 0, \xi; z)\right|^2$ and energy density flux j (depicted by overlaid arrows), computed using Eq. (3.7) for $l = 1$, $\alpha = 1$ and $\beta_2 = 1,\ 0.5,\ 0, -0.5, -1$. The purely diffractive contributions to j have been subtracted out, leaving the flow contributing to OAM (See Sec. 3.5). Propagation is shown through the beam waist ($z/z_{0x} = 0$) and into the far field ($\pm\infty$). The red arrows indicate the direction of spatiotemporal phase gradient $\nabla\Phi(x, \xi)$ and the red diagonals mark the boundary across which there is a phase jump of π. (b) Similar plots for spacetime-eccentric $l = 1$ STOVs with $\alpha = 0.5$ and $\beta_2 = 1, 0, -1$. For each row in (a) and (b), the value of $\langle L_y \rangle$ is shown in the $z = 0$ (centre) panels. Within each panel of (a) and (b), the pulse propagates right to left.

direction can flip to maintain OAM conservation [see rows (i), (ii), and (vi)]. (2) The phase winding can disappear, yet nonzero $\langle L_y \rangle$ remains [rows (iii) and (vi)]. (3) A donut-shaped STOV launched in vacuum or dilute media does not stay together as a donut; the spatiotemporal energy flow component $\mathbf{j}_\perp$ forces the donut into spatiotemporally offset lobes [rows (iii) and (vii)]. (4) For $\beta_2 \neq 0$, the near and far field intensity profiles are self-similar [all rows except (iii) and (vii)]. (5) There exists a self-similar STOV mode with integer OAM for $\alpha = 1$ and $\beta_2 = -1$ [row (v)]. Classically, this is visualized as balanced STOV energy flow along $\hat{\mathbf{x}}$ and $\hat{\boldsymbol{\xi}}$.

3.4 Conclusions

This chapter presented an analysis for a new class of light states, spatiotemporal optical vortices (STOVs), with orbital angular momentum (OAM) orthogonal to propagation. In vacuum, the OAM of these states is quantized in integer multiples of $\alpha/2$, where α is the STOV eccentricity parameter. For a symmetric STOV ($\alpha = 1$) in vacuum, the OAM is quantized in integer multiples of ½. In a dispersive medium, it is quantized in integer multiples of $(\alpha - \beta_2/\alpha)$, where β_2 is the normal group velocity dispersion of the material, where we consider the OAM as shared between a photon and a STOV polariton. These results are expected to motivate further studies into the physics and applications of STOVs.

3.5 Additional Material:

A.1 Mode Solutions of the Paraxial Wave Equation in the Spatiotemporal Domain

As in Sec. 3.2, the wave equation in the spectral domain,

$$\left(\nabla_\perp^2 + \frac{\partial^2}{\partial z^2} + k^2(\omega)\right)\tilde{\boldsymbol{\mathcal{A}}}(\boldsymbol{r}_\perp, z, \omega) = 0 \ , \tag{A1}$$

eventually leads to the paraxial wave equation for the slowly varying amplitude $A = A(\mathbf{r}_\perp, \xi; z)$,

$$i2k_0 \frac{\partial A}{\partial z} = \left(-\nabla_\perp^2 + \beta_2 \frac{\partial^2}{\partial \xi^2}\right) A = HA \ , \tag{A2}$$

where z plays the role of a time-like running parameter that indexes the evolution of the pulse as it propagates, $\xi = v_g t - z$ is a local space coordinate in the frame of the pulse, and $\beta_2 = v_g^2 k_0 k_0''$ is the normalized group velocity dispersion, and H is the propagator. For $\nabla_\perp^2 = \partial^2/\partial x^2 + \partial^2/\partial y^2$, Eq. (A2) has separable solutions $A = A^x(x,z)A^y(y,z)A^\xi(\xi,z)$.

For $\mathbf{r}_\perp = (x, y)$, the most general Hermite-Gaussian (HG) mode solution is

$$\begin{aligned} A_{mp}^{xy}(x, y; z) = A_m^{0,x} A_p^{0,y} \sqrt{\frac{w_{0x} w_{0y}}{w_x(z) w_y(z)}} H_m\left(\frac{\sqrt{2}x}{w_x(z)}\right) H_p\left(\frac{\sqrt{2}y}{w_y(z)}\right) \\ \times \exp\left[\frac{-x^2}{w_x^2(z)} + \frac{-y^2}{w_y^2(z)}\right] \exp\left[ik_0\left(\frac{x^2}{2R_x(z)} + \frac{y^2}{2R_y(z)}\right)\right] \\ \times \exp\left[-i\left(m + \tfrac{1}{2}\right)\psi_x(z) - i\left(p + \tfrac{1}{2}\right)\psi_y(z)\right], \end{aligned} \tag{A3}$$

which allows for different spot sizes (w_{0x}, w_{0y}, $w_x(z) = w_{0x}(1 + (z/z_{0x})^2)$, and $w_y(z) = w_{0y}(1 + (z/z_{0y})^2)$), radii of curvature ($R_x$, R_y), and Gouy phase shifts ($\psi_x(z) = \tan^{-1}(z/z_{0x})$ and $\psi_y(z) = \tan^{-1}(z/z_{0y})$), where $z_{0x} = \frac{1}{2}k_0 w_{0x}^2$ and $z_{0y} = \frac{1}{2}k_0 w_{0y}^2$ are the Rayleigh lengths.

For the local, time-like spatial coordinate ξ, the HG solution is

$$A_q(\xi; z) = A_q^{0,\xi}\sqrt{\frac{w_{0\xi}}{w_\xi(z)}}\exp\left(-\frac{\xi^2}{w_\xi^2(z)}\right)\exp\left(-i\frac{k_0}{\beta_2}\frac{\xi^2}{2R_\xi(z)}\right) \times \exp\left(i\left(q+\tfrac{1}{2}\right)\psi_\xi(z)\right), \tag{A4}$$

where, $z_{0\xi} = k_0 w_{0\xi}^2/2|\beta_2|$, $w_\xi(z) = w_{0\xi}(1 + (z/z_{0\xi})^2)$, $R_\xi(z) = z(1 + (z_{0\xi}/z)^2)$, and the Gouy phase is $\psi_\xi(z) = \mathrm{sgn}(\beta_2)\tan^{-1}(z/z_{0\xi})$.

The complete solution to the polychromatic paraxial equation is then

$$\begin{aligned} &A_{mpq}(x, y, \xi; z) \\ &= A_m^{0,x}A_p^{0,y}A_q^{0,\xi}\sqrt{\frac{w_{0,x}w_{0,y}w_{0,\xi}}{w_x(z)w_y(z)w_\xi(z)}}H_m\left(\frac{\sqrt{2}x}{w_x(z)}\right)H_p\left(\frac{\sqrt{2}y}{w_y(z)}\right)H_q\left(\frac{\sqrt{2}\xi}{w_\xi(z)}\right) \\ &\quad\times\exp\left(-\frac{x^2}{w_x^2(z)}-\frac{y^2}{w_y^2(z)}-\frac{\xi^2}{w_\xi^2(z)}\right) \\ &\quad\times\exp\left(ik_0\left(\frac{x^2}{2R_x(z)}+\frac{y^2}{2R_y(z)}-\frac{\xi^2}{2\beta_2 R_\xi(z)}\right)\right) \\ &\times\exp\left(-i(m+\tfrac{1}{2})\psi_x\right)\exp\left(-i(p+\tfrac{1}{2})\psi_y\right)\exp\left(i(q+\tfrac{1}{2})\psi_\xi\right), \end{aligned} \tag{A5}$$

The x, y, and ξ solutions are normalized to form a basis in the spatiotemporal domain,

$$u_m^x(x;z) = \frac{C_m}{\sqrt{w_x(z)}} H_m\left(\frac{\sqrt{2}\,x}{w_x(z)}\right)\exp\left(-\frac{x^2}{w_x^2(z)}\right)$$
$$\times \exp\left(ik_0\frac{x^2}{2R_x(z)}\right)\exp\left(-i\left(m+\tfrac{1}{2}\right)\psi_x(z)\right), \quad \text{(A6a)}$$

$$u_p^y(y;z) = \frac{C_n}{\sqrt{w_y(z)}} H_p\left(\frac{\sqrt{2}\,y}{w_y(z)}\right)\exp\left(-\frac{y^2}{w_y^2(z)}\right)$$
$$\times \exp\left(ik_0\frac{y^2}{2R_y(z)}\right)\exp\left(-i\left(p+\tfrac{1}{2}\right)\psi_y(z)\right), \quad \text{(A6b)}$$

$$u_q^\xi(\xi;z) = \frac{C_q}{\sqrt{w_\xi(z)}} H_q\left(\frac{\sqrt{2}\,\xi}{w_\xi(z)}\right)\exp\left(-\frac{\xi^2}{w_\xi^2(z)}\right)$$
$$\times \exp\left(-ik_0\frac{\xi^2}{2\beta_2 R_\xi(z)}\right)\exp\left(i\left(q+\tfrac{1}{2}\right)\psi_\xi(z)\right), \quad \text{(A6c)}$$

where $C_j = \left(\frac{2}{\pi}\right)^{\frac{1}{4}}\left(2^j\, j!\right)^{-\frac{1}{2}}$.

A $l=\pm1$ STOV with spatiotemporal eccentricity $\alpha = w_{0\xi}/w_{0x}$, constructed as $A_\alpha^{l=\pm1}(x,y,\xi,z=0) = A_0\left(\frac{\xi}{w_{0,\xi}} \pm i\frac{x}{w_{0,x}}\right)\exp\left(-\frac{x^2}{w_{0x}^2}-\frac{y^2}{w_{0y}^2}-\frac{\xi^2}{w_{0\xi}}\right)$, can be expressed in the basis of Eqs. A6(a-c) as

$$A_\alpha^{l=\pm1}(x,y,\xi;z=0) = \frac{A_0\sqrt{w_{0x}w_{0y}w_{0\xi}}}{2\sqrt{2}C_0^2C_1}u_0^y(y,0)$$
$$\times\left(u_0^x(x,0)u_1^\xi(\xi,0) \pm iu_1^x(x,0)u_0^\xi(\xi,0)\right), \quad \text{(A7)}$$

and is thus propagated to $z>0$ by H to give

$$A_{\alpha}^{l=\pm 1}(x,y,\xi,z) = A_0 \sqrt{\frac{w_{0,x}w_{0,y}w_{0,\xi}}{w_x(z)w_y(z)w_\xi(z)}} \exp\left(-\frac{x^2}{w_x^2(z)} - \frac{y^2}{w_y^2(z)} - \frac{\xi^2}{w_\xi^2(z)}\right)$$
$$\times \exp\left(ik_0 \frac{x^2}{2R_x(z)} + ik_0 \frac{y^2}{2R_y(z)} - i\frac{k_0}{\beta_2}\frac{\xi^2}{2R_\xi(z)}\right)$$
$$\times \exp\left(-i\frac{1}{2}\psi_x(z) - i\frac{1}{2}\psi_y(z) + i\frac{1}{2}\psi_\xi(z\right)$$
$$\times \left[\frac{\xi}{w_\xi(z)} \exp\left(i\psi_\xi(z)\right) \pm i\frac{x}{w_x(z)} \exp\left(-i\psi_x(z)\right)\right]. \quad \text{(A8)}$$

A.2 Orbital Angular Momentum of STOVs

The similarity between the paraxial electromagnetic wave equation and the non-relativistic equation for evolution of a quantum wavefunction (the Schrödinger equation) simplifies calculation of dynamical quantities. For a quantum mechanical wavefunction $\psi(\mathbf{r}, t)$, one can use the Schrödinger equation to show that the probability density $|\psi(\boldsymbol{r}, t)|^2$ satisfies the continuity equation $\partial|\psi|^2/\partial t = -\nabla \cdot \mathbf{j}$, where $\mathbf{j}(\mathbf{r}, t) = i\hbar/2m\,(\psi\nabla\psi^* - \psi^*\nabla\psi)$ is the probability current density.

In our case, for the electromagnetic energy density $|A|^2$, an exactly analogous procedure [88] using Eq. (A2) gives

$$\frac{\partial|A|^2}{\partial z} = -\nabla \cdot \mathbf{j}, \quad \text{(A9)}$$

where $\nabla \cdot \mathbf{F} = \partial F_x/\partial x + \partial F_y/\partial y + \partial F_\xi/\partial \xi$, and z is a running parameter analogous to time t in the Schrodinger equation, and

$$\mathbf{j} = \frac{1}{i2k_0}(A^*\,\nabla_\perp A - A\nabla_\perp A^*) - \frac{\beta_2}{i2k_0}\left(A^*\frac{\partial A}{\partial \xi} - A\frac{\partial A^*}{\partial \xi}\right)\hat{\boldsymbol{\xi}} \quad \text{(B10)}$$

is the energy density flux. Using $A = |A|\exp(i\Phi)$, $\mathbf{j}$ simplifies to

$$\mathbf{j} = \frac{|A|^2}{k_0}\left(\frac{\partial\Phi}{\partial x}\hat{\mathbf{x}} + \frac{\partial\Phi}{\partial y}\hat{\mathbf{y}} - \beta_2\frac{\partial\Phi}{\partial\xi}\hat{\boldsymbol{\xi}}\right) = \frac{|A|^2}{k_0}\nabla_{\mathrm{st}}\Phi, \tag{A11}$$

Since $\mathbf{j} \propto \mathbf{p}$, where $\mathbf{p}$ is the linear momentum, we identify $\nabla_{\mathrm{st}} = \nabla_\perp - \beta_2\hat{\boldsymbol{\xi}}\,\partial/\partial\xi$ as the spacetime gradient appropriate for the linear momentum density operator $\hat{\mathbf{p}} = -i\nabla_{\mathrm{st}}$. This leads to the orbital angular momentum operator $\hat{\mathbf{L}} = \mathbf{r} \times \hat{\mathbf{p}}$, giving

$$L_y = (-i\mathbf{r} \times \nabla_{st})_y = -i(\xi\,\partial/\partial x + x\beta_2\,\partial/\partial\xi). \tag{A12a}$$

In analogy with the Schrödinger equation, it is straightforward to show that $(d/dz)\langle L_y\rangle = i(2k_0)^{-1}\langle[H, L_y]\rangle$, where $\langle\ \ \rangle$ denotes expectation value and $\langle L_y\rangle = \langle A|L_y|A\rangle$ is the expectation value of OAM. Because $[H, L_y] = 0$ (L_y commutes with the propagation operator H), $\langle L_y\rangle$ is invariant with propagation.

Transforming into polar coordinates using $x = \rho\sin\Phi$, and $\xi = \rho\cos\Phi$ gives

$$\begin{aligned} L_y = -i\left(\rho\sin\Phi\cos\Phi\,(1+\beta_2)\frac{\partial}{\partial\rho} + (\cos^2\Phi - \beta_2\sin^2\Phi)\frac{\partial}{\partial\Phi}\right) \\ = L_y^e + L_y^i \end{aligned} \tag{A12b}$$

where

$$L_y^e = -i\rho\sin\Phi\cos\Phi\,(1+\beta_2)\frac{\partial}{\partial\rho} \tag{A13}$$

and

$$L_y^i = -i(\cos^2\Phi - \beta_2\sin^2\Phi)\frac{\partial}{\partial\Phi} \tag{A14}$$

are the extrinsic and intrinsic components of the OAM operator, where $\langle L_y\rangle = \langle A|L_y|A\rangle = \langle A|L_y^e + L_y^i|A\rangle = \langle A|L_y^i|A\rangle$ because $\langle A|L_y^e|A\rangle = 0$.

The expectation value of L_y is calculated for general l and α as

$$\langle L_y \rangle = \frac{\int_0^{2\pi}\int_0^{\infty} A_\alpha^{l^*}\, L_y\, A_\alpha^l \rho d\rho d\Phi}{\int_0^{2\pi}\int_0^{\infty} \left|A_\alpha^l\right|^2 \rho d\rho d\Phi} = \frac{1}{2} l \left(\alpha - \frac{\beta_2}{\alpha}\right), \tag{A15}$$

where

$$A_\alpha^l = \left(\frac{\rho}{w_{0\xi}}\right)^{|l|} \exp\left[-|l|\frac{\rho^2}{w_{0\xi}^2}(\cos^2\Phi + \alpha^2 \sin^2\Phi)\right] \times (\cos\Phi + i\alpha \mathrm{sgn}(l)\sin\Phi)^{|l|}, \tag{A16}$$

with $\alpha = w_{0\xi}/w_{0x}$ and $l = 0, \pm 1, \pm 2, \ldots$.

To verify that $\langle L_y \rangle$ is conserved, we use Eq. (A8) and (A12a), to compute $\langle A_{\alpha=1}^{l=1} | L_y | A_{\alpha=1}^{l=1} \rangle$ as a function of z for $z = 0$ to $z = 100 z_{0x}$ (for the cases $\beta_2 = +1$, $\beta_2 = 0$, and $\beta_2 = -1$). This is plotted in Fig. A1. It is seen that $\langle L_y \rangle$ is invariant with

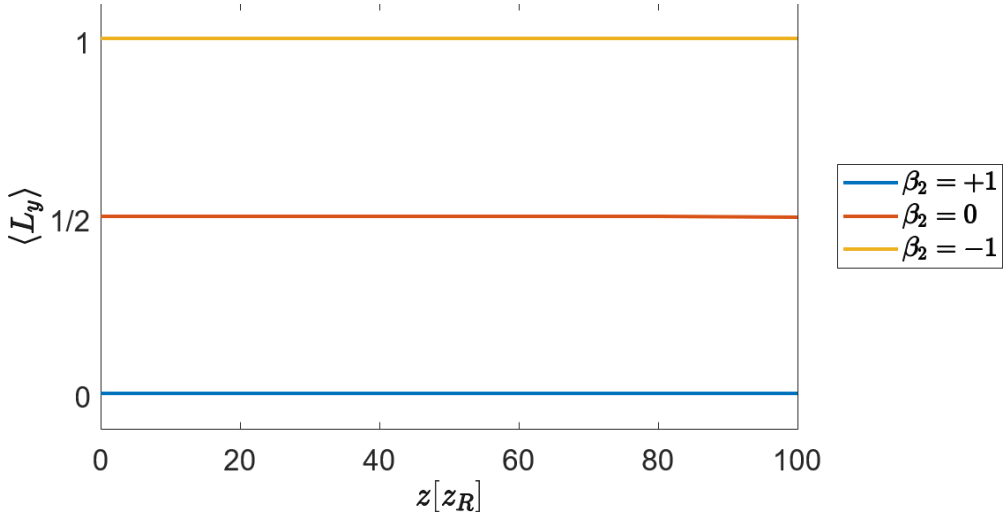

Figure A1. The OAM expectation value $\langle L_y \rangle$, computed for an $l = 1$ STOV using Eqs. (A8) and (A12a) plotted as a function of propagation distance in Rayleigh lengths ($z_{0x} = k_0 w_{0x}^2/2$) for $\beta_2 = +1$, $\beta_2 = 0$, and $\beta_2 = -1$. In all cases, $\langle L_y \rangle$ is conserved.

z and in agreement with the values given by Eq. (A15).

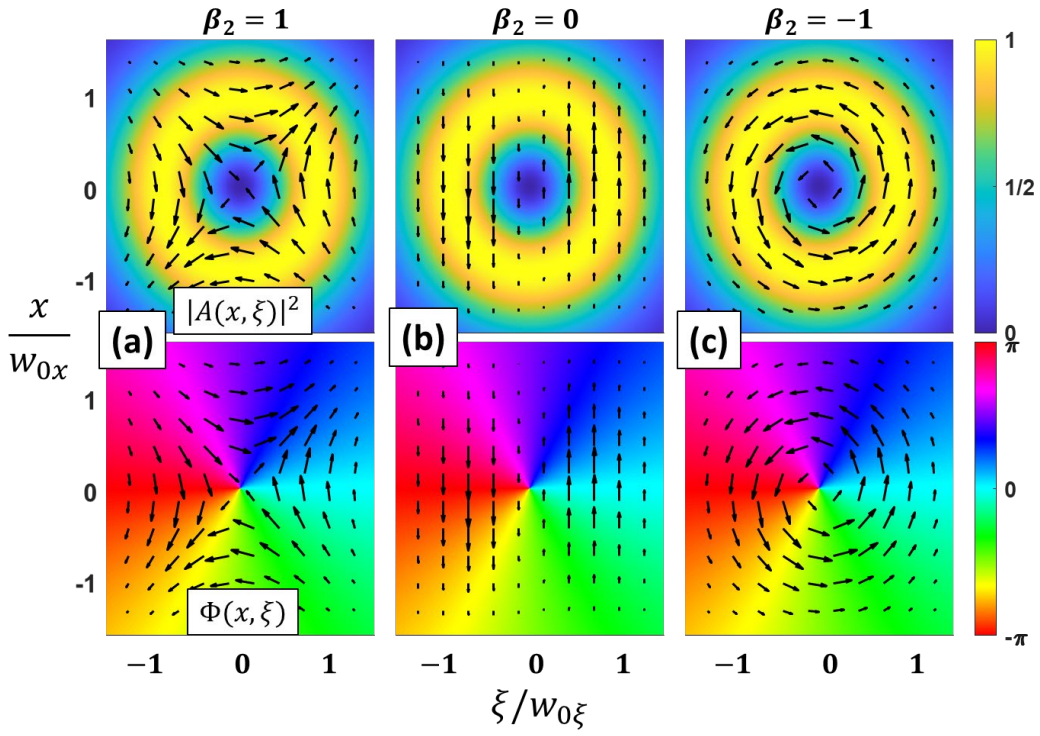

Figure A2. STOV spatiotemporal intensity $|A(x,\xi)|^2$ (top row) and phase $\Phi(x,\xi)$ (bottom row) at z=0 for three values of normalized GVD: (a) $\beta_2 = 1$, (b) $\beta_2 = 0$, and (c) $\beta_2 = -1$. Superimposed on the plots are arrows depicting local energy density flow **j**, where the arrow lengths are proportional to **|j|**. It is seen that the spatiotemporal flow is saddle-shaped in (a), only spatially directed ($\pm x$) in (b), and spiral in (c).

Figure A2 (top panels) plots spatiotemporal intensity profiles at $z = 0$ for a $l = 1$ STOV for (a) $\beta_2 = 1$, (b) $\beta_2 = 0$, and (c) $\beta_2 = -1$. The bottom panels plot the respective spatiotemporal phase profiles. The local energy density flux **j** is overlaid as arrows on both top and bottom panels, with the arrow lengths proportional to **|j|**. For $\beta_2 = 1$, the spatiotemporal energy flow is seen to be saddle-shaped about the STOV singularity. For $\beta_2 = 0$, energy density flow is restricted to the spatial domain, with flow along $-x$ before the singularity and along $+x$ after it. For $\beta_2 = -1$, the energy

density flow is spiral about the singularity. All elements of this figure are computed using (A8) and (A10) (or, equivalently, (A11) and (A16)).

In Fig. A3, intensity and energy density flux is plotted for $l = 1, \alpha = 1$ STOVs propagated from $z = 0$ to $z = +\infty$. Here, unlike Fig. 3.2 in the main chapter, we plot arrows for *total* **j**, which includes the contribution to OAM and the contribution from spatial and temporal dispersion. It is seen that for $z/z_{0x} > \sim 1$, the contributions to **j** from spatial and temporal dispersion begin to dominate the local energy density flow.

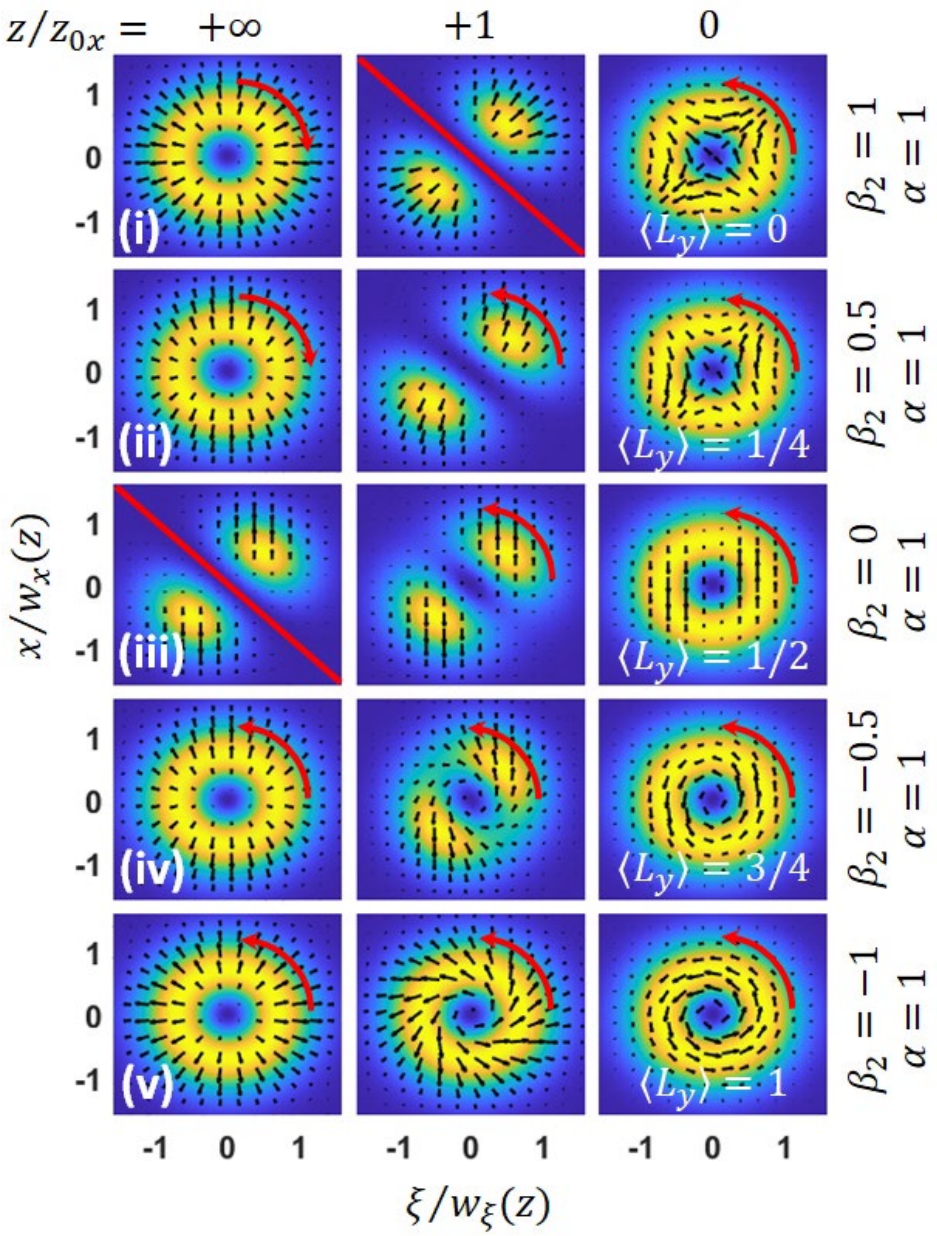

Figure A3. Energy density flux **j** (arrows) superimposed on STOV intensity profiles for $\alpha = 1$ and $\beta_2 = +1, \beta_2 = 0$, and $\beta_2 = -1$ at locations $z/z_{0x} = 0, 1,$ and ∞. The arrow lengths are proportional to $|\mathbf{j}|$. The curved red arrows are in the direction of $\nabla\Phi(x, \xi)$ and the red diagonals mark the boundary of a π phase jump. The phase winding has disappeared at those locations. Unlike Fig. 3.2 of the main text, the dispersion/diffraction contributions to **j** are maintained in this figure. Consequently, after a few Rayleigh ranges of propagation, the energy density flow is dominated by spatial and temporal dispersion.

Chapter 4: Free-space propagation of spatiotemporal optical vortices

4.1 Introduction

Now that we have developed a measurement technique, modal analysis and a sound theory for the transverse OAM carried by STOVs we move on to their direct measurement. In this chapter, we demonstrate the linear generation of STOVs by shaping the spatiospectral domain of a pulse and measure their free-space propagation using TG-SSSI [28]. The experimental and simulated results are in agreement with the theoretical models found in Chapter 3 and Ref. [30].

The discovery and analysis of the spatiotemporal optical vortex (STOV) was reported [24], whose phase windings resides in the spatiotemporal domain. Toroidal STOVs were found to be a universal electromagnetic structure that naturally emerges from the arrested self-focusing collapse of short pulses, which occurs, for example, in filamentation in air [93] as well as in the relativistic self-guiding in laser wakefield accelerators [94,95]. As this vortex is supported on the envelope of a short pulse, its description is necessarily polychromatic. For femtosecond filamentation in air, a pulse with no initial vorticity collapses and generates plasma at the beam center. The ultrafast onset of plasma provides sufficient transient phase shear to spawn two toroidal spatiotemporal vortex rings of charge $l = -1$ and $l = +1$ that wrap transversely around the pulse. In air, the delayed rotational response of N_2 and O_2 [55,56,96]

provides additional transient phase shear, generating additional $l = \pm 1$ ring (toroidal) STOVs on the trailing edge of the pulse [24]. After some propagation distance and STOV-STOV dynamics, the self-guided pulse is accompanied mainly by the $l = +1$ toroidal vortex, which governs the intrapulse energy flow supporting self-guiding [24].

The requirement of transient phase shear for such nonlinearly generated STOVs suggests that phase shear linearly applied in the spatiospectral domain could also lead to STOV formation, and use of a zero dispersion ($4f$) pulse shaper and phase masks have been proposed [26] and demonstrated for this purpose [57]. Here such a $4f$ pulse shaper is utilized to impose STOVs on Gaussian pulses and record single-shot in-flight phase and amplitude images of these structures using the diagnostic developed for this purpose and discussed in Chapter 2, transient-grating single-shot supercontinuum spectral interferometry (TG-SSSI) [28]. The structures generated "line-STOVs" as described in [24,26]; the phase circulates around a straight axis normal to the spatiotemporal plane. An electric field component of a simple $|l|^{\text{th}}$order line-STOV-carrying pulse at position $z \ll z_R$ (where z_R is the Rayleigh length) along the propagation axis can be described as

$$E(\boldsymbol{r}_\perp, z, \tau) = a\left(\frac{\tau}{\tau_s} + i\,\mathrm{sgn}(l)\frac{x}{x_s}\right)^{|l|} E_0(\boldsymbol{r}_\perp, z, t), \tag{4.1}$$

$$= A(x,\tau)\exp[il\Phi_{st}(x,\tau)]\,E_0(\boldsymbol{r}_\perp, z, \tau)$$

where $\boldsymbol{r}_\perp = (x, y)$, $\tau = t - z/v_g$ is a time coordinate local to the pulse, v_g is the group velocity, τ_s and x_s are temporal and spatial scale widths of the STOV, $\Phi_{st}(x,\tau)$ is the

space-time phase circulation in $x-\tau$ space, $l=\pm1,\pm2,...,$ $A(x,\tau)=a\left(\left(\frac{\tau}{\tau_s}\right)^2+\left(\frac{x}{x_s}\right)^2\right)^{\frac{|l|}{2}}$, $a=\sqrt{2}\left(\left(\frac{\tau_0}{\tau_s}\right)^2+\left(\frac{x_0}{x_s}\right)^2\right)^{-\frac{1}{2}}$ for $l=\pm1$, and E_0 is the STOV-free near-Gaussian pulse input to the pulse shaper where x_0 and τ_0 are its spatial and temporal scale widths. Here a is a normalization factor ensuring that pulse energy is conserved through the pulse shaper: $\int d^2\boldsymbol{r}_\perp d\tau|E|^2=\int d^2\boldsymbol{r}_\perp d\tau|E_0|^2$.

4.2 Experimental Setup

In order to confirm the presence of an ultrafast STOV-carrying pulse, both the phase and the amplitude of the electric field envelope must be measured, preferably in a single shot. In work by another group, amplitude and phase have been retrieved from

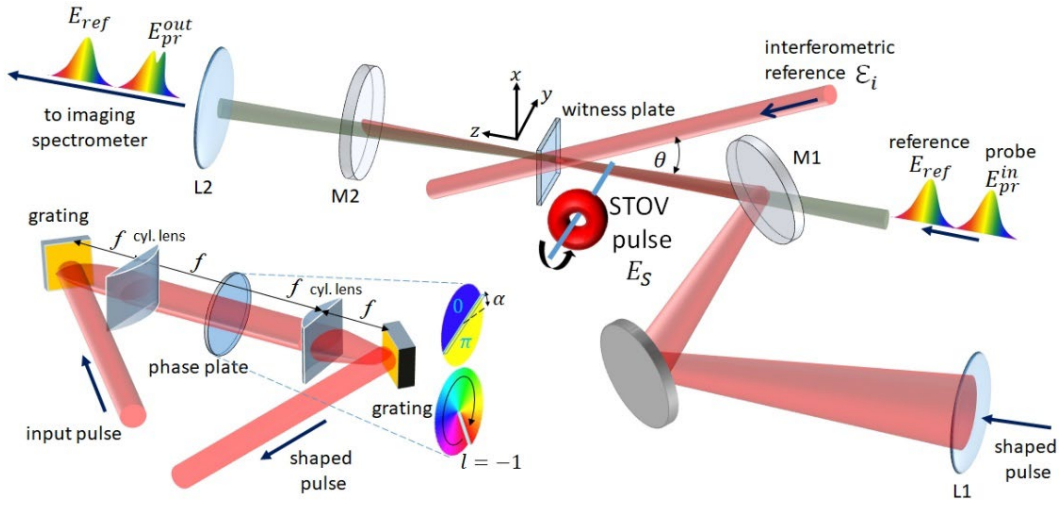

Figure 4.1. Top: Setup for transient grating single-shot spectral interferometry (TG-SSSI). The STOV-carrying pump pulse (center wavelength λ_0 =800nm) at the output of a $4f$ pulse shaper is focused (~1.5 μJ) or imaged (~20 μJ) into a 500 μm thick fused silica witness plate. The pump pulse energy is kept sufficiently low so that the STOV pulse propagates nearly linearly in the plate. A probe pulse $\mathcal{E}_i$ (λ_0 = 795nm, 2 nm bandwidth) crosses the STOV pulse direction at angle $\theta = 6°$, forming a transient grating with modulations $\propto cos\,(kx\,sin\,\theta + \Delta\Phi(x,\tau))$, where the symbols are defined in the main text and reference coordinates are shown next to the witness plate. The transient grating is probed by SSSI [49,58], which uses ~1.5 ps long chirped supercontinuum reference and probe pulses E_{ref} and E_{pr} (λ_0~575 nm). The result is single-shot time and space resolved images of amplitude and phase of STOV-carrying pulses. Bottom left: Cylindrical lens-based $4f$ pulse shaper [26,57] for imposing a line-STOV on a 45 fs, λ=800nm input pulse. A phase mask is inserted in the Fourier plane at the common focus of the cylindrical lenses. For the current experiment, we use spiral phase masks ($l = 1$, $l = -1$, and $l = 8$) and a π −step mask, all etched on fused silica, where the π −step angle α and the spiral orientation (for $l = -1$) are also shown. Both the $l = 1$ and $l = 8$ plates have 16 levels (steps) every 2π. Shaper gratings: 1200 line/mm, cylindrical lenses: focal length 20cm.

femtosecond pulses undergoing filamentation using a multi-shot scanning technique in combination with an iterative algorithm [97]. Single-shot supercontinuum spectral interferometry (SSSI) , has been used to measure the space- and time-resolved envelope (but not the phase) of ultrafast laser pulses from the near-UV [49,98] to the longwave infrared [55,56].

For measurements of STOVs, in which space-time phase circulation is a key feature, ordinary SSSI is insufficient. To measure space-time-resolved amplitude *and* phase in a single shot, we again use transient-grating SSSI (TG-SSSI) as described in Chapter 2 and Ref. [28]. The interferometric probe pulse $\mathcal{E}_i$ (same central wavelength of the pump pulse and spectrally filtered by a 2 nm FWHM bandpass filter; see Fig. 4.1) is interfered with the pump to form a transient spatiotemporal grating in the witness plate. Here $\mathcal{E}_i$ is crossed with E_s at an angle of $\theta = 6°$ (free-space crossing angle). The transient grating is now the structure probed by SSSI, with the output probe pulse becoming $E_{pr}^{out} \propto \chi^{(3)}(E_s + \mathcal{E}_i)(E_s^* + \mathcal{E}_i^*)E_{pr}^{in}$. As before, $\Delta\phi(x,\omega)$ is extracted from the interference of E_{pr}^{out} and E_{ref} in the imaging spectrometer, leading to $\Delta\phi(x,\tau)$. Now however, $\Delta\phi(x,\tau)$ is encoded with the pump envelope modulated by the time-dependent spatial interference pattern (transient grating): $\Delta\phi(x,\tau) \propto |E_s(x,\tau)|^2 + 2|E_s||\mathcal{E}_i|f(x,\tau)$, where $k_w = n_w k$ is the pump wavenumber in the witness plate, $f(x,\tau) = \cos\big(2k_w\, sin(\theta_w/2) + \Delta\Phi(x,\tau)\big)$ is the transient grating, θ_w is the crossing angle of E_s and $\mathcal{E}_i$ inside the witness plate and $\Delta\Phi(x,\tau)$ is the spatiotemporal phase of E_s. In the analysis of the two-dimensional (2D) $\Delta\phi(x,\tau)$ images, $\Delta\Phi(x,\tau)$ is extracted

using standard interferogram analysis techniques [49,98], and $I_s(x,\tau) \propto |E_s(x,\tau)|^2$ is extracted using a low-pass image filter (suppressing the sideband in Fourier space imposed by the transient grating).

STOVs were generated by a cylindrical lens-based $4f$ pulse shaper [26], depicted in the lower left of Fig. 4.1. The pulse shaper imposes a line-STOV on an input Gaussian pulse (50 fs, $1.5-20$ μJ) using a $2\pi l$ spiral transmissive phase plate (with $l = +1, -1,$ or $+8$) or a π-step plate at the shaper's Fourier plane (common focus of the cylindrical lenses). The vertical and horizontal axes on the phase masks lie in the spatial (x) and spectral (ω) domains. The phase plate orientations are shown in the bottom of Fig. 4.1, where for the step plate, the adjustable angle α is with respect to the spectral (dispersion) direction. While the shaper imposes a spatiospectral (x,ω) at the phase spiral plate, leading to a spatiotemporal (x,τ) pulse immediately at its output at the exit grating (near field), our desired spatial effects appear in the far field of the shaper, where the desired STOV-carrying pulse emerges. Here, projection to the far field is achieved by focusing the shaper output, using lens L1, into the 500 μm fused silica witness plate, whereupon it is measured using TG-SSSI. In this context, the subscript on E_s can now be read as referring to a STOV-carrying pulse.

4.3 Experimental Results and Discussion

In Fig. 4.2 row (a) shows the pulse with no phase plate in the pulse shaper. This is the far-field output of the shaper as measured by TG-SSSI at the witness plate. The temporal leading edge is at $\tau < 0$. The left column shows $\Delta\phi(x,\tau)$. The fringes are

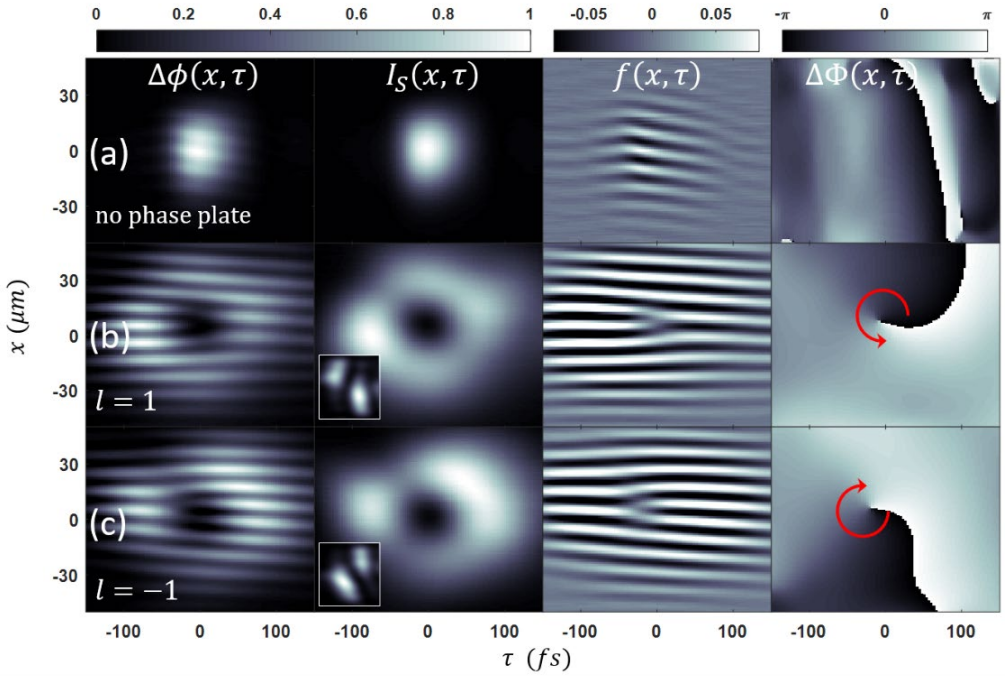

Figure 4.2. (a) Output of pulse shaper with no phase plate. The 50 fs input pulse, with a weakly parabolic temporal phase, is recovered. (b, c) Intensity and phase of pulse in far-field of pulse shaper with $l = 1$ and $l = -1$ spiral phase plates. White-bordered insets: pulse shaper near-field intensity images. The red arrows show the direction of phase circulation. Headings of each column are described in the text. In all panels, the temporal leading edge of the pulse is on the left ($\tau < 0$), so propagation is right-to-left. The pulse energy for the three far field cases above is ~1μJ. For the near field cases (insets), the pulse energy is increased to ~20μJ to offset the reduced signal due to magnification.

removed with a low-pass filter, yielding $I_s(x,\tau)$ in the next column, while in the third column, a high-pass filter leaves the fringe image $f(x,\tau)$. The far-right column shows the extracted spatiotemporal phase $\Delta\Phi(x,\tau)$. It is seen that the pulse envelope I_s

closely agrees with the 50 fs pulse input to the shaper, and that $\Delta\Phi(x,\tau)$ is weakly parabolic in time (small chirp) and relatively flat in space. The slight curvature of the fringes of $f(x,\tau)$ seen in Fig. 4.2 is attributed to a spectral phase mismatch between E_s and $\mathcal{E}_i$.

One form of line-STOV-carrying pulse can be generated with a spiral phase plate in the pulse shaper. For a $l = 1$ plate, row (b) of Fig.4.2 shows, as in (a), the various extractions from TG-SSSI. The presence of a spatiotemporal phase singularity is evident from the characteristic forked pattern in $f(x,\tau)$. The spatiotemporal envelope $I_s(x,\tau)$ and phase $\Delta\Phi(x,\tau)$ of the STOV are shown in the second and fourth columns, where the pulse appears as an edge-first flying donut with a 2π phase circulation around the phase singularity at the donut null. Using an $l = -1$ plate (flipping the $l = 1$ plate) generates the opposite spatiotemporal phase circulation, as seen in row (c). The small insets in (b) and (c) show the corresponding near-field intensity envelopes from the shaper (obtained by imaging the shaper output at the witness plate), consisting of two-lobes separated by a space-time diagonal.

Line-STOVs of charge $l = \pm 1$ can also be generated with a π-step phase plate in the shaper's Fourier plane, rotated to an angle α_{step} with respect to the grating dispersion direction, so that the step lies along the spatiospectral line $d\bar{x}/d\bar{\omega} = \mp\frac{1}{2}(x_s/x_0)(\tau_s/\tau_0)^{-1}$ (see discussion below), where x_0 and τ_0 are the widths and duration of the shaper input pulse, with $\bar{x} = x/x_0$ and $\bar{\omega} = \omega\tau_0$. In practice, α_{step} is finely adjusted to get a line-STOV output as measured by TG-SSSI. As seen in Fig.

3.3, for $\alpha_{step} = 25°$, the near-field output of the shaper is a flying donut [row (a)] with $l = 1$, while the lens-focused, far-field envelope [row (b)] is two lobes separated by a space-time diagonal. Going to $\alpha_{step} = -25°$ [row (c)] gives a STOV-carrying pulse envelope that is the spatial reflection of (b). In (b), it is seen that the vortex charge adds to $+1$ [consistent with (a)] and in (c) the charge adds to -1.

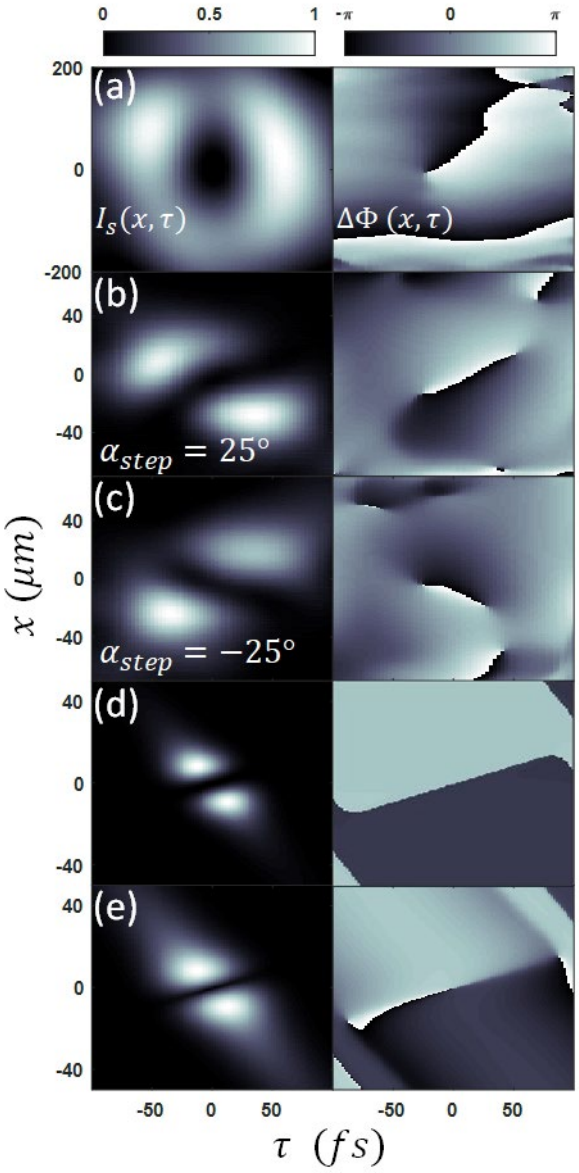

Fig 4.3. (a) Flying donut near-field intensity and phase from π-step pulse shaper, obtained from imaging shaper output into witness plate. (b, c) Offset lobe far-field intensity and phase, obtained by focusing shaper output into witness plate for step orientations $\alpha_{step} = \pm 25°$. (d) Simulation for $\alpha_{step} = +25°$ of far-field intensity and phase for (d) no dispersion, (e) group dispersion delay GDD=100 fs^2. The addition of parabolic temporal phase to the spatio-temporal phase step of (d) explains the phase pattern in (b, c). Headings of each column are described in the text. The pulse energy in panel (a) is ~20μJ and ~1μJ in panels (b) and (c). Propagation is right-to-left.

The near-field of the pulse shaper was simulated by Fourier-transforming an input spatiotemporal pulse $E_0(x,\tau)$ to the spatiospectral domain $\tilde{E}_0(x,\omega)$, applying the spatiospectral phase shift represented by the phase mask, along with any dispersion, and then Fourier-transforming the field back to the spatiotemporal domain as $E(x,\tau)$. Here the y dependence is ignored, which is near-Gaussian throughout. To simulate the far-field output of the shaper, the spatial Fourier-transform is applied $E(x,\tau) \rightarrow \tilde{E}(k_x,\tau) = E'(x',\tau)$, where $x' \propto k_x$ is the local transverse coordinate in the far field. Simulations of the far field of the π-step shaper are shown in panels (d) with no dispersion and (e) with group delay dispersion $\mathrm{GDD} = 100\ \mathrm{fs}^2$, corresponding to the measured $\Delta\Phi(x,\tau)$ in Fig. 4.3(a) The result of (d) is in agreement with the expression for $\tilde{E}(k_x,y,\tau)$, while (e) resembles the experimental result (b). The origin of this effect is that optimizing the SC pulse for TG-SSSI leaves the pump pulse with a very small chirp [parabolic phase in time, as seen in Fig. 4.3(a)]. Adding this phase to the diagonal π-step phase of 4.3(d) gives 4.3(e). Comparing Figs. 4.2 and 4.3, note that the π-step and $l = \pm 1$ spiral phase shaper outputs appear to be complementary: the near field one of these "quasi-modes" corresponds to the far-field of the other. As discussed, going from the Fourier plane in the shaper to the shaper output (near field) and then to the far field requires two transforms:$(x,\omega) \rightarrow (x,\tau) \rightarrow (k_x,\tau)$. If one were to start with Eq. (4.1) (for $l = \pm 1$) and ignore z, $x \rightarrow k_x$ yields $\tilde{E}(k_x,y,\tau) = a\left(\tau/\tau_s \pm \frac{1}{2}k_x x_0^2/x_s\right)\tilde{E}_0(k_x,y,\tau)$ and then $\tau \rightarrow \omega$ yields $\tilde{E}(k_x,y,\omega) = \frac{1}{2}a(i\omega\tau_0^2/\tau_s \pm k_x x_0^2/x_s)\tilde{E}_0(k_x,y,\omega)$ where we have assumed a pulse shaper input $E_0(\boldsymbol{r}_\perp,\tau) =$

$\epsilon(y)\exp(-(x/x_0)^2-(\tau/\tau_0)^2)$, with spatial and temporal widths x_0 and τ_0, and where $\epsilon(y)$ in this experiment is near-Gaussian ($\propto \exp(-(y/y_0)^2)$) but can be arbitrarily bounded. However we can swap $k_x \leftrightarrow 2ix/x_0^2$ and $\omega \leftrightarrow 2i\tau/\tau_0^2$ in any of these expressions to calculate the field at any location given either of the other two. Therefore, a flying donut STOV with an $l = \pm 1$ spiral phase in (x,τ) in the far field requires an $l = \pm 1$ spiral phase plate in (x,ω) in the shaper. A flying donut in (x,τ) in the near field then requires a π-step phase plate in (x,ω) in the shaper which yields spatiotemporally offset lobes in the far field separated by a π-step in phase.

To estimate the optimum angle α_{step} for the π-step plate to produce a near-field $l = \pm 1$ STOV at the shaper output, making the appropriate swap in the above expressions gives $\tilde{E}(x,y,\omega) = ia\left(\frac{1}{2}\omega\tau_0^2/\tau_s \pm x/x_s\right)\tilde{E}_0(x,y,\omega)$ at the phase plate, where a π phase shift occurs across the line $\frac{1}{2}\omega\tau_0^2/\tau_s \pm x/x_s = 0$. The spatiospectral orientation of the plate's π step is therefore $d\bar{x}/d\bar{\omega} = \mp\frac{1}{2}\,(x_s/x_0)(\tau_0/\tau_s)^{-1}$, as cited earlier, and clearly enables control of the STOV space-time aspect ratio. For example, we have observed that for $\alpha_{step} \to 0°$, the STOV appears as two lobes reflected across the time axis. This is consistent with $d\bar{x}/d\bar{\omega} \to 0$ and $\tau_0/\tau_s \to 0$, corresponding to extreme time-axis-stretching of the donut hole.

As most experiments with STOVs will take place in the far field of a pulse shaper, selecting among a flying donut, spatiotemporally offset lobes, or other possible space-time structures will depend on the far-field STOV profile desired for applications. In

any case, the electromagnetic angular momentum is conserved through the spatiotemporal/spatiospectral domains.

To visualize how a STOV-carrying pulse evolves from near field at the pulse shaper to the far field, 3D+time unidirectional pulse propagation equation (UPPE) propagation simulations [84,99] were performed as shown in Fig 4.4. The input to the shaper is $E_0(\boldsymbol{r}_\perp, \tau) = \varepsilon_0 \exp(-y^2/y_0^2 - x^2/x_0^2 - \tau^2/\tau_0^2)$, to which is applied the $l = +1$ spiral spatiospectral phase factor $\exp\big(i\Delta\phi(x,\omega)\big) = \mathbb{Z}/|\mathbb{Z}|$ (phase-only mask corresponding to the experiment), where $\mathbb{Z} = a\left(\frac{1}{2}\bar{\omega}(\tau_0/\tau_s) + i\bar{x}\,(x_0/x_s)\right)$, the prefactor of $\tilde{E}(x,y,\omega)$ as calculated using the theoretical treatment above. The pulse was then propagated to the far field through a 3 m lens at Rayleigh range $z_R = 2.3$ m (the finite memory of the (GPU)-based computer memory limited the simulations to lower spatial

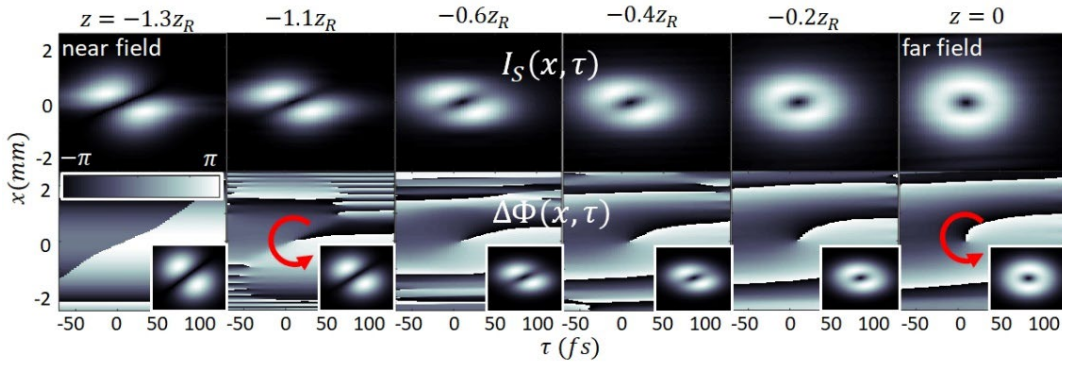

Figure 3.4. 3D+time UPPE simulation of STOV-carrying pulse launched from a pulse shaper with a $l = +1$ spatio-spectral spiral phase factor $e^{i\Delta\varphi(x,\omega)} = \mathbb{Z}/|\mathbb{Z}|$ corresponding to our experiment (see text). "Near-field" is right after a $3m$ lens at the pulse shaper output; "far-field" is at the lens focus. Rayleigh range is $z_R = 2.3m$. The propagation direction within each panel is right-to-left. Top row: intensity profiles $I_S(x,\tau)$. Bottom row: phase profiles $\Delta\Phi(x,\tau)$ with red arrows showing phase increase direction. Bottom row white-bordered insets: intensity profiles simulated using $l = +1$ spatio-spectral spiral phase factor $\mathbb{Z}$.

resolution, necessitating us of a long focal length lens). The top and bottom tow of panels in Fig. 4.4 show amplitude $I_s(x,\tau)$ and phase $\Delta\Phi(x,\tau)$ of the STOV. The y dependence maintains its Gaussian envelope. The white-bordered insets in the bottom row show simulations with the phase *and* amplitude mask $\mathbb{Z}$ applied, corresponding to our theoretical treatment above, which is based on the form of STOV assumed in Eq. (4.1). The results for both masks are very similar and either works to generate STOVs. The simulation clearly shows the continuous evolution of the STOV pulse from space-time diagonally-separated lobes to donut, with the STOV angular momentum conserved throughout. It is important to reiterate that while the form of STOV assumed in Eq. (4.1) necessitates a spatiospectral phase and amplitude mask of form $\mathbb{Z}$, the experiment actually uses a pure phase mask $\mathbb{Z}/|\mathbb{Z}|$ - that is the (x,ω) pulse profile is matched to the phase plate profile – but as shown by the 3D+time propagation simulations, this leads to very similar results.

The transformation of one quasi-mode into the other can be viewed as STOV mediation of energy flow within the pulse. In a frame moving at the pulse group velocity as shown in [88] and more recently applied to STOVs [24,30], the local energy density flux consistent with the paraxial wave equation is $\mathbf{J} = (c/8\pi k_0)|E_s|^2\left(\nabla_\perp\Phi_{st} - \beta_2(\partial\Phi_{st}/\partial\xi)\hat{\boldsymbol{\xi}}\right)$, where $\xi = v_g t - z$, Φ_{st} is the spatiotemporal phase [see Eq. (4.1)], $\hat{\boldsymbol{\xi}}$ is a unit vector along ξ, and $\beta_2 = v_g^2 k_0(\partial^2 k/\partial\omega^2)_0$ is the normalized group velocity dispersion, where $\beta_2^{air} \approx 10^{-5}$ and $\beta_2^{glass} \approx 10^{-2}$. Because the first term in **J** is dominant for both air and glass, the weakly

saddle-shaped energy flow [24,30] is mostly along $\pm x$, providing the necessary transformation from donut to spatiotemporally offset lobes and back again. This is a remarkable effect: we note that in a STOV-free beam, the term $\nabla_{\perp}\Phi$ would act on a local spatial phase curvature to transversely direct energy (diffract) to both transverse directions with respect to the direction of the beam propagation (here $\pm x$ and $\pm y$). However, in an $l = 1$ linear STOV whose axis is along y [see Fig. 4.2(b)], $\nabla_{\perp}\Phi$ points along $(-x)$ in front of the pulse and along $(+x)$ in the back, directing energy density to one side in the front of the pulse and the opposite side in the back. This is seen in the transformation of the spatiotemporally offset lobes from the near field [Fig. 4.2(b) inset image] to the far-field flying donut. Similar dynamics apply to the $l = -1$ STOV of Fig. 4.2(c), and to the $l = 1$ STOV of Figs. 4.2(a) and 4.2(b).

To explore higher-order STOVs, we use an $l = 8$, (16π) spiral phase plate in the pulse shaper. Figure 4.5(a) shows the near-field intensity envelope and phase, while 4.5(b) shows the intensity and phase in the far-field. In the near field, as shown in (a), six π-step phase jumps appear, corresponding to nulls in the intensity envelope (rather than eight because the SC probe pulse underfilled the larger image of the exit grating in the witness plate). In the far field, where the SC probe pulse overfilled the pump pulse, enabling coverage of all the vortices, it is seen that the pulse has formed eight $l = +1$ STOVs. Such splitting of high-charge vortices into multiple single-charge vortices has been explained for standard monochromatic OAM as originating from interference with a coherent background, or with a coherent probe beam used to measure the presence of vortices [100].

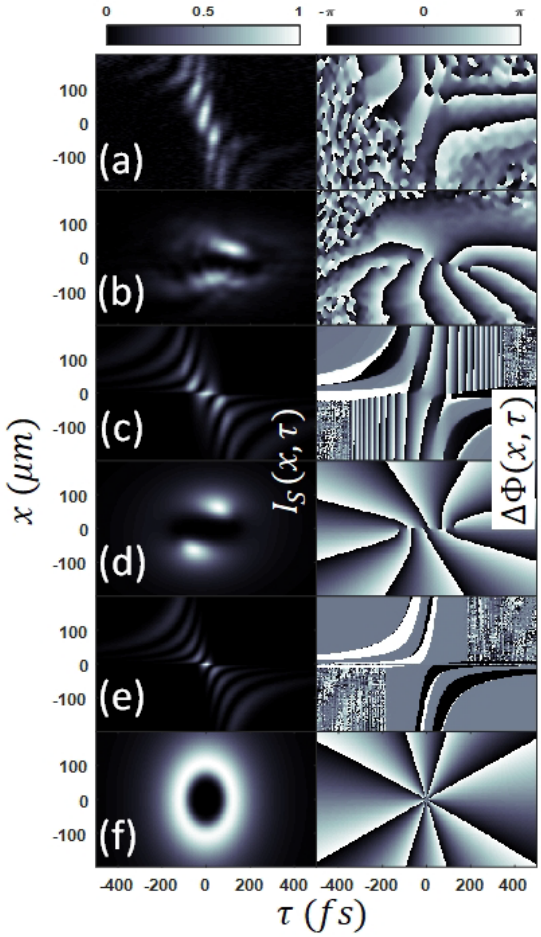

Figure 4.5. Results from pulse shaper with $l = 8$ spiral phase plate. Pulse propagation is right-to-left. Left column: intensity profiles $I_S(x, \tau)$. Right column: phase profiles $\Delta\Phi(x, \tau)$. All profiles are spatially rescaled for comparison. (a) Near-field intensity and phase of shaper output, obtained from imaging exit grating onto witness plate. The $l = 8$ vortex appears as eight π-step phase jumps (only 6 visible owing to underfilling of image by probe SC pulse). Laser pulse energy ~20 μJ. (b) Far-field intensity and phase obtained by focusing shaper output into witness plate. Here, eight $l = 1$ STOVs are seen in the phase plot (here, the SC reference pulse profile overfills the smaller spot). Laser pulse energy ~2 μJ. (c,d) Fourier transform simulation of near-field and far-field intensity and phase where the (x, ω) spatial profile of the pulse in the shaper is *not* matched to the phase mask. (e,f) Fourier transform simulation of near-field and far-field intensity and phase where the (x, ω) pulse profile in the shaper *is* matched to the phase plate.

In this case, the splitting has a different origin: a mismatch of the (x, ω) beam profile in the pulse shaper to the profile of the $l = 8$ spiral phase plate. While this mismatch has only minor effects for generating $l = 1$ STOVs, as discussed in the context of Fig 4.4, it reveals itself for higher-order STOVs. Fourier transform simulations, including glass dispersion, are shown in Fig 3.5(c) and 3.5(d) for the near and far fields, reproducing the main features of the measurements, including the "splitting" into eight $l = +1$ vortices. The (x, ω) beam profile-phase plate mismatch leads to slightly different orientations of adjacent pairs of near-field lobes in Fig. 4.5(a) [4.5(c)]; these form slightly displaced $l = 1$ windings in the far field in Fig. 4.5(b) [5(d)]. So in this case, it appears that the $l = 8$ STOV never forms and eight $l = 1$ STOVs are formed directly. It is expected that with dispersion management and a better match of the spatiospectral beam profile with that of the phase plate will enable generation of high order STOVs that can propagate into the far field. This is shown in the simulations of Fig. 4.5(e) and 4.5(f) for the case where the spatiospectral profile and the phase plate are matched: an $l = 8$ flying donut is formed, accompanied by a single vortex of the same charge.

4.4 Conclusion

In conclusion, the linear generation and propagation in free space of pulses that carry a new type of optical OAM whose associated vortex phase circulation exists in space-time has been demonstrated. These measurements show that freely propagating STOVs conserve angular momentum in space-time and mediate space-time energy flow within

the pulse. It was also through this work that a new ultrafast diagnostic, TG-SSSI was first demonstrated to measure the space- and time-resolved amplitude and phase of a STOV in a single shot. It is anticipated the study of nonlinear propagation of STOV-carrying pulses, as well as the propagation of STOVs through fluctuating media will provide a rich area of study, and in such experiments, sensitive to shot-to-shot fluctuations, TG-SSSI will be an important tool.

Chapter 5: Second-harmonics from spatiotemporal optical vortices

5.1 Introduction

Since we have demonstrated the linear generation of STOVs and their linear free-space propagation in the previous chapter, the next logical step is to examine their nonlinear propagation. In this chapter, SHG of STOVs are examined experimentally using TG-SSSI [28]. Additionally, simulations exploring the conservation process and the propagation of STOVs in material media are presented.

The SHG photons carry twice the OAM of the fundamental beam photons ($m\hbar \rightarrow 2m\hbar$) [101–105], where l is the beam topological charge. Similarly, in sum and difference frequency generation, the OAM of the two fundamental modes are added or subtracted respectively [106]. In the case of q^{th}-order high harmonic generation with mode of charge m, the resulting photons have OAM $qm\hbar$ [107–110]. The conservation of OAM in nonlinear interactions has prompted the measurements of harmonic generation and OAM conservation with STOV-carrying pulses as first presented in [31,111,112], confirmed in [113], and a theoretical treatment of high harmonic generation using STOVs [114].

Because SHG is fundamentally an interaction process of the quantized electromagnetic field, and because all photons in the STOV pulse from the pulse shaper carry the same bandwidth, polarization, and spatiotemporal (or spatiospectral) phase,

these results verify that individual photons can have OAM orthogonal to their direction of propagation.

5.2 Analytic Evaluation of Second Harmonic Generation of STOVs

A STOV-carrying pulse of center wavenumber k_0 at position $|z| \ll z_R$ along the propagation axis (strongly satisfied in these experiments) can be written as [27]

$$E_s(\boldsymbol{r}_\perp, z, \tau) = a\left(\frac{\tau}{\tau_s} \pm \mathrm{sgn}(l)\frac{x}{x_s}\right)^{|l|} \exp(ik_0 z)\ E_0(\boldsymbol{r}_\perp, z, \tau) \tag{5.1}$$

$$= A(x,\tau)\exp\big(il\Phi_{st}(x,\tau)\big)\exp(ik_0 z)\,E_0(\boldsymbol{r}_\perp, z, \tau),$$

where z_R is the Rayleigh range, $\boldsymbol{r}_\perp = (x, y)$, $\tau = t - z/v_g$ is a time coordinate local to the pulse, v_g is the group velocity, τ_s and x_s are the temporal and spatial scale widths of the STOV, $\Phi_{st}(x,\tau)$ is the spacetime phase circulation in $x-\tau$ space, the integer, l, is the topological charge of the STOV, $A(x,\tau) = a((\tau/\tau_s)^2 + (x/x_s)^2)^{|l|/2}$, $a = \sqrt{2}\left(\left(\frac{x_0}{x_s}\right)^2 + \left(\frac{\tau_0}{\tau_s}\right)^2\right)^{-1/2}$ for $l = \pm 1$, and E_0 is the STOV-free Gaussian pulse input to the pulse shaper, where x_0 and τ_0 are the spatial and temporal widths of the pulse [27]. Here, a is a normalization factor ensuring energy conservation through the pulse shaper. The propagation phase factor $\exp(ik_0 z)$ contributes to extrinsic OAM, and not to the SHG process.

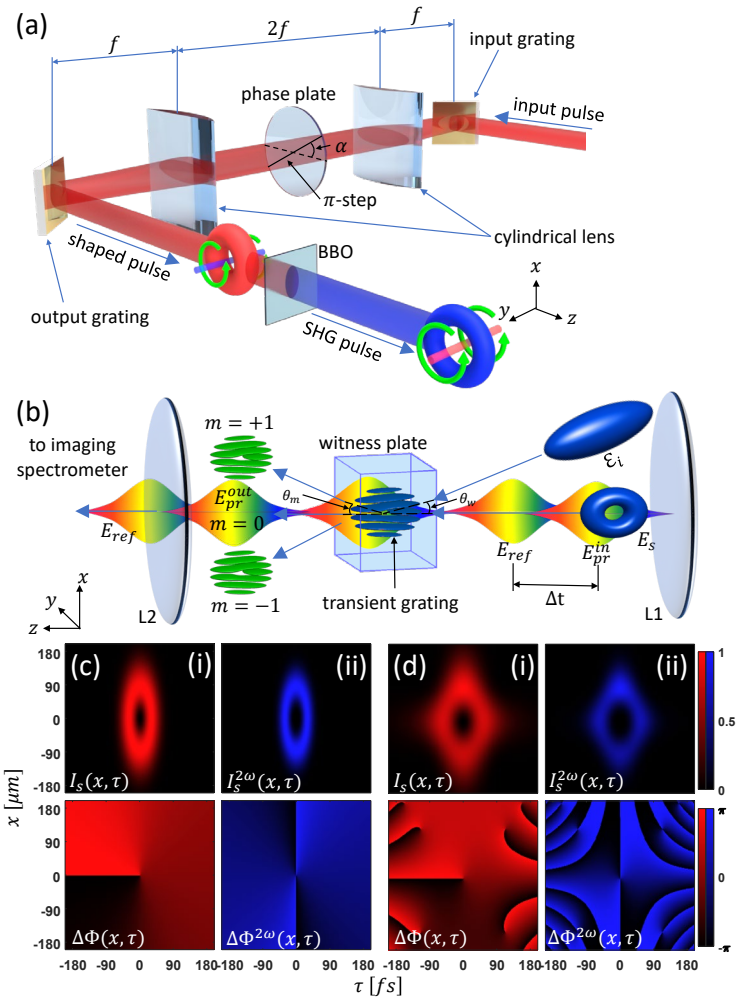

Figure 5.1. (a) 4f pulse shaper used to generate a $l = \pm 1$ STOV-carrying pulse at 800nm, composed of two 1200 groove/mm gratings, two $f = 10$ cm cylindrical lenses and a transmissive π-step phase plate. The fused silica phase plate has an 882nm step oriented at $\pm 40°$ to the grating dispersion direction. A 100μm thick BBO crystal is located 20cm from the output grating. (b) TG-SSSI setup, with elements described in the main text. (c) Idealized spatiotemporal intensity $I(x,\tau) \propto |E|^2$ and phase $\Delta\Phi(x,\tau)$ of (i) E_S ($l = +1$) described by Eq. (5.1) and (ii) $E_S^{2\omega}$ ($l = +2$). (d) Spatiotemporal intensity and phase of (i) E_S ($l = +1$) and (ii) $E_S^{2\omega}$ ($l = +2$) from simulation (See Sec. 5.6) of our pulse shaper, followed by SHG in the nonlinear BBO crystal with $\mathrm{GVM}_{\mathrm{BBO}} = 0$ and $\mathrm{GDD}_{\mathrm{BBO}} = 0$. Here, the diamond-like donut shape of $I_S(x,\tau)$ and $I_S^{2\omega}(x,\tau)$ stems from the contribution of higher order Hermite-Gaussian modes generated from the π-step phase plate and superimposed on the STOV.

The well-known SHG process [115], as applied to the fundamental STOV pulse of Eq. (5.1), would give $E_s^{2\omega}(\boldsymbol{r}_\perp, z, \tau) \propto A^2(x,\tau)\exp\big(i2l\Phi_{st}(x,\tau)\big)E_0^2(\boldsymbol{r}_\perp, z, \tau)$, assuming perfect phase matching and an undepleting pump. This result is plotted in Fig. 5.1(c), which shows the intensity and phase of the fundamental [red colormap (i)] and the second-harmonic fields [blue colormap (ii)]. The 2π phase winding of E_s is transformed into a 4π phase winding of $E_s^{2\omega}$, accompanied by a narrowing of the intensity ring by a factor of $\sqrt{2}$. Because this pulse shaper modulates only the input pulse phase and not its amplitude, the STOVs it generates are not fully symmetric as shown in the pulse shaper simulation of Fig. 5.1(d-i). (See Sec. 5.6) The diamond-shaped spacetime donut - reproduced in the measurements later – results from beam contributions by higher-order Hermite-Gaussian modes generated at each frequency by the π step of the phase plate. The corresponding second-harmonic field of the shaper output is shown in Fig. 5.1(d-i).

5.3 Measurement of SHG of STOV

5.3.1 Experimental Setup

Fundamental ($\lambda_0 = 800$ nm) STOVs with electric field E_s were generated from 50 fs pulses from a 1 kHz Ti:sapphire amplifier routed through the $4f$ pulse shaper depicted in Fig. 5.1(a) and previously presented in Refs. [26,27,57]. The key feature of the pulse shaper is the transmissive fused silica phase plate at the common focus of the cylindrical lenses (the Fourier plane of the pulse shaper). The phase plate has a π step

of height $\lambda_0/2(n_{\mathrm{FS}}-1) \approx 882$ nm (where $n_{\mathrm{FS}} = 1.4533$ is the refractive index of the substrate at 800 nm) across its diameter. Orienting the step at $\alpha = \pm 40^{\circ}$ to the dispersion direction of the input diffraction grating generates fundamental STOVs E_s with topological charge $l = \pm 1$ in the near field of the pulse shaper. Alternatively, a spiral phase plate could have been used to generate a similar STOV pulse in the far field of the shaper [27,57]. The angle α depends on the beam diameter and spectral resolution of the pulse shaper and is tuned experimentally. SHG of E_s was accomplished by placing a 100 μm thick, type I beta-barium borate (BBO) crystal at the immediate output of the $4f$ pulse shaper in the near field. The crystal was sufficiently thin to ensure SHG phase matching over the full pulse bandwidth. *It is important to stress here that a well-aligned, ideal pulse shaper of this type* [26,27,57] *imposes the same bandwidth, spatiotemporal phase and polarization on all output photons.* In addition, the photons have a purely spatial phase, which is related to their extrinsic OAM. Minus this component, STOV-based OAM is intrinsic, and it is the intrinsic part of the OAM that is responsible for angular momentum conservation under SHG.

In order to observe the spatiotemporal phase and amplitude of the fundamental and SHG STOVs, the use of transient-grating single-shot supercontinuum spectral interferometry (TG-SSSI) was employed, a technique developed for measuring pulses containing spatiotemporal phase singularities [27,28] and is discussed in Chapter 2. TG-SSSI enables the single shot measurement of the phase $\Delta\Phi(x,\tau)$ and intensity $I(x,\tau)$ profiles of ultrashort pulses, where x is a space dimension orthogonal to pulse

propagation [as shown in Fig. 5.1(a)] and τ is the local time in the pulse frame. As shown in the TG-SSSI setup depicted in Fig. 5.1(b), either E_s or its second harmonic $E_s^{2\omega}$ is imaged by a low dispersion MgF_2 lens (L1) into the "witness plate," where it interferes with a spatial reference pulse $\mathcal{E}_i$ to form a transient volume grating. Spectral interferometry using probe and reference supercontinuum pulses E_{pr} and E_{ref} was performed on the transient-grating, enabling extraction of $\Delta\Phi(x,\tau)$ and $|E_s(x,\tau)|^2 \propto I(x,\tau)$ (or $\Delta\Phi^{2\omega}(x,\tau)$ and $|E_s^{2\omega}(x,\tau)|^2$) [27,28]. In this TG-SSSI iteration, the setup can measure pulses as short as $\sim$11 fs at the fundamental ($\sim$27 fs at the second harmonic). For adequate signal-to-noise ratio, the lowest pulse energy measured here was 3 μJ, corresponding to a peak intensity of $\sim 150\ \mathrm{GW/cm^2}$.

5.3.2 Experimental Results

The TG-SSSI measurements of the fundamental and SHG STOVs are shown in Fig. 5.2, where the red colormap panels of (a) show the spatiotemporal intensity $I_s(x,\tau)$ and phase $\Delta\Phi(x,\tau)$ of the fundamental $l = +1$ STOV $E_s(x,\tau)$ at the near-field output of the $4f$ pulse shaper. $I_s(x,\tau)$ has the characteristic edge-first "flying-doughnut" profile, with the pulse propagating right to left, while $\Delta\Phi(x,\tau)$ is a single 2π winding centered at $(x,\tau) = (0,0)$. The dip in intensity near $x = -60$ μm in Fig. 5.2(a) is due to scattering off the π step of the phase plate. Figure 4.2(b), in the blue colormap, shows the measured spatiotemporal intensity $I_s^{2\omega}(x,\tau)$ and phase $\Delta\Phi^{2\omega}(x,\tau)$ of $E_s^{2\omega}(x,\tau)$. Instead of a single 4π phase winding [as in Fig. 5.1(c) and 5.1(d)], we see that $I_s^{2\omega}(x,\tau)$ and $\Delta\Phi^{2\omega}(x,\tau)$ show two spatiotemporally offset vortices, embedded in the second

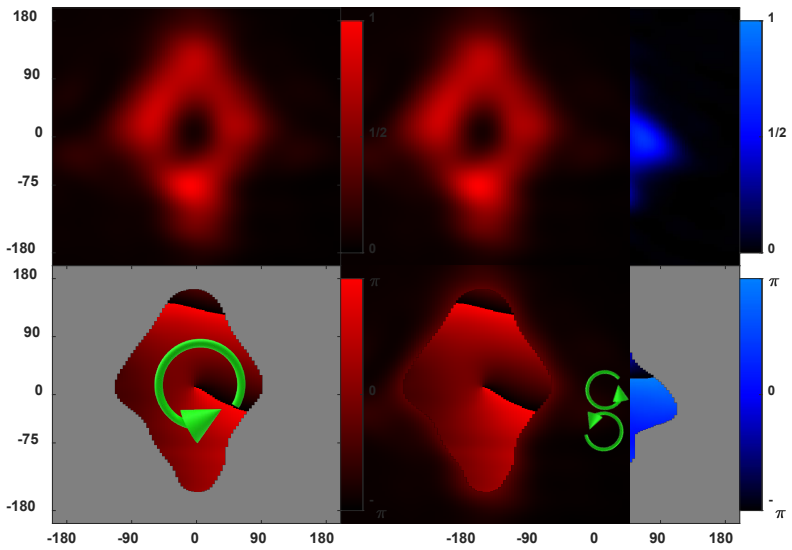

Figure 5.2. TG-SSSI measurements of fundamental and SHG STOVs. (a) Top: Intensity profile $I_S(x,\tau)$ of fundamental $l = +1$ STOV; Bottom: spatiotemporal phase $\Delta\Phi(x,\tau)$ showing one 2π winding. (b) Top: SHG output pulse $I_S^{2\omega}(x,\tau)$ showing two donut holes embedded in pulse; Bottom: spatiotemporal phase profile $\Delta\Phi^{2\omega}(x,\tau)$ showing two 2π windings. Phase traces are blanked in regions of negligible intensity, where phase extraction fails. These images represent 500 shot averages: the extracted phase shift from each spectral interferogram is extracted, then the fringes of each frame (shot) are aligned and averaged, then the phase map is extracted [28].

harmonic pulse, around whose centers are two 2π phase windings. This constitutes two $l = +1$ STOVs, ad thus energy conservation dictates that the $E_s^{2\omega}$ pulse carries on average, twice the OAM per photon of the fundamental E_s.

The spatiotemporal splitting of the STOV in $E_s^{2\omega}$ is due to (1) group velocity mismatch (GVM) ($= 1/v_g^{(2\omega)} - 1/v_g^{(\omega)}$) between the E_s and $E_s^{2\omega}$ pulses in the BBO crystal during SHG [116] and (2) group delay dispersion (GDD) in both the BBO and the lens L1. These effects are explored next through simulations.

5.4 Simulation of SHG of STOV

The mechanics phase winding splitting during SHG of STOVs and their subsequent propagation was examined by spectral domain [$\tau \to \omega$ and $\boldsymbol{r}_\perp \to \boldsymbol{k}_\perp = (k_x, k_y)$] simulations using the carrier resolved unidirectional pulse propagation equation (UPPE) algorithm [83] of the 3D system of propagation equations.

$$\frac{\partial \tilde{\mathbf{E}}}{\partial z} = iK_z(\omega, k_\perp)\tilde{\mathbf{E}} + \frac{i2\pi}{K_z(\omega, k_\perp)}\frac{\omega^2}{c^2}\tilde{\mathbf{P}}, \tag{5.2}$$

for the fields $\tilde{\mathbf{E}} = \hat{\boldsymbol{y}}E_s$ or $\tilde{\mathbf{E}} = \hat{\boldsymbol{x}}E_s^{2\omega}$. Here $K_z(\omega, \boldsymbol{k}_\perp) = \sqrt{k^2(\omega) - |k_\perp|^2}$ is the linear propagator in the spectral domain, $k(\omega) = \omega n(\omega)/c$ is the wavenumber (with dispersion in BBO and MgF_2 lens L1 provided by Refs. [116] and [117]), and $\tilde{\mathbf{P}}$ is the nonlinear polarization for the BBO portion of the propagation, where the orthogonally polarized E_s and $E_s^{2\omega}$ fields are computed in the spatiotemporal domain and coupled through

$$P_y = \chi^{(2)}_{yxy}(-\omega; 2\omega, -\omega)E_x E_y^* \exp\left[-i\left(k_y + k_y - k_x\right)z\right], \tag{5.3a}$$

$$P_x = \chi^{(2)}_{\mathrm{xyy}}(-2\omega; \omega, \omega)E_y^2 \exp\left[i\left(k_y + k_y - k_x\right)z\right], \tag{5.3b}$$

where $\chi^{(2)}$ is the second-order susceptibility tensor for BBO [118].

Owing to symmetry along y, $\partial\tilde{\mathbf{E}}/\partial y = 0$ was used, which also reduces the computational load. The simulation (see Sec. 5.6) generates E_s in the pulse shaper, propagates it through the BBO while generating $E_s^{2\omega}$, and then propagates the fields through the MgF_2 lens to the witness plate. The initial conditions at the entrance to the pulse shaper are $\hat{\boldsymbol{x}}\,E_x = 0$ and $\hat{\boldsymbol{y}}\,E_0$ is a plane wave with wavevector $(0,0,k_0)$, where

$|E_0|^2$ is a Gaussian corresponding to the experiment's 3.2 mm $1/e^2$ beam radius, 50 fs pulse width, and 350 μJ energy.

These simulations generating $E_s^{2\omega}(\boldsymbol{r}_\perp, z, \tau)$ show that for the case of zero dispersion ($\mathrm{GVM_{BBO}} = 0$, $\mathrm{GVD_{BBO}} = 0$, and $\mathrm{GDD_{L1}} = 0$), the $l = +2$ STOV does not break up for BBO crystal thickness less than ~100 μm. This is seen in Fig. 5.3(a) for two BBO thicknesses, 20 μm and 100 μm. The $\Delta\Phi^{2\omega}(x, \tau)$ plots are zoomed in near the phase singularity, while the insets show the full intensity profile.

Figure 5.3(b) shows a simulation for the non-physical case of $\mathrm{GVM_{BBO}} = 0.19\ \mathrm{fs^2/\mu m}$ and $\mathrm{GVD_{BBO}} = 0$. It is concluded that nonzero $\mathrm{GVM_{BBO}}$ is sufficient to break the $l = +2$ STOV into two $l = +1$ STOs in as little as 20 μm of propagation in BBO. Including $\mathrm{GVD_{BB0}} = 0.209\ \mathrm{fs^2/\mu m}$ in the simulation [Fig 5.3(c)] shows the separation of the two windings relative to the case in Fig 5.3(b). Note that for $I_s^{2\omega}(x, \tau)$ [insets of (a), (b), and (c)], the two field nulls are resolvable only into one central null.

A simulation corresponding directly to Fig. 5.2's experimental parameters is shown in Fig. 5.3(d), where $\mathrm{GDD_{L1}} = 350\ \mathrm{fs^2}$ and $\mathrm{GDD_{air}} = 250\ \mathrm{fs^2}$ are included. Here, the already separated $l = +1$ STOVs are driven farther apart by the additional dispersion from linear propagation in air and through the MgF_2 lens, leading to two spatiotemporally offset nulls in $I_s^{2\omega}(x, \tau)$. Because of linear propagation in L1 and air, GDD has a different effect than the interplay of $\mathrm{GVM_{BBO}}$ and $\mathrm{GVD_{BBO}}$ on vortex separation during nonlinear propagation [Fig. 5.3(c)]. Comparing the results in Fig. 5.2(b) and 5.3(c), the simulation matches the experiment quite well.

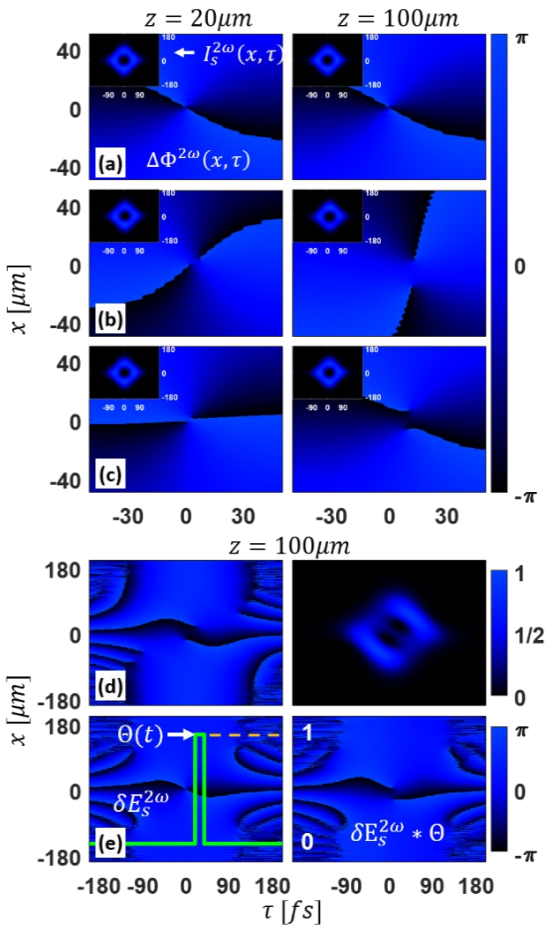

Figure 5.3. Simulation (See Sec. 5.6) of the SHG of a fundamental $l = +1$ STOV E_S. Plotted is $I_S^{2\omega}(x,\tau) \propto |E_S^{2\omega}|^2$ and $\Delta\Phi^{2\omega}(x,\tau)$, the intensity and phase of the simulated SHG pulse. The simulation generates E_S in the pulse shaper, propagates it through the BBO while generating $E_S^{2\omega}$, and then propagates the fields through MgF_2 lens L1 to the witness plate. The phase images are zoomed in at the null to show the decomposition of the high order STOV. (a) $\mathrm{GVM_{BBO}} = 0$, $\mathrm{GDD_{BBO}} = 0$, $\mathrm{GDD_{L1}} = 0$. The $l = 2$ STOV does not break up regardless of the BBO thickness, here for 20μm (left) and 100μm (right). Insets: $I_S^{2\omega}(x,\tau)$, with horizontal $\tau(fs)$ and vertical $x\ (\mu m)$ scales. (b) $\mathrm{GVM_{BBO}} = 0.19\ \mathrm{fs^2/\mu m}$, GDDBBO=0, and GDDL1 =0. Here, the $l = 2$ STOV breaks up into two $l = 1$ STOVs in as little as 20μm of propagation in BBO. (c) $\mathrm{GVM_{BBO}} = 0.19\ \mathrm{fs^2/\mu m}$, $\mathrm{GDD_{BBO}} = 20.9\ \mathrm{fs^2}$, and $\mathrm{GDD_{L1}} = 0$. (d) Simulation corresponding to experimental parameters of Fig. 5.2: $\mathrm{GVM_{BBO}} = 0.19\ \mathrm{fs^2/\mu m}$, $\mathrm{GDD_{BBO}} = 20.9\ \mathrm{fs^2}$, $\mathrm{GDD_{air}} = 250\ \mathrm{fs^2}$ and $\mathrm{GDD_{L1}} = 350\ \mathrm{fs^2}$. (e) Simple convolution model of the effect of GVM in BBO, showing decomposition of $l = +2$ STOV into two $l = +1$ STOVs.

The effect of GVM in the BBO on the decomposition of an $l = +2$ STOV can be explained as follows: As E_s propagates in the BBO, eash portion of its envelope at local time τ nonlinearly generates a contribution $\delta E_s^{2\omega}$ that slips back in time with respect to the group velocity frame of the fundamental. The SHG crystal output can then be constructed as the convolution integral $E_s^{2\omega}(x,\tau) = \int_{-\infty}^{\tau} \delta E_s^{2\omega}(x,\tau - t)\Theta(t)dt$, the sum of a sequence of time-shifted $l = +2$ STOV contributions $\delta E_s^{2\omega}(x,\tau - t)$ that models the increasing slip of the peak of $E_s^{2\omega}$ with respect to the peak of E_s. Here, $\Theta(t)$=1 for $0 \leq t \leq \Delta\tau$, and $\Theta(t) = 0$ elsewhere, where the maximum time slip is $\Delta\tau = \left(1/v_g^{(2\omega)} - 1/v_g^{(\omega)}\right)L \approx 19$ fs for the SHG BBO crystal length $L = 100$ μm. The integral yields two spatially offset $l = +1$ phase windings as depicted in Fig. 5.3(d). This is essentially the STOV equivalent to the splitting observed due to spatial walk-off of LG beams in nonlinear crystals [119]. The additional nonzero GDD_{L1} leads to the diagonal (spatiotemporal) offset of Fig. 5.3(c). Recognizing from Fig. 5.3 that the two spatially offset $l = +1$ phase windings represents a superposition of time-shifted $l = +2$ STOV pulses, we find that OAM conservation in SHG also applies to STOVs.

5.5 Conclusion

In summary, the conservation of STOV-based OAM in SHG, has been experimentally and theoretically demonstrated. GVM between the fundamental and second-harmonic STOVs is the primary cause for $l = +2$ STOVs to quickly separate into two $l = +1$ STOVs after only a short propagation distance in the SHG crystal. The spacetime

separation of STOVs during SHG could possibly be mitigated by using noncollinear SHG geometry.

The question of whether photons in an ultrashort STOV pulse individually carry transverse OAM is difficult to answer experimentally using linear optics; this question is more easily answered with the help of nonlinear optics. The conservation of photon number implied by the Manley-Rowe relation for SHG, $2d/dz\left(I^{(\omega)}/\hbar\omega\right) = d/dz\left(I^{(2\omega)}/\hbar\omega\right)$ [115], implies that, *on average*, photons at the second harmonic carry twice the OAM of photons at the fundamental. However, because SHG is fundamentally a quantum mechanical process involving light-matter interactions of quantized electromagnetic fields, and because all photons in the STOV pulse from the pulse shaper carry the same bandwidth, polarization, and spatiotemporal phase, we conclude that energy and angular momentum conservation in the SHG process holds at the individual photon level – and that photons in STOV-carrying pulses have OAM orthogonal to their direction of propagation. The uncertainty relations $\Delta k_x \Delta x \geq 1/2$ and $\Delta k_\xi \Delta \xi \geq 1/2$ ensure that a photon with STOV OAM could be found anywhere in the transverse and longitudinal extent of the pulse, and it could have any frequency consistent with the bandwidth.

5.6 Additional Material:

B.1 Second Harmonic Generation Propagation Simulations

Propagation simulations of this chapter employed the Unidirectional Pulse Propagation Approximation (UPPE) algorithm [83], a fully spectral method for simulation of linear and nonlinear propagation of ultrashort laser pulses. UPPE simulated (1) nonlinear propagation of the fundamental $l = 1$ STOV E_S through the BBO and generation of the SHG field $E_S^{2\omega}$ (2), linear propagation from the exit face of the BBO through lens L1 to the witness plate of TG-SSSI (See Fig. 5.1 in Sec. 5.2). UPPE can be implemented in multiple ways (scalar or vectorial, envelope or carrier resolving), none of which require the beams to be paraxial. The only assumption made is unidirectional propagation of pulses. For the simulations of this chapter, we implemented a carrier-resolving scalar UPPE solver.

Assuming $\mathbf{E}(x, y, t, z)$ is the electric field of the laser pulse (including the carrier) and $\tilde{\mathbf{E}}(k_x, k_y, \omega, z)$ is its Fourier transform in time ($t \to \omega$) and transverse space ($\{x, y\} \to \{k_x, k_y\} = \{\mathbf{k}_\perp\}$) we have

$$\partial\tilde{\mathbf{E}}/\partial z = iK_z(\omega, \mathbf{k}_\perp)\tilde{\mathbf{E}} + i2\pi\, K_z^{-1}(\omega, \mathbf{k}_\perp)(\omega^2/c^2)\widetilde{\mathbf{P}}, \tag{B1}$$

where $K_z(\omega, \boldsymbol{k}_\perp) = \sqrt{k^2(\omega) - |\mathbf{k}_\perp|^2}$ models diffraction and dispersion and $\widetilde{\mathbf{P}}$ is the nonlinear polarization. The advantage of solving spectral domain Eq. (B1) is the decoupling of field values from their adjacent values (in ω and $\mathbf{k}_\perp$). Only the history of the fields $\tilde{\mathbf{E}}$ and $\widetilde{\mathbf{P}}$ at a given spectral point $(\omega, \mathbf{k}_\perp, z)$ determines the value of

$(\omega, \mathbf{k}_\perp, z + \Delta z)$ through simple integration. Depending on the type of nonlinearity modeled, it is convenient to calculate the polarization in either the spatio-temporal domain ($\mathbf{P}$) or the spatio-spectral domain ($\widetilde{\mathbf{P}}$). For nonlinear propagation through the BBO crystal, $\mathbf{P}$ is calculated in the space-time domain since the pulse is polychromatic, and is given by

$$P_y = \chi^{(2)}_{yxy}(-\omega;\ 2\omega, -\omega) E_x E_y^*\, e^{-i(k_y + k_y - k_x)z},$$

$$P_x = (1/2)\chi^{(2)}_{xyy}(-2\omega;\ \omega, \omega) E_y^2 e^{i(k_y + k_y - k_x)z},$$

while it is $\mathbf{P} = \mathbf{0}$ in the linear part of the propagation. For inclusion in Eq. (5.1) of Sec. 5.2, $\mathbf{P}$ is Fourier transformed to $\widetilde{\mathbf{P}}$, as shown there. To apply our simulations to y-symmetric STOVs we use $\partial \widetilde{\mathrm{E}}/\partial y = 0$ ($k_y = 0$), thereby reducing the simulations to a 2D slice through the pulse at $y = 0$.

B.2 Pulse Shaper Simulations

Pulse shaper simulation was performed by applying a π-step phase to a simulated Gaussian pulse in the spatio-spectral domain. The pulse parameters used were: $\tau_{FWHM} = 70$fs, $x_{FWHM} = 4$mm (both for intensity envelope), central wavelength λ_0 = 800nm, and grating period $\Lambda = 1/1200$ mm. The input field into the pulse shaper is $E_0(x, \tau) = E_0 \exp(-x^2/2\sigma_x^2 - \tau^2/2\sigma_\tau^2 + i\omega_0\tau)$, where $\sigma_x = x_{FWHM}/2\sqrt{\ln(2)}$, $\sigma_\tau = \tau_{FWHM}/2\sqrt{\ln(2)}$ and $\omega_0 = 2\pi c/\lambda_0$. An input grating angle of $\theta_i = -10°$ was assumed and the first order diffraction angle is given as $\theta_1(\lambda) = \sin^{-1}(-\lambda/\Lambda - \sin\theta_i)$. Referenced to λ_0 in the first order, the angle is $\Delta\theta_1(\lambda) = \theta_1(\lambda) - \theta_1(\lambda_0)$. The

spatial location of the dispersed ray at the π-step phase plate is $y = f \tan \Delta\theta_1(\lambda)$, where $\lambda = 2\pi c/\omega$, and $f = 100$mm is the focal length of the cylindrical lens. The phase plate is rotated at an angle α relative to the dispersion direction of the grating, and the phase shift it imparts to the beam is computed as $A(x, y) = 0$ for $x < y \tan \alpha$ and $A(x, y) = \pi$ for $x > y \tan \alpha$, where $E_{out}(x, \tau) = \mathcal{F}_\omega^{-1}\left[\mathcal{F}_\tau[E(x, \tau)] \exp\left(iA(x, y)\right)\right]$.

Simulating the scattering off of the $\boldsymbol{\pi}$-step on the phase plate was similarly done by defining a mask $B(x, y) = 0$ for $|x - y \tan \alpha| \leq w/2$ and $B = 1$ elsewhere, where w is the width of the scattering edge (the etched step with finite width in the phase plate). The scattering (amplitude) mask is then applied to the input pulse as $E_{out}(x, \tau) = \mathcal{F}_\omega^{-1}\left[B(x, y)\mathcal{F}_\tau[E(x, \tau)] \exp\left(iA(x, y)\right)\right]$. Figure B1 shows the simulated shaper output without and with the scattering edge included in the simulation for a range of $\boldsymbol{\alpha}$ values.

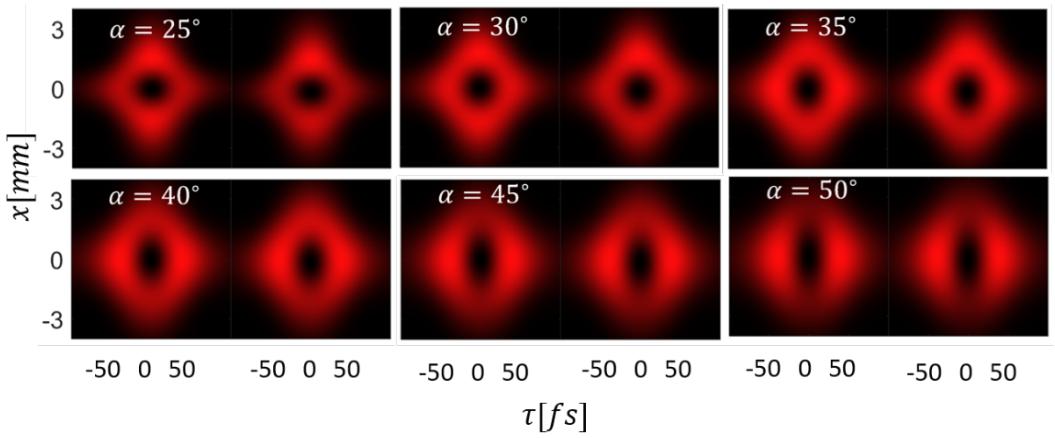

Figure B1. Intensity of the STOV at the pulse shaper output vs. π-step angle (α) with respect to dispersion direction (y). For each value of α, the left panel does not include scattering due to the π-step, while the right panel includes it by applying the phase mask B discussed above.

The pulse where the scattering edge is simulated show a slight dip in intensity at the bottom of the pulse due to amplitude modulation in the spatio-spectral domain.

The diamond-like shape of the simulated shaper output of Fig. B1 is a result of high order Hermite-Gaussian modes generated at each frequency bisected by the π-step of the phase plate. To illustrate this Fig. A2(a) shows the intensity output of the pulse shaper at $\alpha = 40°$ (without the scattering edge), while Fig. B2(c) shows

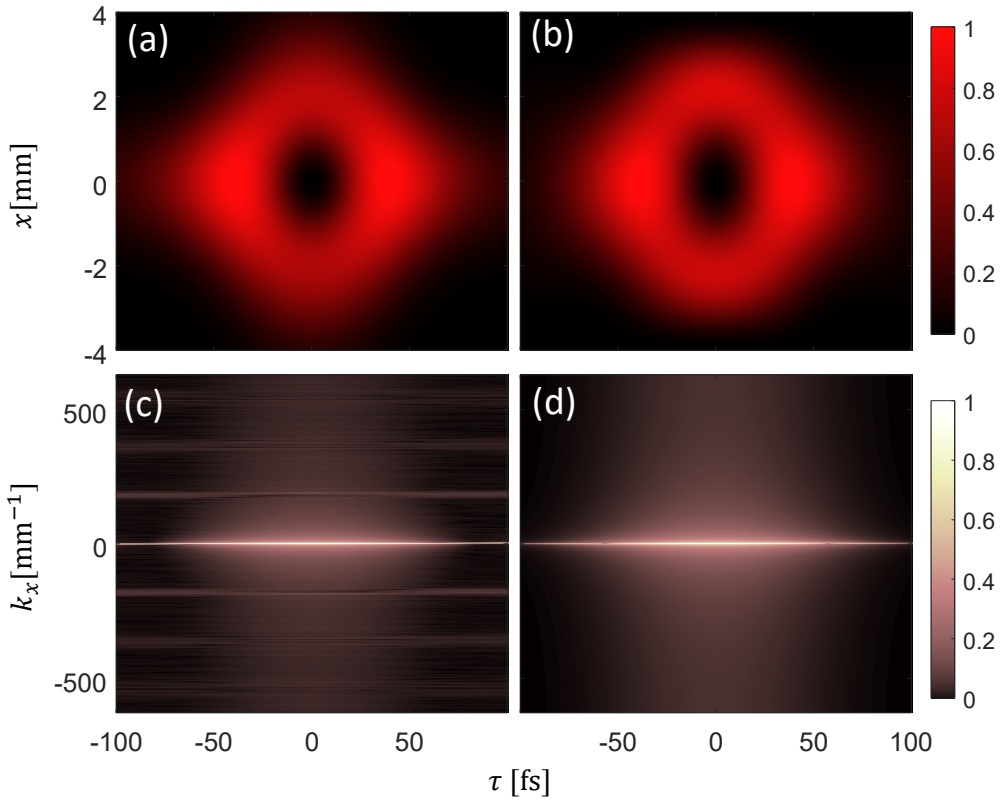

Figure B2. (a) Pulse shaper output for $\alpha = 40°$ without modeling scattering from edge of the π-step phase plate. (b) shows the spatially filtered output of the pulse shaper where large values of k_x in (c) are set to zero. (c) shows the log of the spatial Fourier transform of the shaper output, $\log(|\mathcal{F}_x(E_{out})| + 1)$. The high frequency horizontal stripes can be filtered out using a spatial filter which result in (b) the spatially filtered output of the pulse shaper (d) shows the log of the spatial Fourier transform of an ideal STOV, $\log(|\mathcal{F}_x(E_{STOV})| + 1)$.

log $(|\mathcal{F}_x(E_{out})| + 1)$. The high frequency components in the spectral domain of the field can be seen as horizontal strips. Figure A2(b), shows the result of spatially filtering the output of the pulse shaper (the spatial filtering here was performed by setting $k_x > 2.36mm^{-1} = 0$ in (c)). Finally, Fig. B2(d) shows log $(|\mathcal{F}_x(E_{out})| + 1)$ for an ideal symmetric STOV of the form $\propto (\tau/\tau_s \pm i\, x/x_s)E_0(\mathbf{r}_\perp, z, \tau)$. We note the absence of the horizontal bands in the spectrum.

Free space propagation of STOVs was previously explored experimentally and with simulations [27]. Figure B3 shows the simulated intensity and phase evolution during

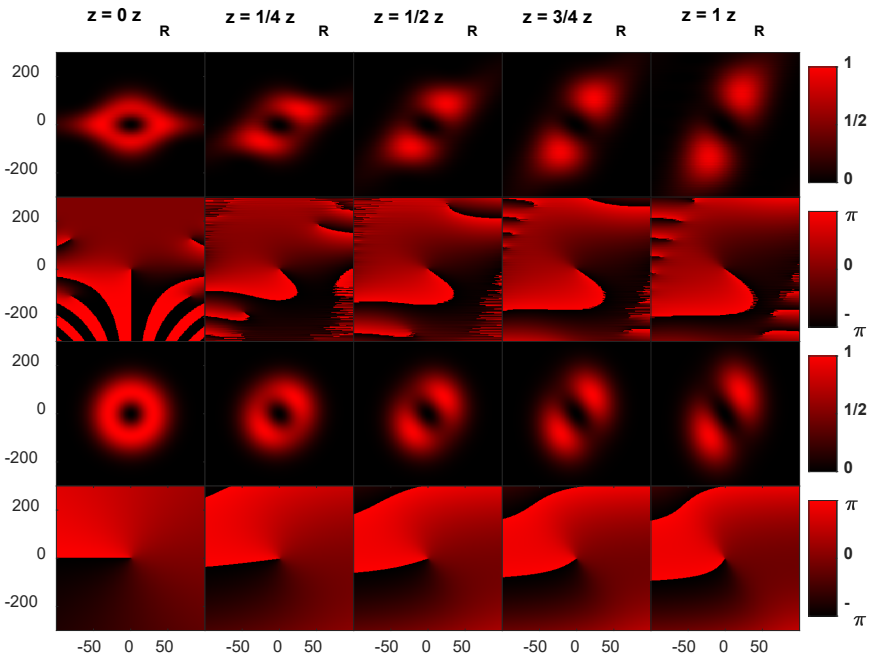

Figure B3. (Shaper) shows the intensity (top) and phase (bottom) of the shaper generated STOV pulse as it propagates over one Rayleigh length, z_R, of the Gaussian carrier pulse. (Ideal) shows the intensity (top) and phase (bottom) of an ideal STOV pulse as it propagates over one Rayleigh length, z_R, of the Gaussian carrier pulse.

propagation of the pulse shaper output and an ideal STOV over a Rayleigh range of the Gaussian input pulse, using the previously described UPPE method [83]. Note that both ideal- and shaper-generated STOVs evolve into two-lobed structures after one Rayleigh length of propagation.

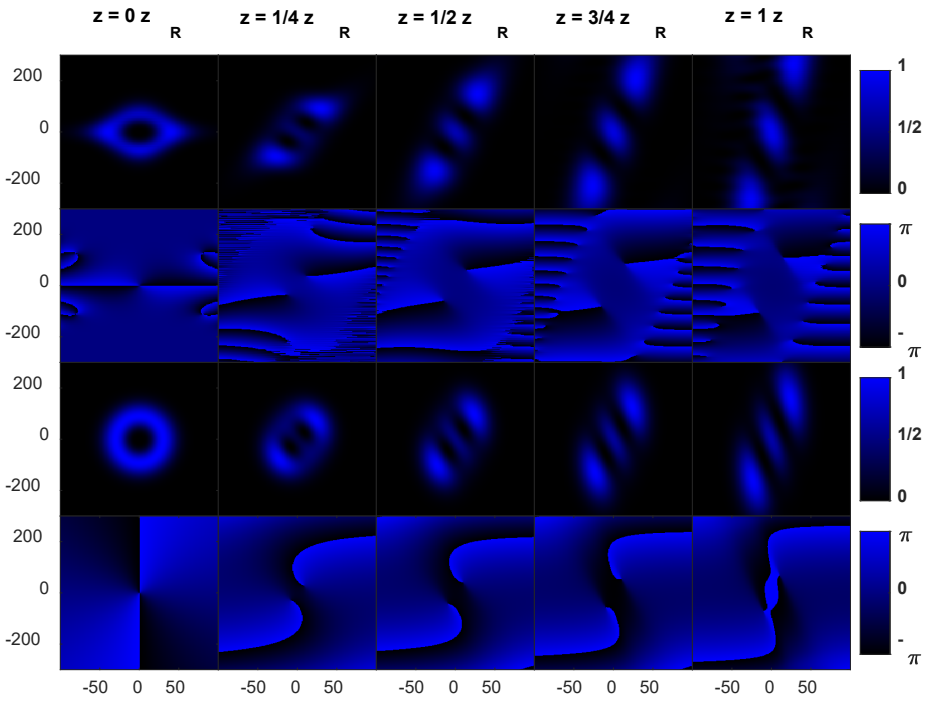

Figure B4. (Shaper) shows the intensity (top) and phase (bottom) of the second harmonic of the shaper-generated STOV pulse as it propagates over one Rayleigh length, z_R, of the second harmonic of the Gaussian input pulse. (Ideal) shows the intensity (top) and phase (bottom) of the second harmonic of an ideal STOV pulse as it propagates over one Rayleigh length, z_R, of the second harmonic of the Gaussian input pulse.

In Figure B4, we show propagation simulations of the intensity and phase evolution of the squared output of the pulse shaper (second harmonic generation in an ideal

crystal), and of an ideal STOV over the Rayleigh range of the frequency doubled Gaussian input pulse. Note that the second harmonic of both the ideal STOV and the shaper-generated STOV evolve into three-lobed structures after propagation of one Rayleigh length.

B.3 Experimental Setup Details

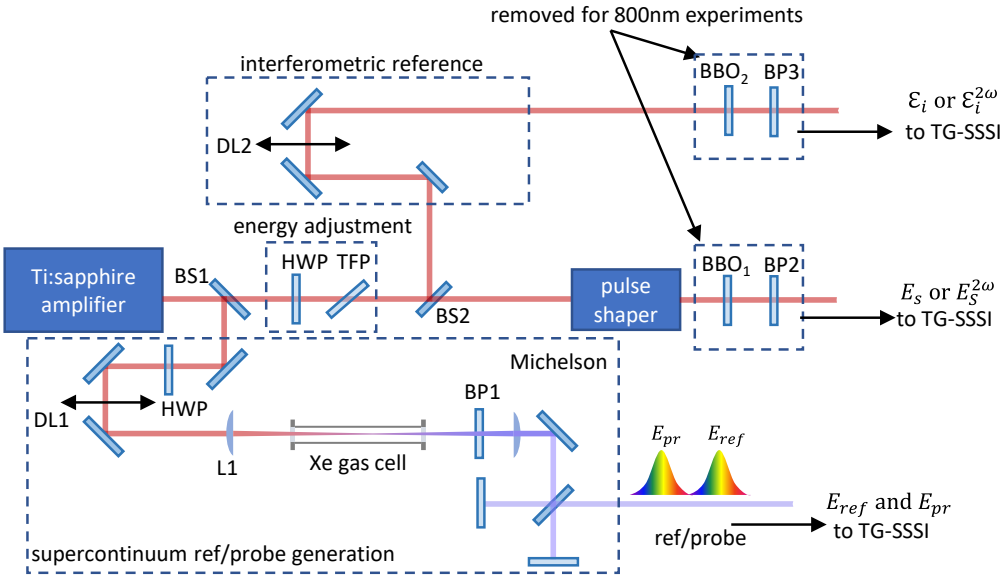

Figure B5. Preparation of pulses required for TG-SSSI measurement. The output from a Ti:Sapphire amplifier was split between reference and probe supercontinuum (SC) pulse generation (E_{ref} and E_{pr}), the structured pulse E_s, and the interferometric reference, $\mathcal{E}_i$, using beamsplitters BS1 (reflect 20%, transmit 80%) and BS2 (reflect 25%, transmit 75%). The energies of E_s and $\mathcal{E}_i$ were controlled using a half-wave plate (HWP) and thin film polarizer (TFP). The SC and $\mathcal{E}_i$ delay lines (DL1 and DL2) allow for control of the temporal overlap of the E_{pr} and $\mathcal{E}_i$ with E_s. For SHG measurements, the output of the pulse shaper, E_S, is passed through BBO_1 (100μm) to generate $E_S^{2\omega}$, which is then passed to the TG-SSSI setup using multiple 400nm dielectric mirrors (which filters out the 800nm light and is shown here as effective BP2). For SHG measurements, $\mathcal{E}_i$ is passed through BBO_2 (1mm) to generate $\mathcal{E}_i^{2\omega}$, which is then sent through 10nm bandpass filter BP3 centered at 400nm, which also rejects the fundamental. The interferometric reference $\mathcal{E}_i^{2\omega}$ is then directed to the TG-SSSI setup. In the SC delay line DL1, the beam is attenuated and apertured using an iris, and the linear polarization is rotated with half-waveplate HWP to be co-polarized with either E_s and $\mathcal{E}_i$ (for measurements of the fundamental), or $\mathcal{E}_i^{2\omega}$ and $E_S^{2\omega}$ (for SHG measurements). The output of DL1 is focused into the Xe gas cell using 75cm plano-convex lens L1. Filamentation in the 2 atm Xe gas cell generates broadband SC supercontinuum ~400-900 nm, which was short-passed below ~750 nm by BP1 (800 nm dielectric mirror), collimated using 40cm achromatic lens L2, and sent into a Michelson interferometer to generate E_{ref} and E_{pr}. The bandwidth 400-700 nm was used in TG-SSSI.

The experimental layout preceding TG-SSSI is shown in Fig. B5, with full description in the figure caption.

B.4 Modeling of Group Velocity Mismatch Effect

Modeling group velocity mismatch in nonlinear interactions using convolution integrals is a common heuristic approach [120]. Below we show the simple case of numerically adding the fields of two temporally offset $l = 2$ STOVs and find that this yields a pulse with two spatially offset $l = 1$ STOVs. At each infinitesimal slice of propagation of the fundamental through the BBO, a portion of the fundamental is converted to frequency doubled (second harmonic) light. The fundamental propagates faster through the BBO than the second harmonic, so at each infinitesimal slice of propagation, the locally generated second harmonic temporally leads the second harmonic generated at earlier infinitesimal slices. Mathematically, this is equivalent to convolving a single infinitesimal slice of generated second harmonic with a step function of width equal to the total walk-off of the second harmonic with respect to the fundamental. A toy model of this where the electric fields of two ideal $l = 2$ STOVs separated by 19 fs are added together is shown in Fig. B6.

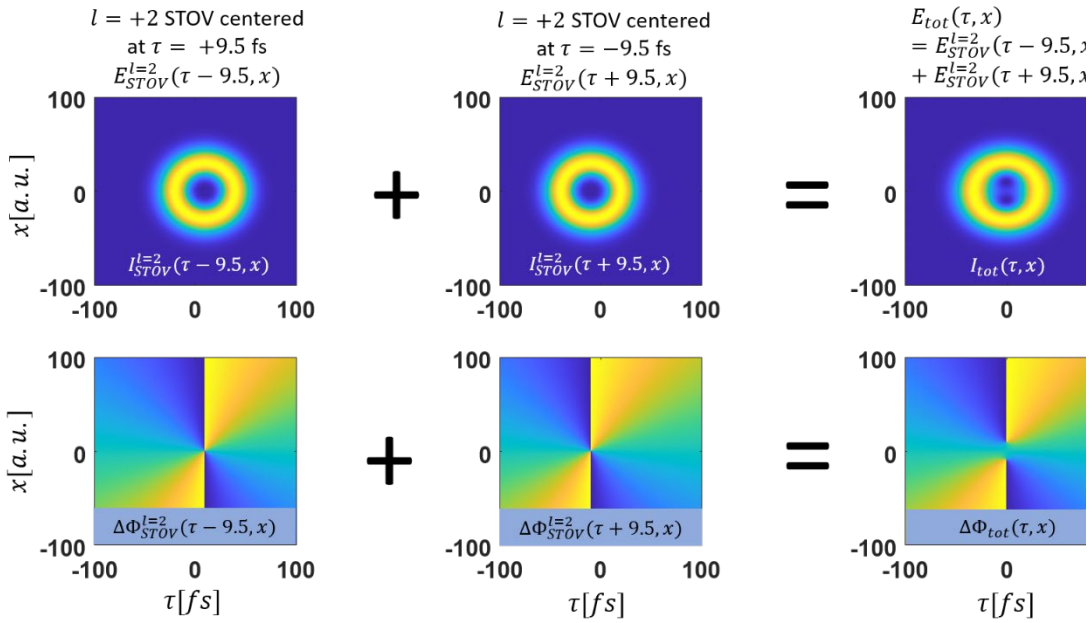

Figure B6. Shows a toy model of the result when the electric field of two temporally offset $l = 2$ STOVs are added, resulting in two $l = 1$ STOVs offset spatially.

Chapter 6: Transient Perturbations of Light and Transverse OAM

6.1 Introduction

Since the publication of the accomplishments in the previous chapters, alternative methods for STOV generation have been proposed [121–123], and calculation of higher order STOV propagation has been performed [124]. Despite the rapidly increasing experimental activity studying STOVs, there had been no theoretical analysis of their OAM content until recently [30,87,125], where one result determined that STOV-based OAM must take half-integer values [30] (See Chapter 3), with the other claiming that only integer values are allowed [87,125] (see further discussion in Sec. 6.6). This difference is more than just an academic question, as it quantifies the exchange of transverse OAM in light-matter interactions. Such interactions, the subject of this chapter, are one of the building blocks of future applications of STOVs.

Interactions of longitudinal OAM-carrying beams with matter have been long studied. One early example is the interaction of a LG_{0m} donut mode with a macroscopic particle, causing it to rotate about the OAM axis [5]. The converse of this process can be viewed as the torquing of light, in which a light beam gains OAM from an interaction with matter. A simple example of this is the pickup of OAM by a beam passing through a spiral phase plate [19] or any refractive index structure that imparts a non-zero azimuthal phase shift about the propagation axis. For example, LG_{0m} donut beam

propagation through a turbulent atmosphere leads to an output beam carrying a spectrum of longitudinal OAM states $m, m \pm 1, m \pm 2, \ldots$. [13,126], owing to the random azimuthal phase shifts picked up over the propagation range. In all of these cases, the OAM beam can be CW and monochromatic, with the refractive index structures static on the timescale of the beam evolution: such torquing of light makes preservation of pure longitudinal OAM states difficult.

In this chapter, we present the first experimental evidence of the controlled spatiotemporal transfer of *transverse* OAM to light by matter: the *spatiotemporal* torquing of light. This is a radically different situation than the torquing of longitudinal, spatially-defined OAM light by stationary or slowly varying refractive index structures such as phase plates or air turbulence. We demonstrate that transverse OAM of a light pulse can be changed only for sufficiently fast transient phase perturbations that overlap with the pulse in spacetime, or by removing energy from a pulse already possessing transverse OAM. We explore the physics of what constitutes an optimal overlap. Furthermore, we experimentally verify our "half-integer" theory of STOV OAM [30]; the theory is crucial to correctly quantifying the light-matter interaction of this experiment. We also make a connection to the first measurement of STOVs [24], providing a spatiotemporal torque-based explanation for their generation.

6.2 Determining Changes in Transverse Orbital Angular Momentum

The perturbation-induced change in the orbital angular momentum of an optical pulse can be determined from measurements of the amplitude and phase of the pulse before

and after the perturbation. For the well-known case of pulses with longitudinal OAM, say along $\hat{\mathbf{z}}$, the procedure is straightforward: If the pre- and post-perturbation complex electromagnetic field envelopes are E_s and E_{sp}, then the change in longitudinal OAM per photon (which is necessarily *intrinsic* OAM) is computed as $\Delta\langle L_z\rangle = \langle L_z\rangle_{sp} - \langle L_z\rangle_s = u_{sp}^{-1}\langle E_{sp}|L_z|E_{sp}\rangle - u_s^{-1}\langle E_s|L_z|E_s\rangle$, where $L_z = (\mathbf{r}\times\hat{\mathbf{p}})_z = -i(x\,\partial/\partial y - y\,\partial/\partial x)$ is the longitudinal OAM operator. Here we use the linear momentum operator $\hat{\mathbf{p}} = -i\nabla$, and $u_{s,sp} = \langle E_{s,sp}|E_{s,sp}\rangle = \int d^3\mathbf{r}\,|E_{s,sp}|^2$. The expectation values of L_z for the pre- and post-perturbation fields are $\langle L_z\rangle_{s,sp} = u_{s,sp}^{-1}\langle E_{s,sp}|L_z|E_{s,sp}\rangle = u_{s,sp}^{-1}\int d^3\mathbf{r}\,E_{s,sp}^* L_z E_{s,sp}$, where the integrals are taken over all space, with $d^3\mathbf{r} = dxdydz$ and the origin taken as the energy density centroid (or "centre of energy"). This choice of origin isolates the intrinsic OAM from extrinsic OAM; it is further discussed in Sec. 6.6. The same result is obtained by directly integrating the OAM density of the fields [127]: $\Delta\langle L_z\rangle = 2k_0U_{sp}^{-1}\int d^3\mathbf{r}\,[(\mathbf{r}-\mathbf{r}_{sp})\times(\mathbf{E}_{sp}\times\mathbf{H}_{sp}^*)]_z - 2k_0U_s^{-1}\int d^3\mathbf{r}\,[(\mathbf{r}-\mathbf{r}_s)\times(\mathbf{E}_s\times\mathbf{H}_s^*)]_z$, where $U_{s,sp} = \int d^3\mathbf{r}\,(|\mathbf{E}_{s,sp}|^2 + |\mathbf{H}_{s,sp}|^2)$, $\mathbf{r}_{s,sp} = U_{s,sp}^{-1}\int d^3\mathbf{r}\,\mathbf{r}(|\mathbf{E}_{s,sp}|^2 + |\mathbf{H}_{s,sp}|^2)$ are the respective pulse centres of energy, $\mathbf{H}_{s,sp}$ is the magnetic field, and k_0 is the wavenumber of the fields, which can be monochromatic. Here we have assumed a dilute non-magnetic material with index of refraction satisfying $Re(n) \cong 1$.

Likewise, for changes in transverse spatiotemporal OAM, an operator-based calculation should agree with a direct field-based calculation using the transverse OAM density. That is, if E_s and E_{sp} are pre- and post-perturbation $\hat{\mathbf{y}}$-polarized pulses

propagating along $\hat{\mathbf{z}}$ with transverse OAM oriented along $\hat{\mathbf{y}}$ (ensuring no effects of spin angular momentum), the change in intrinsic transverse OAM per photon, $\Delta\langle L_y\rangle$, should be calculable either as

$$\Delta\langle L_y\rangle = \langle L_y\rangle_{sp} - \langle L_y\rangle_s = u_{sp}^{-1}\langle E_{sp}|L_y|E_{sp}\rangle - u_s^{-1}\langle E_s|L_y|E_s\rangle, \tag{6.1a}$$

$$\begin{aligned}\text{or}\quad \Delta\langle L_y\rangle = {} & 2k_0' U_{sp}^{-1}\int d^3\mathbf{r}'\left[\left(\mathbf{r}'-\mathbf{r}_{sp}'\right)\times\left(\mathbf{E}_{sp}\times\mathbf{H}_{sp}^*\right)\right]_y - \\ & 2k_0 U_s^{-1}\int d^3\mathbf{r}'\left[\left(\mathbf{r}'-\mathbf{r}_s'\right)\times\left(\mathbf{E}_s\times\mathbf{H}_s^*\right)\right]_y ,\end{aligned} \tag{6.1b}$$

provided that the correct L_y operator is used in Eq. (6.1a) and the origin is the spacetime centre of energy. In Eq. (6.1b), $\mathbf{r}'$ refers to spacetime coordinates in the group velocity frame of the pulse (see below), $u_{s,sp} = \int d^3\mathbf{r}'\,|\mathbf{E}_{s,sp}|^2$, $U_{s,sp} = \int d^3\mathbf{r}'\,(|\mathbf{E}_{s,sp}|^2 + |\mathbf{H}_{s,sp}|^2)$, and $\mathbf{r}_{s,sp}' = U_{s,sp}^{-1}\int d^3\mathbf{r}'\,\mathbf{r}'(|\mathbf{E}_{s,sp}|^2 + |\mathbf{H}_{s,sp}|^2)$ are the spacetime centres of energy. Because STOV pulses are polychromatic [30], here k_0 is the central wavenumber and k_0' allows for a central wavenumber shift in a spatiotemporally perturbed pulse. For weak perturbations, $k_0' = k_0$, and for negligibly absorbing perturbations (see Sec. III), $u_{sp} = u_s$ and $U_{sp} = U_s$. Our experiments satisfy these conditions. These expressions also assume nonmagnetic material and $Re(n) \cong 1$, the conditions of our experiments.

As indicated, care must be taken in determining the form of the spatiotemporal OAM operator L_y. Unlike longitudinal OAM L_z, whose physical origin is the circulation of electromagnetic energy density around the z-axis in both x and y

dimensions, energy density flow in a $\hat{\mathbf{z}}$-propagating STOV pulse in vacuum, with OAM along $\hat{\mathbf{y}}$, can occur only along $\pm x$: if any flow occurred along z, it would be superluminal or subluminal above or below the vortex singularity (depending on the sign of the STOV), violating special relativity. In recent work [30], we found a transverse spatiotemporal OAM operator, expressed in spacetime rectangular or polar coordinates,

$$\begin{aligned} L_y = (\mathbf{r}' \times \hat{\mathbf{p}}_{st})_y &= -i\left(\xi \frac{\partial}{\partial x} + \beta_2 x \frac{\partial}{\partial \xi}\right) \\ &= -i\left[\rho \sin\Phi \cos\Phi\,(1+\beta_2)\frac{\partial}{\partial \rho}\right. \\ &\left. + (\cos^2\Phi - \beta_2 \sin^2\Phi)\frac{\partial}{\partial \Phi}\right] \\ &\rightarrow -i(\cos^2\Phi - \beta_2 \sin^2\Phi)\frac{\partial}{\partial \Phi}\ , \end{aligned} \tag{6.2}$$

which applies in a dispersive optical material. Here $\xi = v_g t - z$ is a local space coordinate in the group velocity (v_g) frame of the pulse (local time is $\tau = \xi / v_g$), t is time in the lab frame, $\beta_2 = v_g^2 k_0 k_0''$ is the dimensionless group velocity dispersion of the material, $k_0'' = (\partial v_g^{-1}/\partial \omega)_{k_0}$, and $\hat{\mathbf{p}}_{st} = -i\nabla_{st} = -i(\nabla_\perp - \beta_2\, \partial/\partial \xi)$ is the spatiotemporal linear momentum operator [30]. The spacetime polar coordinates (ρ, Φ) are defined by $x = \rho \sin\Phi$ and $\xi = \rho\cos\Phi$. The arrow in Eq. (6.2) indicates that the first term in the full polar coordinate expression always integrates to zero in Eq. 1(a), leaving the second term as the intrinsic transverse OAM operator in polar coordinates [30]. In performing the integrals in Eqs. (6.1a) and (6.1b), $d^3\mathbf{r}' = dydxd\xi$

in spacetime rectangular coordinates and $d^3\mathbf{r}' = dy\rho d\rho d\Phi$ in spacetime polar coordinates.

Our L_y operator is consistent with special relativity, it conserves electromagnetic energy density flux, and it is conserved with propagation: $d/dz\ \langle L_y \rangle = i(2k_0)^{-1}\langle [H, L_y] \rangle = 0$ [30]. Here $\left[H, L_y\right]$ $(= 0)$ is the commutator of L_y and the propagation operator, $H = -\nabla_\perp^2 + \beta_2\, \partial^2/\partial\xi^2$, from the spacetime paraxial wave equation $2ik_0\, \partial \mathbf{A}(\mathbf{r}_\perp, \xi; z)/\partial\, z = H\mathbf{A}(\mathbf{r}_\perp, \xi; z)$ for the field $\mathbf{A}$. In the group velocity frame, z plays the role of a time-like running parameter. It is straightforward to show that L_y is conserved under non-paraxial propagation as well (see Sec. 6.6).

For the room air of our experiments, $\beta_2 \cong 1.5 \times 10^{-5}$. This small dispersion has a negligible effect over short air propagation distances, so for the analysis below we take $\beta_2 = 0$ and the transverse OAM operator becomes $L_y = -i\xi\, \partial/\partial x \rightarrow -i \cos^2 \Phi\, \partial/\partial\Phi$ from Eq. (6.2). Note that without the gradient in ξ enabled by nonzero β_2, this operator cannot transport energy density along $\pm\xi$ in the group velocity frame; it is transported only along $\pm x$.

To illustrate how STOVs propagate and to provide definitions for parameters used later in this chapter, Fig. 6.1(a) reproduces results from [30], where a STOV pulse, of topological charge $l = 1$ and spacetime asymmetry ratio $\alpha = w_{0\xi}/w_{0x} = 0.24$, propagates right to left in air from $z/z_{0x} = -0.41$ to $z/z_{0x} = 0.24$, and right to left within each panel. Here $w_{0\xi}$ and w_{0x} are time-like and space-like Gaussian spatial scales of the pulse, and $z_{0x} = k_0 w_{0x}^2/2$ is the space-like Rayleigh range. The top two

rows are spatiotemporal intensity and phase profiles from the analytic modal STOV theory of [30], and the bottom rows are the corresponding experimental intensity and phase profiles $|E_s(x,\xi)|^2$ and $\phi_s(x,\xi) = \arg(E_s(x,\xi))$ captured by TG-SSSI [28], where the Gaussian y-dependence of the field is not displayed as it remains unaffected in our experiments and computations. Spatial diffraction along $\pm x$ causes the donut shape near $z = 0$ to evolve to lobed structures with opposite spacetime tilt on either side of $z = 0$, while the transverse OAM is conserved throughout propagation. For a STOV pulse of topological charge l and spacetime asymmetry ratio α propagating in a dispersive medium characterized by β_2, the expectation value of transverse OAM is $\langle L_y \rangle = \frac{1}{2} l(\alpha - \beta_2/\alpha)$, so that for the air-propagating STOV pulse in Fig. 6.1, $\langle L_y \rangle = \frac{1}{2} l\alpha = 0.12$. The factor of ½ for the spacetime vortex is a direct result of energy density circulation restricted to $\pm x$ [30].

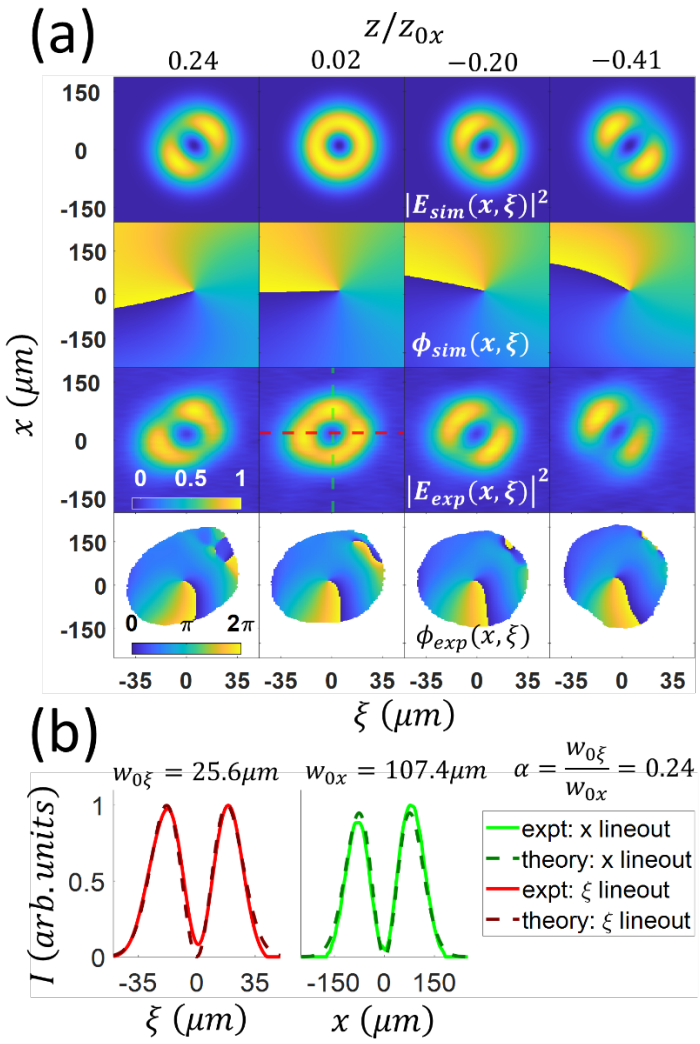

Figure 6.1. Illustrative figure on STOV pulse propagation for spacetime asymmetry ratio $\alpha = w_{0\xi}/w_{0x} = 0.24$, with $z_{0x} = \frac{1}{2}k_0 w_{0x}^2 = 4.5$ cm (a) Top 2 rows: Modal theory [30] plots of spatiotemporal intensity and phase of $l = 1$ STOV pulse propagating right to left through its beam waist from $z/z_{0x} = -0.41$ to $z/z_{0x} = 0.24$ (and right to left within each panel). Bottom 2 rows: experimental intensity and phase plots extracted by TG-SSSI. (b) Lineouts along $(0, \xi)$ and $(x, 0)$ of the experimental intensity profile at $z/z_{0x} = 0.02$ (solid lines) and fits to the modal theory curves (dashed lines).

6.3 Spatiotemporal Torque

The goal of our experiments is twofold: (1) to explore how spatiotemporal perturbations to electromagnetic fields affect transverse OAM, and (2) to verify the correctness of our theoretical approach [30]. For an initial pulse $A_s(x,\xi) = |A_s(x,\xi)|e^{i\phi_s(x,\xi)}$ and a spatiotemporal perturbation $\Gamma(x,\xi) = |\Gamma(x,\xi)|e^{i\Delta\phi_p(x,\xi)}$, where $\phi_s(x,\xi)$ and $\Delta\phi_p(x,\xi)$ are real functions, the perturbed pulse is $A_{sp}(x,\xi) = \Gamma(x,\xi)A_s(x,\xi)$. This formulation implicitly assumes that the perturbation does not backscatter light back into the pulse; this condition is well satisfied by sufficiently weak perturbations, including those of our experiments, and by perturbations that effectively remove energy from the pulse. We take A_s and A_{sp} to be polarized along $\hat{\mathbf{y}}$ so there are no effects of spin angular momentum. The change of transverse OAM per photon from the perturbation is then (see Sec. 6.6)

$$\begin{aligned}\Delta\langle L_y\rangle &= \langle L_y\rangle_{sp} - \langle L_y\rangle_s \\ &= iu_{sp}^{-1}\int dx\, d\xi \left[|A_s|^2|\Gamma|^2 L_y\Delta\phi_p \right. \\ &\left. + |A_s|^2\left(|\Gamma|^2 - \frac{u_{sp}}{u_s}\right)L_y\phi_s\right],\end{aligned} \tag{6.3}$$

where $u_{sp} = \int dx\, d\xi\, |A_s(x,\xi)|^2|\Gamma(x,\xi)|^2$.

Equation (6.3) is intuitively appealing. The first term suggests the notion of "spatiotemporal torque", where the change in OAM is given by an effective force-lever

arm product, $iL_y\Delta\phi_p = \xi\,\partial\Delta\phi_p/\partial x + \beta_2 x\,\partial\Delta\phi_p/\partial\xi$, weighted by the energy density distribution $|A_{sp}(x,\xi)|^2 = |\Gamma(x,\xi)A_s(x,\xi)|^2$ of the torqued object. Here the "force" components are $\partial\Delta\phi_p/\partial x$ and $\beta_2\,\partial\Delta\phi_p/\partial\xi$, and the lever arm components are ξ and x. A mechanical analogy for the second term is the change in OAM caused by location-specific mass removal from a spinning wheel. For cases where energy is removed from the pulse by absorption or backscattering, $u_{sp}/u_s < 1$, and the second term contributes to the change in OAM provided that the initial pulse has transverse OAM; otherwise $L_y\phi_s = 0$ and the second term vanishes. That is, the wheel must already be spinning for mass removal to change OAM. Note that the second term will vanish, irrespective of ϕ_s, in the case of a pure phase perturbation where $|\Gamma| = 1$ and $u_{sp}/u_s = 1$. This type of perturbation corresponds to our experiments.

Further examination of Eq. (6.3) leads to several insights: (a) Pure amplitude perturbations (with $\Delta\phi_p$ =constant) that conserve pulse energy cannot change the transverse OAM of a light pulse; in that case $\Gamma(x,\xi)$ can be viewed as a scattering coefficient that redistributes pulse energy over $\pm x$ in the pulse frame. (b) Steady state ($\partial\Delta\phi_p/\partial\xi = 0$) or spatially uniform ($\partial\Delta\phi_p/\partial x = 0$) phase perturbations do not change transverse OAM. (c) The only ways to change transverse OAM are (i) if either or both of the effective force terms, $\partial\Delta\phi_p(x,\xi)/\partial x$ and $\beta_2\,\partial\Delta\phi_p(x,\xi)/\partial\xi$, are time-varying and have an asymmetric temporal overlap with the energy density distribution (across the pulse's temporal centre of energy) or (ii) energy is removed from a pulse already containing transverse OAM. In atmospheric density gases, β_2 is negligible and

$\partial\Delta\phi_p(x,\xi)/\partial x$ is the dominant contribution to the first term of Eq. (6.3), providing an unbalanced x-component force across $\xi = 0$.

We now consider a simple step function perturbation model, which provides good physical intuition and corresponds to our experiments (see Sec. 6.4). It also provides interpretative insight for the first experiment to measure STOVs [24]. We apply the spacetime perturbation $\Gamma(x,\xi) = |\Gamma(x,\xi)|e^{i\Delta\phi_p(x,\xi)}$, with $|\Gamma(x,\xi)| = 1$ and

$$\Delta\phi_p(x,\xi) = \Delta\phi_{p0}[\Theta(x - x_0 + h) - \Theta(x - x_0 - h)]\Theta(\xi - \xi_0)\,, \tag{6.4}$$

to either a Gaussian pulse, $A_{\mathrm{G}}(x,\xi)$, or to a $l = 1$ STOV pulse, $A_{\mathrm{STOV}}(x,\xi)$:

$$A_{\mathrm{G}}(x,\xi) = \mathrm{A}_0\exp\left(-x^2/w_{0x}^2 - \xi^2/w_{0\xi}^2\right) \tag{6.5a}$$

$$A_{\mathrm{STOV}}(x,\xi) = \left(\xi/w_{0\xi} + i\,x/w_{0x}\right)A_{\mathrm{G}}(x,\xi) \tag{6.5b}$$

Here $\Theta(q)$ is the Heaviside function, $2h$ is the spatial width of the perturbation centered at $x = x_0$, and the perturbation turns on at $\xi = \xi_0$ (or $\tau = \tau_0$). The choice of a phase-only perturbation ($|\Gamma(x,\xi)| = 1$) corresponds to our experimental perturbation (see Sec. 6.4). The space-like and time-like widths of the Gaussian pulse are w_{0x} and $w_{0\xi}$, and the expressions for $\mathrm{A_G}$ and for $\mathrm{A_{STOV}}$ are accurate for $z << z_{0x} = k_0 w_{ox}^2/2$ [30]. Because transverse OAM is conserved with z, it is sufficient to use these expressions in our calculations. Using Eq. (6.1a) with initial fields A_{G} or A_{STOV}, the simple

perturbation model produces analytic solutions for $\Delta\langle L_y\rangle_{\mathrm{G}}$ and $\Delta\langle L_y\rangle_{\mathrm{STOV}}$ as a function of (x_0, ξ_0):

$$\Delta\langle L_y\rangle_G = \frac{\Delta\phi_{p0}}{2\pi}\left(\alpha + \frac{\beta_2}{\alpha}\right)\left(\exp\left(\frac{8hx_0}{w_{0x}^2}\right) - 1\right)\exp\left(-\frac{2(h+x_0)^2}{w_{0x}^2} - \frac{2\xi_0^2}{w_{0\xi}^2}\right) \quad (6.6a)$$

$$\begin{aligned}\Delta\langle L_y\rangle_{STOV} = \frac{\Delta\phi_{p0}}{2\pi}\left(\alpha + \frac{\beta_2}{\alpha}\right)\exp\left(-\frac{2(h+x_0)^2}{w_{0x}^2} - \frac{2\xi_0^2}{w_{0\xi}^2}\right) \\ \times\left[\left(\exp\left(\frac{8hx_0}{w_{0x}^2}\right) - 1\right)\left(1 + 2\frac{h^2 + x_0^2}{w_{0x}^2} + 2\frac{\xi_0^2}{w_{0\xi}^2}\right)\right. \\ \left. - \frac{4hx_0}{w_{0x}^2}\left(\exp\left(\frac{8hx_0}{w_{0x}^2}\right) + 1\right)\right].\end{aligned} \quad (6.6b)$$

Figures 6.2(a) and 6.2(b) plot $\Delta\langle L_y\rangle_{\mathrm{G}}$ and $\Delta\langle L_y\rangle_{\mathrm{STOV}}$ vs. (x_0, ξ_0). Each panel is for a particular half-width h/w_{ox} and normalized dispersion β_2, where $\beta_2 = \pm 1$ is for dense, positively or negatively dispersive media and $\beta_2 = 0$ corresponds to low density media such as air, the propagation medium of our experiment. Plots using the dispersion of air, $\beta_2 \cong 1.5 \times 10^{-5}$, are indistinguishable from those using $\beta_2 = 0$.

We first discuss the $\beta_2 = 0$ plots (the plots for $\beta_2 = 1$ cases are qualitatively similar). Figure 6.2(a) shows the transfer of transverse OAM to A_G, a pulse with zero initial OAM. Maximum OAM transfer occurs for x_0 located at the spatial edges of the pulse ($x_0 \sim \pm w_{0x}$) and for ξ_0 located near the pulse centre ($\xi_0 \sim 0$). As discussed earlier in the context of Eq. (6.3), these optimum zones of (x_0, ξ_0) maximize the overlap of the force-lever arm product with the torqued pulse energy density. Importantly, the perturbation transient (here, the step $\Theta(\xi - \xi_0)$) must overlap with the pulse so that the

torque contributions are imbalanced across the temporal centre of energy at $\xi = 0$. For $\Theta(\xi - \xi_0)$ located outside the region of the pulse (for $\left|\xi_0/w_{0\xi}\right| > \sim 1$), $\Delta\langle L_y \rangle \to 0$ because the pulse sees the perturbation as steady state. The effect on $\Delta\langle L_y \rangle$ of a spatiotemporal torque localized in space and time is described in Sec. 6.6, supporting the analogy of mechanical torque on a wheel.

The effect of the perturbation on an $l = 1$ STOV pulse is plotted in Fig. 6.2(b). Based on our prior discussion, it is not surprising that the plots are qualitatively similar to those for $l = 0$ in Fig. 6.2(a), with similar values of maximum OAM transfer $|\Delta\langle L_y \rangle|_{max}$. For a phase perturbation with $|\Gamma(x, \xi)| = 1$, Eq. (6.3) shows that $\Delta\langle L_y \rangle$ does not depend on $\phi_s(x, \xi)$, the phase winding of the initial pulse. Detailed differences between Figs. 6.2(a) and 6.2(b) arise from the different energy density distributions $|A_s(x, \xi)|^2$ for Gaussian and STOV pulses.

For $\beta_2 = -1$, $\Delta\langle L_y \rangle = 0$ in all cases. In such a negatively dispersive material, the spatiotemporal pulse shape is preserved because the dispersion in time matches the amplitude and sign of diffraction in space. The effect of any spatiotemporal torque applied to the pulse is zero, because the effective forces applied at the end of the lever arm are balanced.

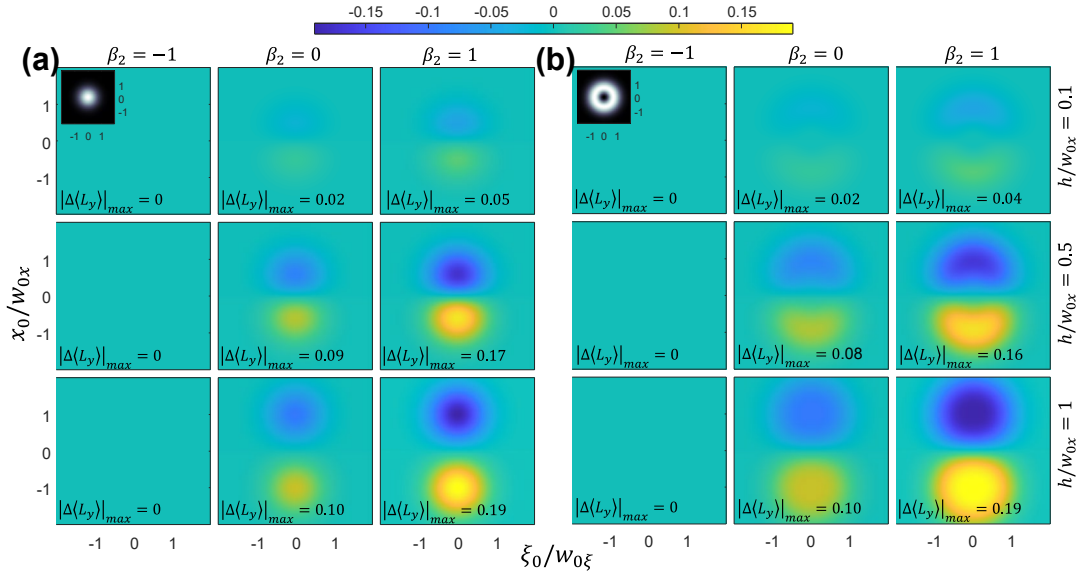

Figure 6.2. Plots of analytic solutions (Eqs. 6.6(a) and 6.6(b)) of $\Delta\langle L_y\rangle$ vs. (x_0, ξ_0) for the spatiotemporal phase shift $\Delta\phi_p(x,\xi)$ of Eq. (6.4) applied to (a) a Gaussian pulse $A_G(x,\xi)$ (Eq. 6.5(a)) and to (b) an $l = 1$ STOV pulse $A_{STOV}(x,\xi)$ (Eq. (6.5b)); x_0 and ξ_0 are the central space location and turn-on time of the perturbation. In Eq. (6.4), we choose $\Delta\phi_{p0} = -0.5$ to model the plasma generated by optical field ionization (OFI) of air.

It is important here to relate these results to the first experimental measurement of STOVs, which were spontaneously generated as a consequence of arrested self-focusing collapse in femtosecond pulse filamentation in air [24]. In air, femtosecond filamentation [46,47] occurs when an ultrashort pulse undergoes self-focusing collapse, which continues and accelerates until the intensity is high enough to ionize air molecules via optical field ionization (OFI), with the ultrafast-risetime plasma then acting to defocus the pulse. The few-femtosecond risetime of the plasma, determined by the OFI rate, occurs well within the pulse temporal envelope. The generated plasma then has a recombination-limited lifetime of several nanoseconds, an extremely long

timescale compared to the pulse itself. The phase perturbation imparted by this plasma is therefore quite well modeled by Eq. (6.4) for $(x_0, \xi_0) = (0,0)$ and $h/w_{0x} \sim 0.5$, where the filament plasma is centered on the pulse and its width $2h$ is narrower than the beam width $\sim 2w_{0x}$.

While the filament-like case of $\beta_2 = 0$ and $h/w_{0x} = 0.5$ (middle right panel in Fig. 2(a)) shows that $\Delta\langle L_y \rangle = 0$ for $(x_0, \xi_0) = (0,0)$, the change in transverse OAM *density*, $\Delta M_y(x, \xi) = A_{sp}^* L_y A_{sp}$ (from Eq. (6.1a)), is non-zero, and this is the effect measured in the experiment of Ref. [24], albeit for a much larger $|\Delta\phi_{p0}|$ accumulated over self-focused propagation in ionizing air. The plots of ΔM_y vs. (x, ξ) in Fig. 6.3(a) and (b) show regions of OAM density of opposite sign across the $x = 0$ axis, displaying physics similar to an x-ξ planar slice of the toroidal STOVs first measured in [24]. Figure 6.3(a) plots ΔM_y for the simple step function perturbation of Eq. (6.4); non-zero ΔM_y regions are only 1 pixel wide. Figure 6.3(b) uses a more realistic perturbation with smoothed step transitions,

$$\Delta\phi_p(x, \xi) = \tfrac{1}{2}\Delta\phi_{p0}\left(1 + \mathrm{erf}\left(\sqrt{2}\,(\xi - \xi_0)/h_\xi\right)\right)\exp\left(-\left((x - x_0)/h_x\right)^8\right), \qquad (6.7)$$

where we take $(x_0, \xi_0) = (0,0)$, $h_x/w_{0x} = 0.5$, and $h_\xi/w_{0\xi} = 0.5$.

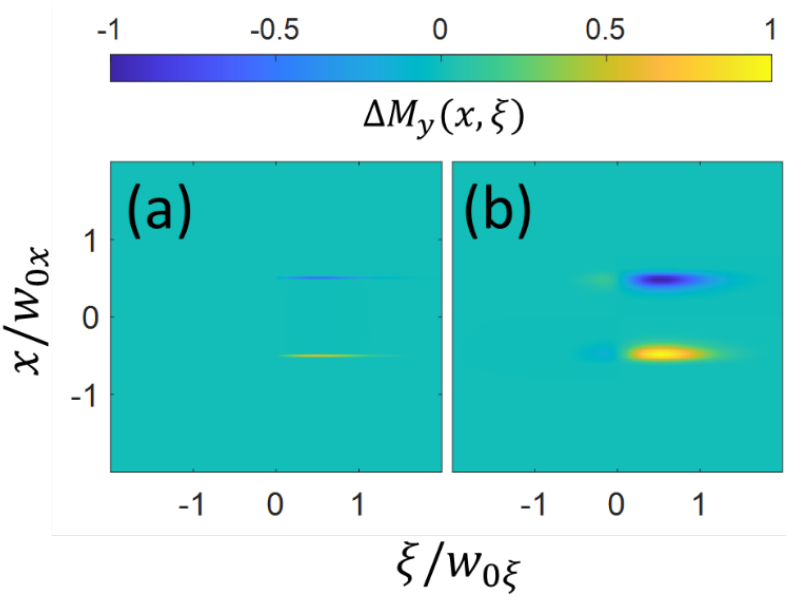

Figure 6.3. (a) Change in transverse angular momentum density $\Delta M_y(x,\xi) = A_{sp}^* L_y A_{sp}$ of a Gaussian pulse $\mathrm{A_G}(x,\xi)$ using step function perturbation, Eq. (6.4). (b) Same as (a) except using smoothed perturbation, Eq. (6.7). In both panels, $\Delta M_y(x,\xi)$ is normalized by the maximum value $|\Delta M_y(x,\xi)|_{max}$.

We now address the effect of a non-energy-conserving pure amplitude perturbation on pulses with and without initial transverse OAM. We place the perturbation $\Gamma(x,\xi) = 1 - \exp(-(x/h)^8)$ at the beam waist ($z = 0$) of $l = 1$ STOV and Gaussian pulses described by Eqs. (6.5a) and (6.5b), with $w_{0x} = w_{0\xi} = 100$ μm, and $2h = 100$ μm. This models a steady state obstruction in the pulse propagation path such as a solid wire of diameter $2h$ centered at $x = 0$, which would remove pulse energy by a combination of backscattering and absorption. Shown in Fig. 6.4(a) are the unperturbed spatiotemporal intensity profiles $I_s(x,\xi) = |E_s(x,\xi)|^2$ for the STOV and Gaussian pulses at $z = 0^-$, followed by the perturbed pulses $I_{sp}(x,\xi) = |E_{sp}(x, y = 0, \xi; z)|^2$

propagating from $z = 0$ to $z = 2z_{0x}$. These were computed by forward-propagating the electric and magnetic fields $\mathbf{E}_{sp}(x, y, \xi; z)$ and $\mathbf{H}_{sp}(x, y, \xi; z)$ from $z = 0$ using our unidirectional pulse propagation code YAPPE (See Sec. 6.6). The z-dependent change in transverse OAM $\Delta\langle L_y \rangle_z$ was calculated directly from the fields using Eq. (6.1b) and plotted in Fig. 6.4(b) as points every $0.1z_{0x}$. In both cases, as expected, $\Delta\langle L_y \rangle_z$ remains constant after the perturbation owing to the conservation of L_y. It is seen that only the STOV pulse has its transverse OAM per photon changed. This is predicted by Eq. (6.3): the second term contributes only if $L_y \phi_s \neq 0$ (the first term in Eq. (6.3) is zero because this is a pure amplitude perturbation). Note that even though the perturbation is on the beam axis at $x = 0$, $\Delta\langle L_y \rangle$ is still non-zero because energy is removed from the pulse at a specific location; this imposes a new spatiotemporal distribution of the remaining energy and thus a new transverse OAM per photon. Changing the x-position of the wire will change $\Delta\langle L_y \rangle$ through new spatiotemporal distributions of the remaining energy. The constant solid line overlaid on the points is determined by a calculation of $\Delta\langle L_y \rangle_{z=0}$ using the matrix elements of Eq. (6.1a) and agrees with the direct field calculation.

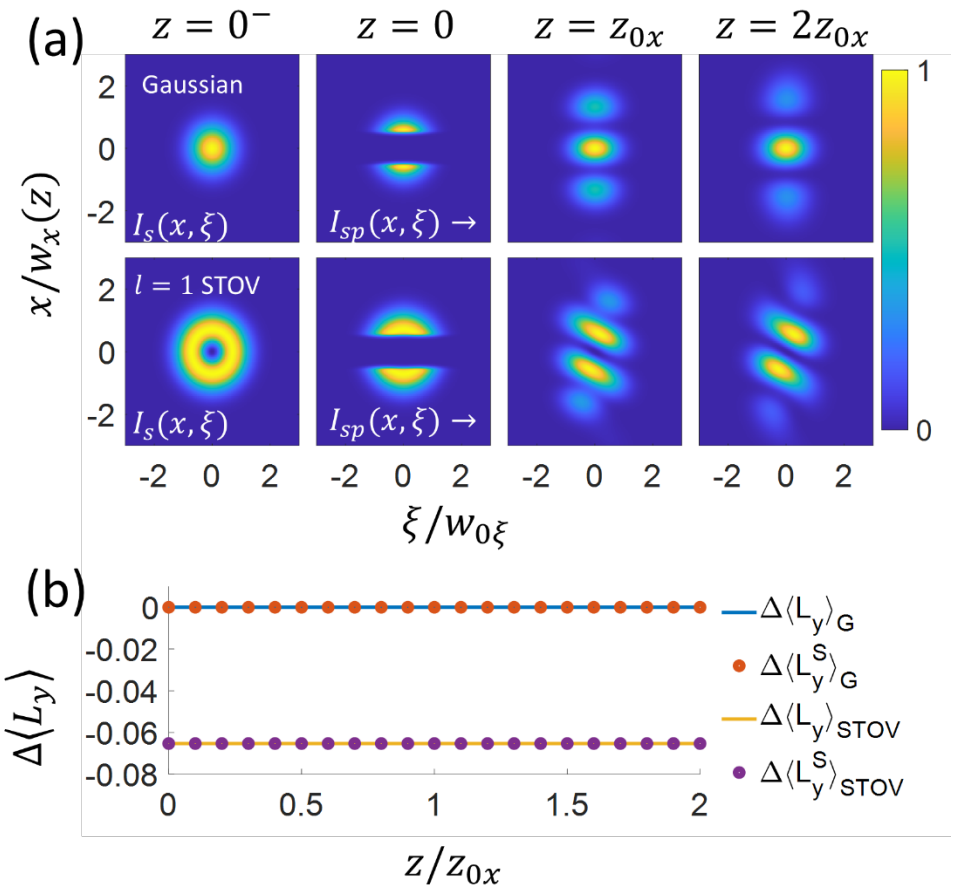

Figure 6.4. Effect of a non-energy-conserving pure amplitude perturbation $\Gamma(x,\xi) = 1 - \exp(-(x/h)^8)$ on pulses with and without transverse OAM. (a) Pre-perturbation $l = 1$ STOV and Gaussian pulse intensities $|E_s(x,\xi)|^2$ at $z = 0^-$, followed by the pulse intensity evolution $|E_{sp}(x, y = 0, \xi; z)|^2$ from $z = 0$ to $z = 2z_{0x}$ determined by **E** and **H** field propagation computed by YAPPE (Sec. 6.6). Here $2h = 100$ μm and $w_{0x} = w_{0\xi} = 100$ μm. (b) Change in transverse OAM per photon vs. z ($\Delta\langle L_y\rangle_z$) for the Gaussian and STOV pulses calculated directly from the fields using Eq. (6.1b) (points) and calculated using Eq. (6.1a) (solid lines).

To conclude this section, it is important to make a connection to the generation of transverse OAM-carrying pulses using our $4f$ pulse shaper [26,27,57]. The shaper generates STOVs from zero-OAM Gaussian input pulses by applying torque in the

spatio-spectral domain. One realization of the pulse shaper has a π-step phase plate in its Fourier $((x,\omega))$ plane and generates donut-shaped STOV pulses in the near field [27]. The phase jump in the (x,ω)-plane, $\Delta\varphi_p(x,\omega) = \arg(\tilde{E}_{sp}(x,\omega))$, where $\tilde{E}_{sp}$ is the time Fourier transform of the shaper-perturbed pulse, plays a role analogous to the phase change $\Delta\phi_p(x,\xi)$ in the spatiotemporal domain. Because we exist in a spatiotemporal rather than a spatio-spectral world, with clocks marking time as the dynamical running parameter, it is *spatiotemporal* perturbations that naturally appear in physical phenomena occurring outside of carefully designed instruments such as $4f$ pulse shapers.

6.4 Experimental Setup

The physical insight provided by the calculations of Sec. III led to our experimental design. To impart a spatiotemporal torque on an optical pulse via a perturbation $\Gamma(x,\xi) = |\Gamma(x,\xi)|e^{i\Delta\phi_p(x,\xi)}$, we impose a spatiotemporal refractive index perturbation in the propagation medium. This is accomplished by using a separate pulse to generate an ultrafast optical field ionization (OFI) air plasma at a controllable spacetime location; we call this spatiotemporal structure a "transient wire". As borne out by measurements and propagation simulations, the low-density plasma in the transient wire is dominantly a phase perturbation, with negligible energy removed from the pulse; effectively $|\Gamma(x,\xi)| = 1$. The transient wire has an ultrafast risetime and a narrow spatial width governed by the OFI rate, and a long lifetime governed by

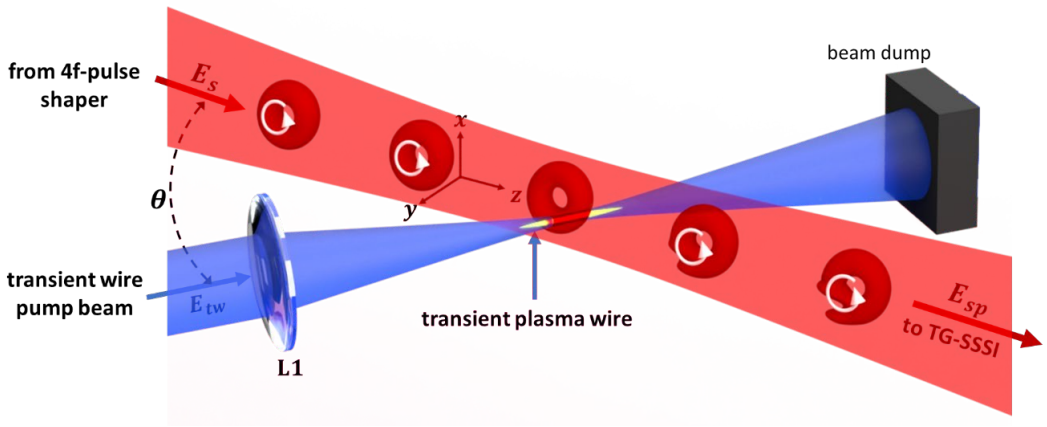

Figure 6.5. Configuration for measuring the effect of a transient phase perturbation on field E_s (from a $4f$ pulse-shaper), imposed by the ultrafast optical-field-induced (OFI) plasma induced by field E_{tw}. This OFI plasma is the "transient wire". The perturbed pulse E_{sp} and unperturbed pulse E_s (E_{tw} off) are measured by TG-SSSI (transient grating single shot supercontinuum spectral interferometry [28]). The angle between the beams is $\theta = 18.5°$. A detailed experimental diagram is shown in Sec. 6.6.

nanosecond timescale recombination: the spatiotemporal phase shift, $\Delta\phi_p(x,\xi)$, is therefore very well described by Eq. (6.4) or Eq. (6.7).

Figure 6.5 is a schematic diagram of the transient wire experiment; a more detailed diagram is presented in Sec. 6.6. Pulse E_s (red beam), either a Gaussian or $l = 1$ STOV pulse from a $4f$ pulse shaper [26–28,57], propagates through air and is intersected by a focused secondary pulse E_{tw} (blue beam) which generates an ultrafast risetime OFI plasma—the transient wire—at an adjustable spacetime location with respect to E_s. After the interaction, the perturbed pulse E_{sp} is relay imaged from 3 mm past the interaction plane (to avoid nonlinear distortion in the imaging) to our TG-SSSI diagnostic [28], which extracts its spatiotemporal amplitude and phase. With E_{tw} turned off, TG-SSSI measures the spatiotemporal amplitude and phase of the

unperturbed pulse E_s. Five synchronized beams are needed for this experiment, which are obtained by splitting the output beam of a 1 kHz repetition rate Ti:Sapphire laser ($\lambda_0 = 800$nm, 40 fs) to give (1) an input pulse to the $4f$ pulse shaper, with output pulse E_s (9.5 μJ, variable pulsewidth), (2) a focused transient wire beam E_{tw} (~250 μJ, 40 fs FWHM, spot size $w_{tw} = 40$ μm) that intersects the E_s beam at $\theta = 18.5°$, and (3) three pulses for TG-SSSI: twin probe and reference supercontinuum (SC) pulses E_{pr} and E_{ref} (with bandwidth $\Delta\lambda_{sc}$~160 nm centred at $\lambda_{sc} = 630$ nm) plus a spatial interferometry reference pulse $\mathcal{E}_i$ (5.5 μJ after 3nm bandpass filter centered at 800nm). The angle $\theta = 18.5°$ is chosen to allow angular separation of the beams to direct E_{sp} to the TG-SSSI diagnostic, and for sufficient spatial overlap of $\Delta\phi_p(x,\xi)$ along the propagation path of E_s.

6.4 Results and Discussion

An example of the transient wire perturbation of an $l = 1$ STOV pulse $E_s(x,\tau)$ is shown in Fig. 6.6, where here we use the local time coordinate $\tau = \xi/v_g$, and $(x,\tau) = (0,0)$ is taken as the spatiotemporal energy centre of E_s. Figure panels 6.5(a)-(c) show, respectively, the unperturbed $l = 1$ STOV pulse intensity $|E_s|^2$ (E_{tw} off), the perturbed pulse intensity $|E_{sp}|^2$ (E_{tw} on), and the transient-wire-induced phase shift $\Delta\phi_p(x,\tau) = \arg(E_{sp}) - \arg(E_s)$, all extracted using TG-SSSI [27,28]. The overlaid dashed red line shows the x-location of the perturbation, which was placed near the top of E_s (at $x_0 = 120\ \mu m$) to obtain appreciable $\Delta\langle L_y \rangle$, as motivated by the simulations in Fig. 6.2(b).

The plots represent a $\Delta y \sim 10$ μm slice of E_s and E_{sp} in the y direction, normal to the x-τ plane of the plots, where Δy is the width of the imaging spectrometer slit used in TG-SSSI (See [28] and Sec. 6.6).

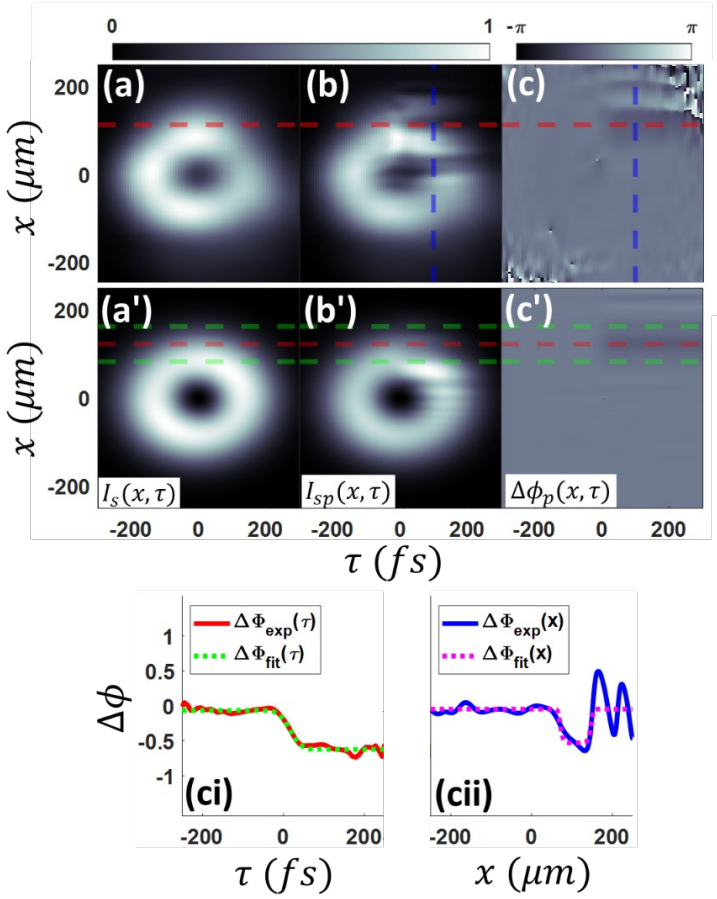

Figure 6.6. (a) TG-SSSI-measured $I_s = |\mathbf{E}_s(x,\tau)|^2$ (transient wire off). (b) and (c) TG-SSSI-measured $\left|\mathbf{E}_{sp}(x,\tau)\right|^2$ and $\Delta\phi_p(x,\tau)$ (transient wire on). (a′)-(c′) corresponding simulated $I_s^{sim} = \left|\mathbf{E}_s^{sim}(x,\tau)\right|^2$, $I_s^{sim} = \left|\mathbf{E}_{sp}^{sim}(x,\tau)\right|^2$, and $\Delta\phi_p^{sim}(x,\tau)$. (ci) Lineout of (c) along dashed red line (solid red) and fit (dotted green). (cii) Lineout of (c) along dashed blue line (solid blue) and fit (dotted pink). The fit curve neglects the oscillations on the right, which are due to the imaging plane being 3 mm past the interaction (see text). The fits in (ci) and (cii) are to $\Delta\phi_p^{sim}(x,\tau) = \frac{1}{2}\Delta\phi_{p0}\left(1 + \mathrm{erf}\left(\sqrt{2}\,(\tau-\tau_0)/h_\tau\right)\right)\exp(-((x-x_0)/h_x)^8)$, giving $h_\tau = h_\xi/v_g =$ 44 fs and $h_x = 40$ μm. In (ci) $x = 120$ μm $(= x_0)$, and in (cii) $\tau = 100$ fs.

From Fig. 6.6(c), the maximum phase shift induced by the OFI plasma is $\Delta\phi_{p0} = -0.45$, where E_{tw} was delayed so that the half-maximum phase shift $\Delta\phi_{p0}/2$, which defines the perturbation onset time τ_0, occurred for $\tau_0 = 0$. From nonlinear least squares fitting of measured $\Delta\phi_p(x,\tau)$ to Eq. (6.7), we extract the phase shift risetime $h_\tau = h_\xi/v_g$ ~44 fs and spatial half width at $1/e$ maximum h_x~40 μm, with data lineouts overlaid with fits in Figs. 6(ci) and (cii). The peak phase shift corresponds to an OFI plasma density $\Delta N_e = |\Delta\phi_{p0}| N_{cr}\lambda_0/2\pi L \approx 5\times10^{17}$ cm^{-3}, where $N_{cr} = 1.7\times10^{21}\, cm^{-3}$ is the critical density at $\lambda_0 = 800$ nm and $L = 2w_{tw}/\sin\theta$ ~250 μm is the OFI plasma length experienced by E_s. It is seen in Fig. 6.6(b) that an amplitude modulation feature lies below the dashed red line, starting near $\tau = 0$. This modulation is the diffractive consequence of the OFI-induced phase perturbation, and develops during the 3 mm of propagation from the interaction location to the TG-SSSI object plane. This is borne out by the simulations of Fig. 6.6(a')-(c') (performed using YAPPE (See Sec. 6.6), which show that similar diffractive modulations occur equidistantly above and below the dashed red line, but have no effect on the change in angular momentum of the pulse. Panel 6.6(a′) shows the simulated unperturbed pulse $|E_s^{sim}|^2$ (E_{tw} off) and panel 6.6(b′) shows the perturbed pulse $|E_{sp}^{sim}|^2$ (E_{tw} on), both 3 mm past the intersection with E_{tw}. Here, the perturbation by E_{tw} is simulated by imposing on E_s^{sim} the perturbation $\Gamma(x,\tau) = |\Gamma(x,\tau)|e^{i\Delta\phi_p(x,\tau)}$, with $|\Gamma(x,\tau)| = 1$ and $\Delta\phi_p^{sim}(x,\tau)$ from Eq. (6.7), using h_τ and h_x

derived from the fit discussed above. The red and green horizontal dashed lines in panels 6.6(a′)-(c′) mark the centre ($x = x_0$) and $\pm h_x$ edges of $\Delta\phi_p^{sim}(x,\tau)$.

In our main experiment, the results of which are shown in Fig. 6.7, we varied the spatiotemporal torque on both STOV and Gaussian pulses by scanning the transient wire onset time τ_0. For torquing the STOV pulse, we spatially placed the wire near the top and bottom edges of the pulse, $x_0 = \pm 120$ μm (Figs. 6.7(a) and 6.7(b)), and at $x_0 = 60$ μm for the Gaussian pulse (Fig. 6.7(c)). The onset time was scanned from -200fs to 800fs in steps of $\Delta\tau_0 \sim 66$ fs, and the TG-SSSI-extracted complex spatiotemporal fields $E_s(x,\tau)$ and $E_{sp}(x,\tau)$ were then used to determine $\Delta\langle L_y\rangle$ at each delay using Eq. 6.1(a) and Eq. (6.1b), which we label as $\Delta\langle L_y\rangle_{1a}$ and $\Delta\langle L_y\rangle_{1b}$. In Eq. (1a), we use the STOV OAM operator $L_y = -i\xi\,\partial/\partial x$ (for $\beta_2 = 0$), while in Eq. (1b), the $\mathbf{H}_{s,sp}(x,\xi)$ fields are calculated as the 2D inverse Fourier transform of $\tilde{\mathbf{H}}_{s,sp}(\mathbf{k},\omega) = (c/\omega)\mathbf{k} \times \tilde{\mathbf{E}}_{s,sp}(\mathbf{k},\omega)$, where $\tilde{\mathbf{E}}_{s,sp}(\mathbf{k}-\mathbf{k}_0,\omega)$ is the discrete 2D Fourier transform of the measured $\mathbf{E}_{s,sp}(x,\xi)$ fields, and $\mathbf{k}_0 = k_0\hat{\mathbf{z}}$ is the pulse central wavenumber.

The top two rows in Figs. 6.7(a)-(c) plot $I_{sp}(x,\tau) = |\mathbf{E}_{sp}(x,\tau)|^2$ and $\Delta\phi_p(x,\tau) = \arg(E_{sp}(x,\tau)) - \arg(E_s(x,\tau))$, with all amplitude and phase data extracted from raw TG-SSSI frames averaged over 500-750 shots. The lower panels plot $\Delta\langle L_y\rangle_{1a}$ and $\Delta\langle L_y\rangle_{1b}$ versus transient wire onset delay. These plots are in excellent agreement, confirming that our expression for the transverse OAM operator L_y (Ref. [30] and Eq. (6.2)) is correct. Overlaid in Figs. 6.7(a)-(c) are curves for

$\Delta\langle L_y\rangle_{theory}$, using Eqs. (6.6a) and (6.6b) for $\Delta\langle L_y\rangle_{\mathrm{G}}$ and $\Delta\langle L_y\rangle_{\mathrm{STOV}}$. Agreement with the experimental results is excellent. In each experiment in Fig. 6.7, the measured experimental parameters were slightly different. These are listed in the figure caption and were incorporated into the expressions for $\Delta\langle L_y\rangle_{\mathrm{G}}$ and $\Delta\langle L_y\rangle_{\mathrm{STOV}}$.

Figure 6.7. Effect of transient wire onset time τ_0 on changing the transverse OAM of STOV and Gaussian pulses. Onset time is scanned between -200 fs and 800 fs in $\Delta\tau_0 = 66$ fs steps. (a) $l = 1$ STOV pulse, with transient wire centred at $x_0 = +120$ μm; (b) $l = 1$ STOV pulse, with transient wire centred at $x_0 = -120$ μm; (c) Gaussian pulse ($l = 0$), with transient wire centred at $x_0 = 60$ μm. The top two rows in (a)-(c) are $I_{sp}(x,\tau) = |E_{sp}(x,\tau)|^2$ and $\Delta\phi_p(x,\tau) = \arg(E_{sp}) - \arg(E_s)$, where $E_s(x,\tau)$ and $E_{sp}(x,\tau)$ are the unperturbed and perturbed complex fields extracted from TG-SSSI measurements. The spatial location of the perturbation is indicated by the red dotted lines. The bottom panels in (a)-(c) plot $\Delta\langle L_y\rangle_{1a}$ and $\Delta\langle L_y\rangle_{1b}$, which are the change in spatiotemporal OAM per photon computed by inserting the measured E_s and E_{sp} into Eq. (6.1a), and the **E** and **H** fields computed from them into Eq. (6.1b). The error bars are the $\pm$ standard deviation over 500-750 shots of extracted data. Overlaid in (a)-(c) is $\Delta\langle L_y\rangle_{\mathrm{theory}}$, calculated using Eqs. (6.6a) and (6.6b), in which we use measured and fit quantities. For $\Delta\langle L_y\rangle_{\mathrm{theory}}$ in panel (a): ($\Delta\phi_{p0} = -0.45$, $w_{0x} = 120$ μm , $w_{0\xi} = 56$ μm, $h = 40$ μm, $x_0 = 120\,\mu m$). For $\Delta\langle L_y\rangle_{\mathrm{theory}}$ in panel (b): ($\Delta\phi_{p0} = -0.21$, $w_{0x} = 110$ μm , $w_{0\xi} = 56$ μm, $h = 40$ μm, $x_0 = -120\,\mu m$). For $\Delta\langle L_y\rangle_{\mathrm{theory}}$ in panel (c): ($\Delta\phi_{p0} = -0.31$, $w_{0x} = 100$ μm , $w_{0\xi} = 61$ μm, $h = 40$ μm, $x_0 = 60\,\mu m$). The " $-\infty$" mark on the time axes refers to the $\xi_0 \to -\infty$ limit of $\Delta\langle L_y\rangle_{\mathrm{theory}}$.

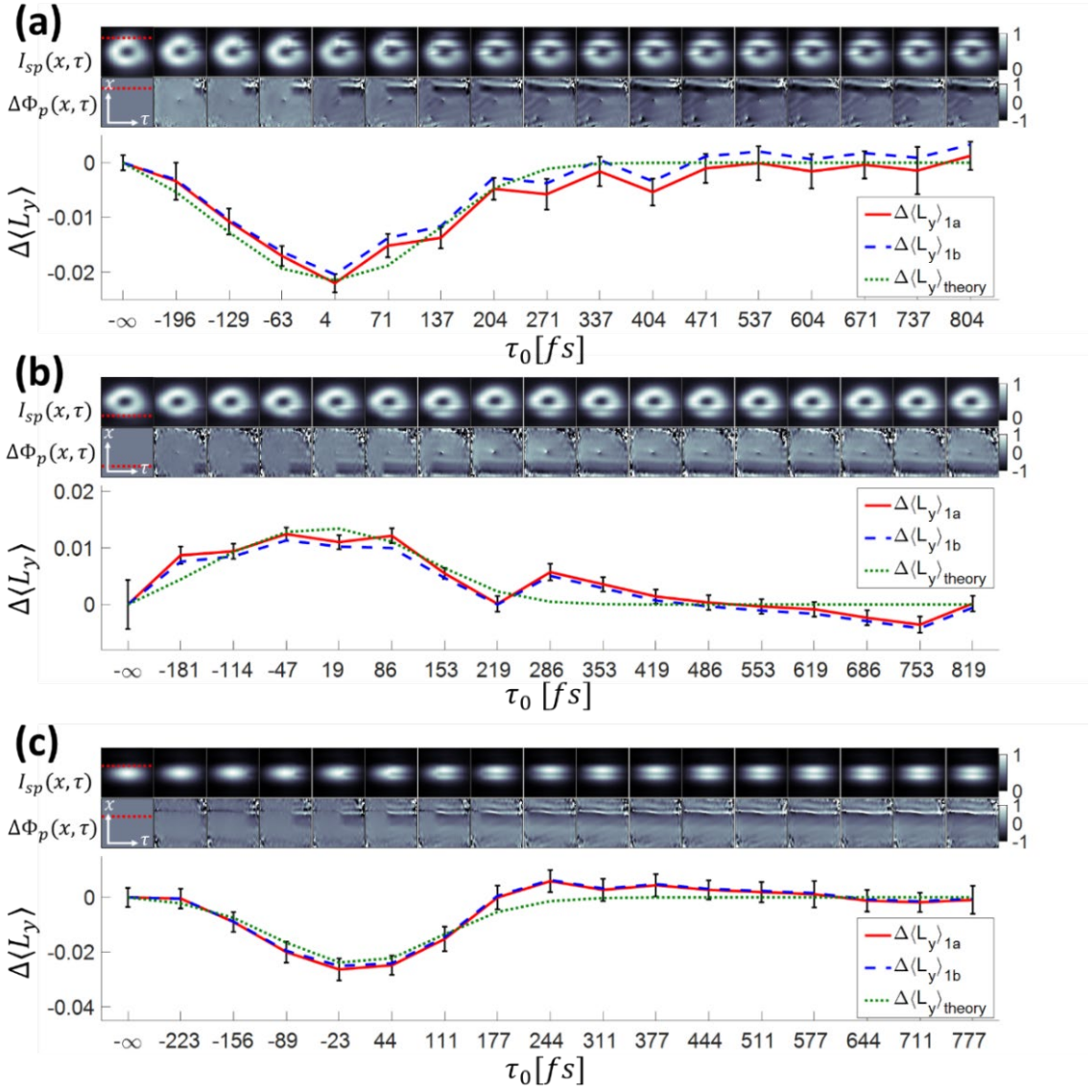
(a)
$I_{sp}(x,\tau)$
$\Delta\Phi_p(x,\tau)$
$\Delta\langle L_y\rangle$
$\Delta\langle L_y\rangle_{1a}$
$\Delta\langle L_y\rangle_{1b}$
$\Delta\langle L_y\rangle_{theory}$
-∞ -196 -129 -63 4 71 137 204 271 337 404 471 537 604 671 737 804
$\tau_0[fs]$
(b)
$I_{sp}(x,\tau)$
$\Delta\Phi_p(x,\tau)$
$\Delta\langle L_y\rangle$
$\Delta\langle L_y\rangle_{1a}$
$\Delta\langle L_y\rangle_{1b}$
$\Delta\langle L_y\rangle_{theory}$
-∞ -181 -114 -47 19 86 153 219 286 353 419 486 553 619 686 753 819
$\tau_0\ [fs]$
(c)
$I_{sp}(x,\tau)$
$\Delta\Phi_p(x,\tau)$
$\Delta\langle L_y\rangle$
$\Delta\langle L_y\rangle_{1a}$
$\Delta\langle L_y\rangle_{1b}$
$\Delta\langle L_y\rangle_{theory}$
-∞ -223 -156 -89 -23 44 111 177 244 311 377 444 511 577 644 711 777
$\tau_0[fs]$

The results of Fig. 6.7 confirm our Sec. 6.3 theory: once the OFI plasma phase transient is shifted away from the pulse envelope, $\Delta\langle L_y\rangle \to 0$. To impart spatiotemporal torque and a change in transverse OAM, the perturbation transient must temporally overlap with the pulse energy density distribution. Refractive index transients with timescales much longer than the pulse temporal envelope have little effect on the transverse OAM of a pulse. In general, irrespective of its spatial location or peak amplitude, the more imbalanced a transient spatiotemporal perturbation is across the temporal centre of energy of an optical pulse, the greater effect it has on changing the transverse OAM.

6.5 Conclusions

We have demonstrated that the transverse orbital angular momentum (OAM) per photon of an electromagnetic pulse can be changed only by a transient phase perturbation comparable to the pulse envelope and overlapping with it, or by a non-energy-conserving amplitude perturbation if the pulse already has transverse OAM. Our half-integer theory of STOV pulse OAM [30] is in excellent agreement with our experiments and with propagation simulations directly using the **E** and **H** fields. The experiments of this chapter, in which spatiotemporal torques were faster than the short pulses to which they were applied, would not have been possible without our high bandwidth, high time resolution single shot technique—TG-SSSI [28]— for STOV pulse amplitude and phase recovery.

The concept of spatiotemporal torque, introduced in this chapter, provides insight into the dynamics leading to changes in transverse OAM: the effective force, manifested as a spatiotemporal phase gradient supplied by the perturbation, is weighted by the spacetime lever arm and the electromagnetic energy density distribution. If the initial field is a STOV pulse with zero energy density at the singularity (an "edge-first flying donut" [27]), spatiotemporal torquing can be analogized by mechanical torque on a rotating hoop, where maximum change in OAM is obtained by applying force at the outer rim, where the product of lever arm and mass density is maximum. However, unlike in the mechanical case, a spatiotemporal torque applied to an optical pulse changes the OAM of all particles (photons) identically. The other way to change transverse OAM is to remove energy from a pulse already with transverse OAM; this can be accomplished by a non-energy-conserving amplitude perturbation. This imposes a new spatiotemporal distribution of the remaining energy and thus a new transverse OAM per photon. Here, the mechanical analogy is location-specific mass removal from a spinning wheel.

Our results point the way to methods of distortion-free encoding of information in transverse OAM, for example, in propagation through turbulent atmosphere. The shortest transient timescale for turbulent refractive index fluctuations in the atmosphere is a few milliseconds [128], at least 10 orders of magnitude longer than a ~100 fs duration ultrashort pulse, so air turbulence acts as a weak stationary perturbation with no effect on the expectation value of transverse OAM per photon. While the turbulence-induced *spatial* phase shifts can manifest as transverse (xy) spatial distortion of the

beam, the encoded spatio-temporal phase structure makes possible the extraction of time-based information with fast retrieval schemes.

6.6 Additional Material

C.1 Conservation of transverse OAM operator L_y under non-paraxial propagation

In Ref. [30], we showed that the transverse OAM operator $L_y = -i(\xi\,\partial/\partial x + \beta_2 x\,\partial/\partial\xi)$ was conserved under paraxial propagation. Here, we start with the non-paraxial propagation equation for the field envelope $A(\mathbf{r}_\perp, z, t)$

$$\frac{\partial^2 A}{\partial z^2} + i2k_0\frac{\partial}{\partial z} = -\nabla_\perp^2 A - i2k_0 k_0'\frac{\partial A}{\partial t} + k_0 k_0''\frac{\partial^2 A}{\partial t^2}, \tag{C1}$$

In the group velocity frame, using $\zeta = z$, $\xi = v_g t - z$, $H = -\nabla_\perp^2 + \beta_2\,\partial^2/\partial\xi^2$, and $p_z^2 = -\partial^2/\partial z^2$ gives

$$\frac{\partial A}{\partial \zeta} = \frac{i}{2k_0}\left[HA - \left(\frac{\partial^2 A}{\partial \zeta^2} - 2\frac{\partial^2 A}{\partial\zeta\partial\xi} + \frac{\partial^2 A}{\partial\xi^2}\right)\right] = \frac{i}{2k_0}[H - p_z^2]A\ . \tag{C2}$$

Then for $\langle L_y\rangle = \langle A|L_y|A\rangle$,

$$\frac{d}{dz}\langle L_y\rangle = \left\langle\frac{\partial}{\partial z}\,A\middle|L_y\middle|A\right\rangle + \left\langle A\middle|\frac{\partial}{\partial z}L_y\middle|A\right\rangle + \left\langle A\middle|L_y\middle|\frac{\partial}{\partial z}A\right\rangle, \tag{C3}$$

Since L_y does not explicitly depend on z, and since H, L_y, and p_z are all Hermitian, Eqn (C3) becomes

$$\frac{d}{dz}\langle L_y\rangle = \frac{i}{2k_0}\langle A|[H, L_y]|A\rangle + \frac{i}{2k_0}\langle A|[L_y, p_z^2]|A\rangle = 0, \tag{C4}$$

because L_y commutes with both H and p_z^2.

C.2 Effect of a spatiotemporal perturbation on transverse OAM

The expectation values of L_y per photon for the unperturbed and perturbed pulses, $A_s(x,\xi) = |A_s(x,\xi)|e^{i\phi_s(x,\xi)}$ and $A_{sp}(x,\xi) = \Gamma(x,\xi)A_s(x,\xi) = |\Gamma(x,\xi)|e^{i\Delta\phi_p(x,\xi)}A_s(x,\xi)$, are

$$\langle L_y\rangle_{s,sp} = u_{s,sp}^{-1}\langle E_{s,sp}|L_y|E_{s,sp}\rangle \ . \tag{C5}$$

This gives

$$\langle L_y\rangle_s = u_s^{-1}\int dxd\xi|A_s|^2\left(\xi\frac{\partial\phi_s}{\partial x} + \beta_2 x\frac{\partial\phi_s}{\partial\xi}\right) , \tag{C6a}$$

and

$$\begin{aligned}\langle L_y\rangle_{sp} = u_{sp}^{-1}\int dx\, d\xi\, [&-i|A_s|^2|\Gamma|\left(\xi\frac{\partial|\Gamma|}{\partial x} + \beta_2 x\frac{\partial|\Gamma|}{\partial\xi}\right)\\ &- i|\Gamma|^2|A_s|\left(\xi\frac{\partial|A_s|}{\partial x} + \beta_2 x\frac{\partial|A_s|}{\partial\xi}\right)\\ &+ |A_s|^2|\Gamma|^2\left(\xi\frac{\partial\Delta\phi_p}{\partial x} + \beta_2 x\frac{\partial\Delta\phi_p}{\partial\xi}\right)\\ &+ |A_s|^2|\Gamma|^2\left(\xi\frac{\partial\phi_s}{\partial x} + \beta_2 x\frac{\partial\phi_s}{\partial\xi}\right)] \ ,\end{aligned} \tag{C6b}$$

The first two terms in Eq. (C6b) integrate to zero, yielding

$$\begin{aligned}\Delta\langle L_y\rangle &= \langle L_y\rangle_{sp} - \langle L_y\rangle_s \\ &= iu_{sp}^{-1}\int dx\, d\xi\, \Big[|A_s|^2|\Gamma|^2 L_y\Delta\phi_p \\ &\quad + |A_s|^2\left(|\Gamma|^2 - \frac{u_{sp}}{u_s}\right)L_y\phi_s\Big]\ .\end{aligned} \tag{C7}$$

For an initial pulse with zero transverse OAM, such as a Gaussian, $L_y\phi_s = 0$ and

$$\Delta\langle L_y\rangle = iu_{sp}^{-1}\int dx d\xi\ |A_s|^2|\Gamma|^2 L_y\Delta\phi_p\ . \tag{C8}$$

For a phase-only perturbation $|\Gamma(x,\xi)| = 1$, $u_{sp} = u_s$, and Eq. (C8) also applies.

C.3 Effect of a spatiotemporal perturbation on transverse OAM

Recent work [87,125] has asserted that the "canonical" operator for intrinsic transverse OAM is

$$\pounds_y = -i\left(\xi\frac{\partial}{\partial x} - x\frac{\partial}{\partial\xi}\right), \tag{C9}$$

where x and ξ are as defined earlier. In the formulation of [87,125], x and ξ are treated on an equal footing, just as x and y are treated in the L_z operator for longitudinal OAM.

Adoption of $\pounds_y$ assumes unphysical effects, including super- and sub-luminal energy density flow around the spatiotemporal vortex singularity in vacuum, and non-conservation [30,129]. While any valid angular momentum quantity should be conserved with propagation, $\pounds_y$ is not. Namely,

$$\frac{d}{dz}\langle \text{£}_y \rangle = \frac{i}{2k_0}\langle [H, \text{£}_y] \rangle = k_0^{-1}(1+\beta_2)\left\langle \frac{\partial^2}{\partial x \partial \xi} \right\rangle_{z=0}, \tag{C10}$$

which is non-zero except if $\beta_2 = -1$ (when $L_y \to \text{£}_y$) or when there is spatiotemporal field symmetry.

We test the consequences of using £_y with a spatiotemporally asymmetric field. Such a field can be generated, as seen in Figs. 6.6 and 6.7, when a spatiotemporal perturbation is applied to a symmetric pulse. Here, we apply at $z = 0^-$ a phase-only perturbation $\Gamma(x,\xi) = e^{i\Delta\phi_p(x,\xi)}$, with $\Delta\phi_p(x,\xi)$ from Eq. (C7) (with $\Delta\phi_{p0} = -0.5$, $x_0 = -100$ μm, $\xi_0 = 0, h_x = 50$ μm, and $h_\xi = 50$ μm) to the Gaussian pulse A_{G} of Eq. 6.5(a). The transverse OAM of A_{G} is zero. Non-paraxial propagation evolution of the perturbed field $A_{sp}(x,y,\xi;z) = \Gamma(x,\xi)A_{\mathrm{G}}(x,y,\xi;z)$ is then computed using our code YAPPE. In Fig. C1, we plot $\Delta\langle L_y \rangle_z = u_{sp}^{-1}\langle A_{sp}|L_y|A_{sp}\rangle_z$ and $\Delta\langle \text{£}_y \rangle_z = u_{sp}^{-1}\langle A_{sp}|\text{£}_y|A_{sp}\rangle_z$ as a function of propagation distance z. The immediate post-perturbation values, $\Delta\langle L_y \rangle_{z=0}$ and $\Delta\langle \text{£}_y \rangle_{z=0}$, are shown in the figure; these differ. It is clear that $\Delta\langle L_y \rangle_z$ is conserved with propagation, while $\Delta\langle \text{£}_y \rangle_z$ is not. The divergence of $\Delta\langle \text{£}_y \rangle_z$ is predicted by Eq. (C10) and is a consequence of the non-commutation of £_y and the propagation operator H. This increase is linear in z, with slope $d\langle \text{£}_y \rangle/dz = k_0^{-1}\langle \partial^2/\partial x \partial \xi \rangle_{z=0}$, and is in excellent agreement with $\Delta\langle \text{£}_y \rangle_z = u_{sp}^{-1}\langle A_{sp}|\text{£}_y|A_{sp}\rangle_z$. Calculating the change in transverse OAM using Eq. 6.1(b), with

the **E** and **H** fields propagated non-paraxially by the YAPPE simulation, gives the blue points labelled as $\Delta\langle L_y^S\rangle_z$; these agree with $\Delta\langle L_y\rangle_z$.

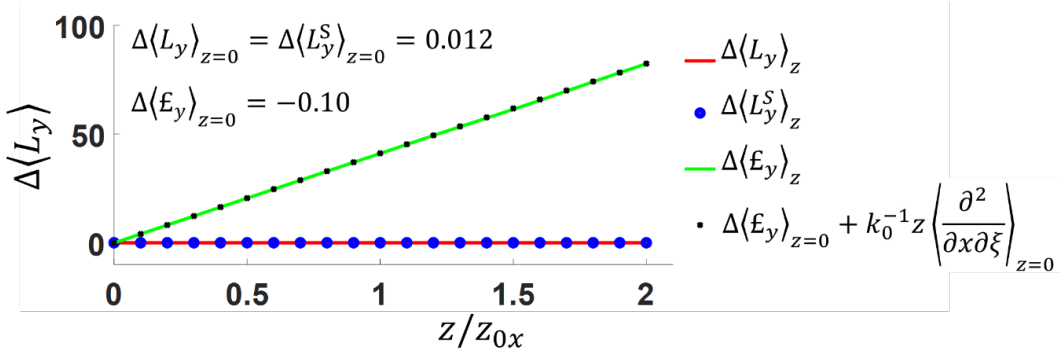

Figure C1. Propagation evolution of $\Delta\langle L_y\rangle = u_{sp}^{-1}\langle A_{sp}|L_y|A_{sp}\rangle_z$ (red curve) and $\Delta\langle \pounds_y\rangle = u_{sp}^{-1}\langle A_{sp}|\pounds_y|A_{sp}\rangle_z$ (green curve), where the z-evolution of $A_{sp}(x,y,\xi;z)$ is non-paraxially computed using our code YAPPE. The perturbation (given by Eq. (6.7), with $\Delta\Phi_{p0} = -0.5$, $x_0 = -100$ μm, $\xi_0 = 0, h_x = 50$ μm, and $h_\xi = 50$ μm) is applied to the Gaussian pulse of Eq. 6.5(a), with $w_{ox} = 100$μm and $w_{0\xi} = 100$ μm. The immediate post-perturbation OAM changes are $\Delta\langle L_y\rangle_{z=0} = 0.012$ and $\Delta\langle \pounds_y\rangle_{z=0} = -0.10$. Also plotted: Large blue points $\Delta\langle L_y^S\rangle$ computed using Eq. 1(b), with the E and H fields propagated non-paraxially with the code YAPPE, and small black points computed as $\Delta\langle \pounds_y\rangle_z = \Delta\langle \pounds_y\rangle_{z=0} + k_0^{-1} z\langle \partial^2/\partial x\partial\xi\rangle_{z=0}$ from integration of Eq. (C10), where $\langle \partial^2/\partial x\partial\xi\rangle_{z=0} = \langle A_{sp}|\partial^2/\partial x\partial\xi|A_{sp}\rangle$ for $A_{sp} = A_{sp}(x,y,\xi;z=0)$.

Note that non-conservation of $\pounds_y$ is independent of choice of origin, whether it is the perturbed pulse centre of energy $\mathbf{r}'_{sp}$ (as in Fig. C1)) or the "photon number centroid" [125], so $\pounds_y$ cannot be corrected with extrinsic OAM contributions. This is because non-conservation of $\pounds_y$ is caused by the inclusion, even in vacuum, of a non-zero linear momentum density $p_\xi = -i\,\partial/\partial\xi$. As the propagating pulse spatially (transversely) diffracts, with its width in x increasing, the contribution of xp_ξ to $\pounds_y$

increases and $\langle A_{sp}|\pounds_y|A_{sp}\rangle_z$ unavoidably increases with propagation. There are circumstances, not involving pulse propagation, where $\pounds_y$ is appropriate to use. One such example is a vortex stationary in the lab frame, whose transverse OAM, say along $\hat{\mathbf{y}}$, can be described in x-z space coordinates [130].

The choice of origin as the center of energy is essential to isolating the intrinsic OAM from the extrinsic OAM. While Eq. (C4) proves that OAM calculated for any choice of origin is conserved with propagation, to compute the intrinsic OAM in simulations and from experimental data, we always choose the center of energy as the origin [131], thereby automatically removing the extrinsic part of the OAM. A straightforward mechanical analogy also makes this point: the intrinsic OAM of a massive blob, consisting of point particles of varying mass, must be calculated with respect to the centre of mass density.

C.4 Application of Spatiotemporal phase perturbation localized in space and time

As discussed in Sec. 6.4, our transient wire spatiotemporal perturbation is well modeled by Eq. (6.4) or Eq. (6.7), which describe a narrow spatial structure with a fast turn-on time and no turn-off. To more finely map the effect of spatiotemporal perturbations on electromagnetic pulses, we consider a phase perturbation $\Gamma(x,\xi) = e^{i\Delta\phi_p(x,\xi)}$ localized in both space and time and centered at (x_0,ξ_0): $\Delta\phi_p(x,\xi) = \Delta\phi_{p0}\exp[-(x-x_0)^2/h_x^2 - (\xi-\xi_0)^2/h_\xi^2]$. Figure C2 shows the change in transverse

OAM per photon $\Delta\langle L_y\rangle_{x_0,\xi_0}$ for various pulses as a function of (x_0, ξ_0), plotted from analytic expressions determined using Eq. (6.1a). In all cases, we take $\beta_2 = 0$ and the perturbation spatial width $h_x/w_{0x} = 0.25$, with the other parameters listed on the panels and in the figure caption.

Examination of Fig. C2(a), for spatiotemporal torque applied to the $l = 1$ STOV pulse of Eq. 6.5(b), confirms our intuitive expectations from Sec. 6.3. Torque is maximized when the perturbation peak (x_0, ξ_0) is placed at the spatiotemporal locations with appreciable energy density and lever arm (see Eq. (6.3)), while dropping to zero when crossing lines marking the spatial and temporal centers of energy, where torque contributions from opposites sides in space and time cancel. Combined, the two effects give rise to the characteristic 4-lobed patterns plotted. A similar pattern appears in the torquing of Gaussian pulses. It is interesting to note that the locations of maximum torque are spatiotemporally outside the peak intensity contour of A_{STOV}, which is marked with a dashed red circle. This is the effect of lever arm weighting of the optical energy density in Eq. (6.3). A weaker 4-lobed structure with opposite polarity can be seen inside the peak intensity contour; here $h_x/w_{0x} = 0.25$ and $h_\xi/w_{0\xi} = 0.25$ are small enough for the perturbation to torque the inside of the STOV "wheel". This structure disappears for the larger values of $h_\xi/w_{0\xi}$ in Fig. C2(b). Also evident is the linear scaling of $\Delta\langle L_y\rangle$ with α, which stems from our theory of STOV transverse OAM [30].

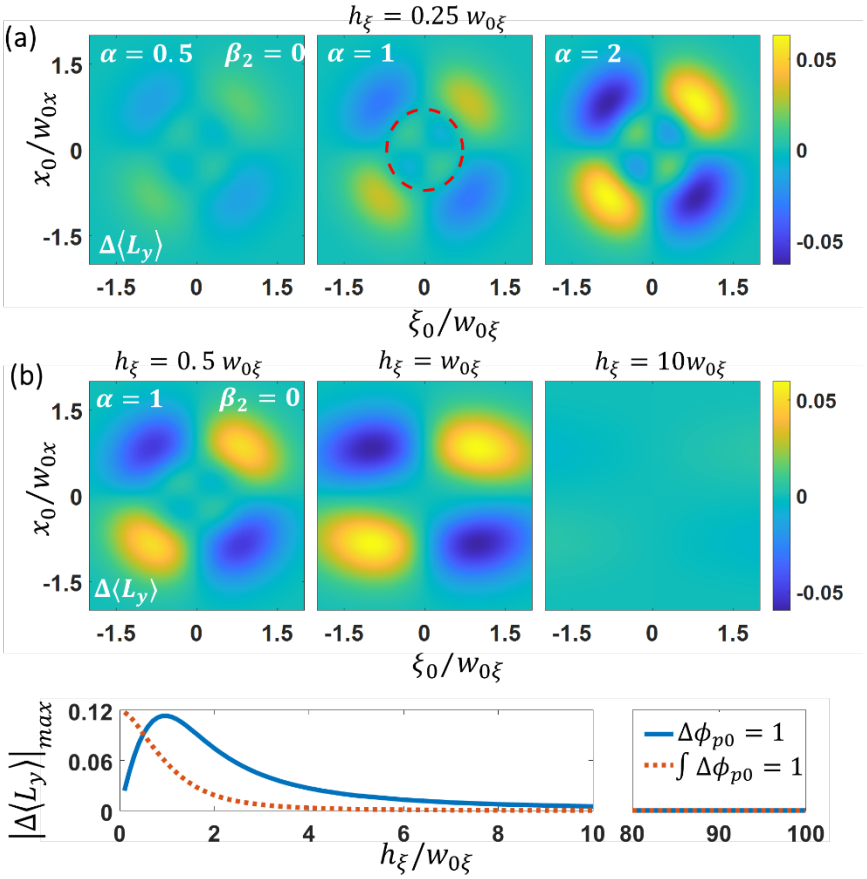

Figure C2. Plots of analytic solutions (See Sec. 6.C.7) for change in transverse OAM per photon, $\Delta\langle L_y\rangle_{x_0,\xi_0}$, imparted to an optical pulse as function of (x_0, ξ_0) by a spatiotemporal phase perturbation $\Gamma(x,\xi) = \exp(i\Delta\phi_p(x,\xi))$. Here $\Delta\phi_p(x,\xi) = \Delta\phi_{p0}\exp[-(x-x_0)^2/h_x^2 - (\xi-\xi_0)^2/h_\xi^2$, $\Delta\phi_{p0} = 1$, $\beta_2 = 0$ and $h_x/w_{0x} = 0.25$. (a) perturbation $\Gamma(x,\xi)$ applied to a $l = 1$ STOV pulse $A_{\text{STOV}}(x,\xi) = (\xi/w_{0\xi} + i\,x/w_{0x})A_{\text{G}}(x,\xi)$ for $h_\xi/w_{0\xi} = 0.25$ and $\alpha = w_{0\xi}/w_{0x}$ =0.5, 1, and 2. The red dashed circle in the centre panel is the contour of peak intensity of $|A_{\text{STOV}}|^2$. (b) $\Gamma(x,\xi)$ applied to $A_{\text{STOV}}(x,\xi)$ as in (a), here with $\alpha = 1$ and transient width $h_\xi/w_{0\xi} = 0.5, 1,$ and 10. The curves immediately below plot the maximum absolute change in OAM ($|\Delta\langle L_y\rangle_{x_0,\xi_0}|_{max}$) vs. transient width h_ξ, for the cases of fixed peak phase shift $\Delta\phi_{p0} = 1$ and constant integrated shift $\int dx d\xi \Delta\phi_p(x,\xi) = 1$. The overlaid dashed ring follows the maximum intensity contour of A_{STOV}.

The effect of a temporally widening $\Delta\phi_p(x,\xi)$ of fixed peak amplitude is plotted in Fig. C3(b). It is seen that in the middle panel (for the middle pulsewidth), the torque is both larger in size and is effectively applied over a wider spatiotemporal area than for perturbations of shorter and longer pulsewidths. In particular, the very long perturbation of the rightmost panel registers negligible $\Delta\langle L_y\rangle_{x_0,\xi_0}$ anywhere, consistent with the perturbation approaching steady state. The blue curve, just below, plots $\left|\Delta\langle L_y\rangle_{x_0,\xi_0}\right|_{max}$, showing that a perturbation transient comparable to the optical pulsewidth ($h_\xi/w_{0\xi}\sim 1$) is most effective in maximizing duration of torque. For the case of an energy-limited perturbation, increasing its duration h_ξ may result in decreasing $\Delta\phi_{p0}$. The red dashed curve, using the constraint $(h_x h_\xi)^{-1}\int dx d\xi\ \Delta\phi_p(x,\xi) = 1$, shows this effect, where in this case the most effective perturbation is the shortest.

C.5 Detailed Experimental Setup

The detailed experimental setup is shown in Fig. C3.

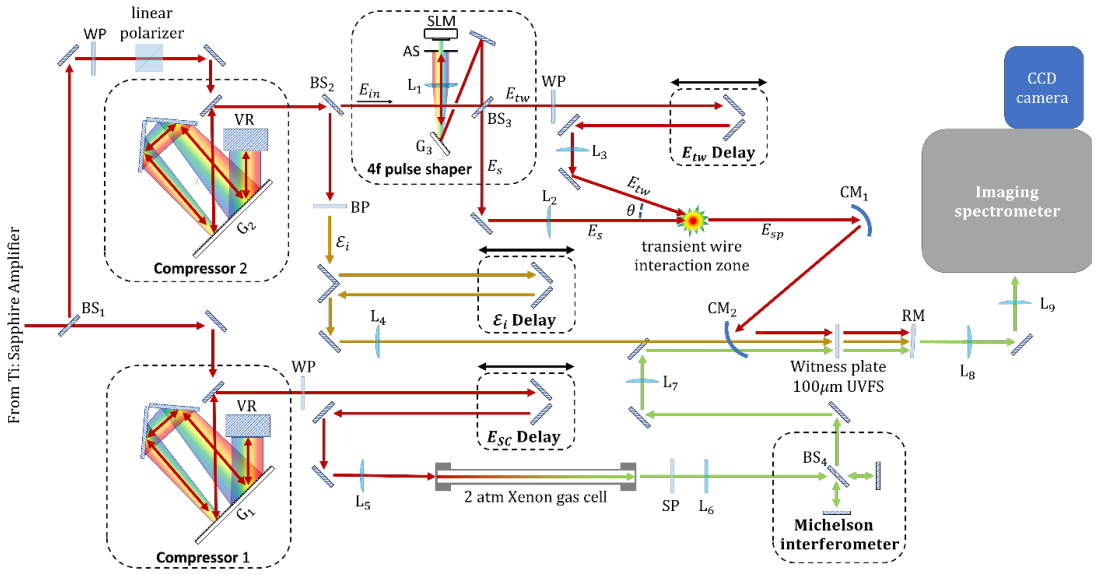

Figure C3. Detailed experimental configuration. Compressor 1 adjusts pulse for $4f$ pulse shaper, TG-SSSI spatial interferometry pulse $\mathcal{E}_i$ and transient wire pulse E_{tw}. Compressor 2 adjusts pulse for TG-SSSI probe and reference supercontinuum pulses [28]. CM: concave mirror, BP: bandpass filter 3nm FWHM, 800nm center, AS: adjustable slit, SLM: spatial light modulator, WP: λ/2 waveplate, SP: short pass filter, transmits below 750nm, VR: vertical retroreflector, RM: pump/interferometric reference rejection mirror, G: grating, L: lens.

C.6 Propagation Simulations

3D+1 (3 space dimensions plus time) simulations of non-paraxial pulse propagation were performed using our UPPE (unidirectional pulse propagation equation) [83,84] implementation called YAPPE (yet another pulse propagation effort) [132]. For linear propagation in a dispersive medium in the group velocity frame. YAPPE solves a system of ordinary differential equations,

$$\frac{\partial}{\partial z}\tilde{E}_{k_x,k_y}(\omega,z) = iK_z\left(\omega,k_x,k_y\right)\tilde{E}_{k_x,k_y}(\omega,z)\,, \tag{C11a}$$

$$\tilde{E}_{k_x,k_y}(\omega, z) = \tilde{E}_{k_x,k_y}(\omega, z = 0)\exp\left(iK_z(\omega, k_x, k_y)z\right). \quad \text{(C11b)}$$

Here, $\tilde{E}_{k_x,k_y}(\omega, z) = \mathcal{F}_{x,y,\tau}\{E(x, y, \tau; z)\}$ is the 3D Fourier transform of the spacetime field $E(x, y, \tau; z)$, where $\tau = t - z/v_g(\omega)$ is local time in the pulse frame of reference, ω is the angular frequency, $v_g(\omega)$ is the frequency-dependent group velocity in the medium, and $K_z(\omega, k_x, k_y) = ((\omega/v_g(\omega))^2 - \left(k_x^2 + k_y^2\right))^{1/2} - \omega/v_g(\omega)$, which models diffraction and dispersion. The transverse wavenumber (k_x, k_y) indexes the system of equations (Eq. (C11)), which are numerically solved. To recover the field in the spacetime domain, a 3D inverse Fourier transform is performed, $E(x, y, \tau; z) = \mathcal{F}^{-1}_{k_x,k_y,\omega}\left\{\tilde{E}_{k_x,k_y}(\omega, z)\right\}$.

C.7 Spatiotemporal Phase Perturbations localized in time and space

We consider the effect of a localized pure phase perturbation $\Gamma(x, \xi) = \exp(i\Delta\Phi_p(x, \xi))$ centered at (x_0, ξ_0), where

$$\Delta\phi_p(x, \xi) = \Delta\phi_{p0}\exp\left[-\frac{(x - x_0)^2}{h_x^2} - \frac{(\xi - \xi_0)^2}{h_\xi^2}\right], \quad \text{(C12)}$$

on both Gaussian and STOV pulses. We first consider the Gaussian at $z = 0$,

$$A_G(x, \xi) = \mathrm{A}_0\exp\left(-\frac{x^2}{w_{0x}^2} - \frac{\xi^2}{w_{0\xi}^2}\right), \quad \text{(C13)}$$

Applying Eq. (6.3) from Sec. 6.2,

$$\begin{aligned}\Delta\langle L_y\rangle &= \langle L_y\rangle_{sp} - \langle L_y\rangle_s \\ &= iu_{sp}^{-1}\int dx\, d\xi\, \Big[|A_s|^2|\Gamma|^2 L_y\Delta\phi_p \\ &\quad + |A_s|^2\left(|\Gamma|^2 - \frac{u_{sp}}{u_s}\right)L_y\phi_s\Big],\end{aligned} \tag{C14}$$

yields a change in transverse OAM per photon

$$\Delta\langle L_y\rangle_G = \frac{8\Delta\phi_{p0}\bar{x}_0\bar{\xi}_0\eta_x\eta_\xi}{\sigma_x^3\sigma_\xi^3}\left(\alpha+\frac{\beta_2}{\alpha}\right)\exp\left(-\frac{2\bar{x}_0^2}{\sigma_x^2}-\frac{2\bar{\xi}_0^2}{\sigma_\xi^2}\right). \tag{C15}$$

Here $\alpha = w_{0\xi}/w_{0x}$, $\eta_x = h_x/w_{0x}$, $\eta_\xi = h_\xi/w_{0\xi}$, $\bar{x}_0 = x_0/w_{0x}$, $\bar{\xi}_0 = \xi_0/w_{0\xi}$, $\sigma_x = \sqrt{1+2h_x^2/w_{0x}^2}$ and $\sigma_\xi = \sqrt{1+2h_\xi^2/w_{0\xi}^2}$. Similarly, for a transverse OAM-carrying STOV pulse,

$$A_{STOV}(x,\xi) = \left(\frac{\xi}{w_{0\xi}} + i\frac{x}{w_{0x}}\right)A_G(x,\xi), \tag{C16}$$

we find

$$\begin{aligned}\Delta\langle L_y\rangle_{STOV} = {} & \Delta\phi_{p0}\frac{8\bar{x}_0\bar{\xi}_0\eta_x\eta_\xi}{\sigma_x^5\sigma_\xi^5}\left(\alpha+\frac{\beta_2}{\alpha}\right)\exp\left[-\frac{2\bar{x}_0^2}{\sigma_x^2}-\frac{2\bar{\xi}_0^2}{\sigma_\xi^2}\right] \\ & \times\left[\eta_x^2+\eta_\xi^2+8\eta_x^2\eta_\xi^2-1+2\frac{\sigma_\xi^2}{\sigma_x^2}\bar{x}_0^2+2\frac{\sigma_x^2}{\sigma_\xi^2}\bar{\xi}_0^2\right].\end{aligned} \tag{C17}$$

Figure C4 plots $\Delta\langle L_y\rangle_G$ and $\Delta\langle L_y\rangle_{STOV}$ vs. (x_0, ξ_0). Both the Gaussian and STOV plots exhibit a 4-lobed structure with respect to spatiotemporal centre of energy.

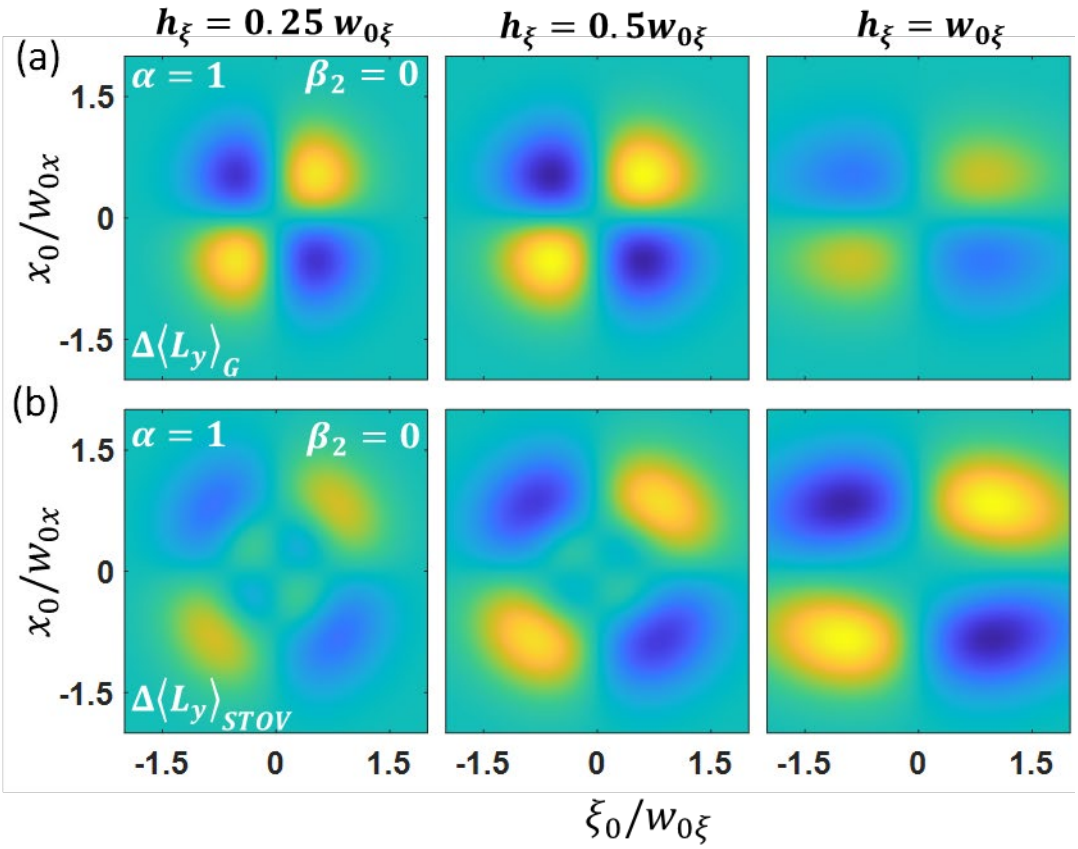

Figure C4. (a) $\Delta\langle L_y\rangle_G$ from Eq. (C15); (b) $\Delta\langle L_y\rangle_{STOV}$ from Eq. (C17). For the Gaussian phase perturbation $\Gamma(x,\xi) = \exp(i\Delta\phi_p(x,\xi)$, where $\Delta\phi_p(x,\xi) = \Delta\phi_{p0}\exp(-(x-x_0)^2/h_x^2 - (\xi-\xi_0)^2/h_\xi^2)$. Here, $h_x = 0.25w_{0x}$, $\beta_2 = 0$, and $\alpha = w_{0\xi}/w_{0x} = 1$.

C.8 Spatiotemporal Amplitude Perturbations localized in time and space

Now, we consider the non-energy-conserving amplitude perturbation $\Gamma(x,\xi) = 1 - \Gamma_0\exp\left(-(x-x_0)^2/h_x^2 - (\xi-\xi_0)^2/h_\xi^2\right)$ centred at (x_0,ξ_0). Applying this perturbation to a Gaussian pulse, with $\phi_s = \text{const}$, yields $\Delta\langle L_y\rangle = 0$. However, for pulses already carrying a spatiotemporal phase, an analytic result such as Eq. (C17) is difficult. Figure C5(a) plots a numerical calculation of $\Delta\langle L_y\rangle_{\text{STOV}}$, as a function of

perturbation location (x_0, ξ_0), for the $l = 1$ STOV pulse of Eq. (3.5b), with $w_{0x} = w_{0\xi} = 1$, $h_x = h_\xi = 0.25w_{0x}$, and $\Gamma_0 = 1$. The dashed red circle is the spatiotemporal location of pulse peak intensity. Figure C5(b), shows the change in OAM from a non-transient amplitude perturbation ($h_\xi \to \infty$). Note that for $h_\xi = 0.25w_{0\xi}$, $|\Delta\langle L_y\rangle| =$

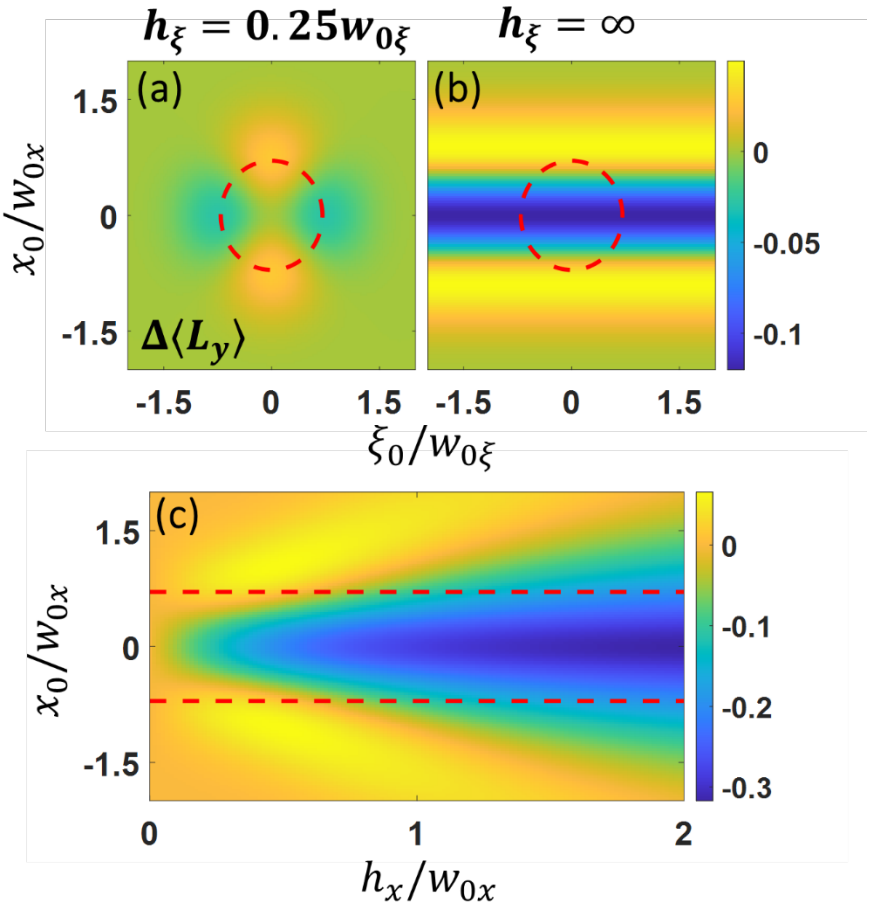

Figure C5. (a) Plot of $\Delta\langle L_y\rangle_{\mathrm{STOV}}$ from the amplitude perturbation $\Gamma(x,\xi) = 1 - \Gamma_0 \exp\left(-(x-x_0)^2/h_x^2 - (\xi-\xi_0)^2/h_\xi^2\right)$, with $w_{0x} = w_{0\xi} = 1$, $h_x = h_\xi = 0.25w_{0x}$, and $\Gamma_0 = 1$. (b) Same as (a) except for $h_\xi \to \infty$. **(c)** Plot of $\Delta\langle L_y\rangle_{\mathrm{STOV}}$ as a function of h_x for $w_{0x} = w_{0\xi} = 1$, $\Gamma_0 = 1$, and $h_\xi \to \infty$. The dashed red lines denote the contour of peak intensity of $A_{\mathrm{STOV}}(x,\xi)$.

0.028, while for the case $h_\xi \to \infty$, $\left|\Delta\langle L_y\rangle\right| = 0.12$, as more energy is removed by the perturbation. It is also interesting that the 4-lobed structure from the amplitude perturbation is complementary to that of the Gaussian phase perturbations in Fig. C4. Figure C5(c) examines how the change in OAM varies with h_x for $h_\xi = \infty$, where we see that outside of the contour of peak intensity of the field, $\Delta\langle L_y\rangle$ can be slightly positive while inside the peak intensity contour $\Delta\langle L_y\rangle$ only decreases as h_x increases.

Chapter 7: Conclusion and Future Work

7.1 Summary and Conclusion

Over the course of this dissertation, we have demonstrated a new pulse characterization technique (TG-SSSI) for measuring spatiotemporally structured light (Chapter 2). In Chapter 3, the mode structure of STOVs was analyzed and a generalized formula for describing STOV modes (a new class of light states) was derived (spatiotemporal modes of integer azimuthal index) as well as the transverse OAM for these modes at a given azimuthal index, l and eccentricity, α. In vacuum, the transverse OAM of these states is given in integer multiples of $\alpha/2$ and in dispersive media, is quantized in integer multiples of $(\alpha - \beta_2/\alpha)/2$. In the later case, the OAM is shared between a photon and a STOV-polariton. We further demonstrated the linear generation using a $4f$ pulse shaper and free-space propagation of STOVs in Chapter 4 by measuring the near-field and far-field outputs of the pulse shaper using either a π-step phase plate or a spiral phase plate. The behavior of STOVs undergoing SHG and the corresponding conservation of OAM was simulated and experimentally demonstrated in Chapter 5 where it was also shown that transverse OAM is carried at the per photon level. Finally, in Chapter 6 we examined the effects of transient spatiotemporal perturbations of STOVs and pulsed lasers envelopes in general, revealing the robustness of transverse OAM carried by laser pulses for perturbations much longer than the temporal scale width of the pulse. This chapter also demonstrated the rich dynamics of transverse OAM in pulsed light and further showed that a phase winding is not necessary for a

pulse to carry transverse OAM just as in Chapter 3 it was shown that a phase winding in the spatiotemporal domain may not necessarily correspond to a pulse carrying transverse OAM.

7.2 Nonlinear Propagation Measurements Using TG-SSSI

To our knowledge, direct study of nonlinearly propagating ultrashort laser pulses (filamentation) has been restricted to methods that do not directly measure the spatiotemporal domain. TG-SSSI is well positioned to fill this gap, since it is capable of single-shot measurements in the spatiotemporal domain. While the supercontinuum generated during filamentation could potentially interfere with the supercontinuum probe and reference, this problem could easily be mitigated by making the measurement non-colinear or by restricting the imaging to the bandwidth of the initial pulse.

For diffuse media (air), we are still interested in measuring STOV formation of filaments and their post formation behavior. Instead of varying the thickness of a solid target we now can vary the thickness of a gaseous target by imposing an interface where the nonlinear refractive index drops off steeply through the use of a helium cell as was used in the first observations of STOVs [24], air waveguide experiments [9] and droplet/aerosol clearing experiments [133].

7.3 STOV Polariton

The STOV-polariton predicted in Chapter 3 presents an intriguing avenue for future research. While it is likely that the STOV-polariton is carried by the linear dielectric response of dispersive media, a more thorough theoretical treatment is needed to better guide future experimental investigations.

List of publications by the candidate

1. **S. W. Hancock**, S. Zahedpour, A. Goffin, and H. M. Milchberg, "Free-space propagation of spatiotemporal optical vortices," Optica **12**, 1547 (2019).

2. **S. W. Hancock**, S. Zahedpour, and H. M. Milchberg, "Transient-grating single-shot supercontinuum spectral interferometry (TG-SSSI)," Opt. Lett. **46**, 1013 (2021).

3. **S. W. Hancock**, S. Zahedpour, and H. M. Milchberg, "Second-harmonic generation of spatiotemporal optical vortices and conservation of orbital angular momentum," Optica **8**, 594 (2021).

4. **S. W. Hancock**, S. Zahedpour, and H. M. Milchberg, "Mode Structure and Orbital Angular Momentum of Spatiotemporal Optical Vortex Pulses," Phys. Rev. Lett. **127**, 193901 (2021).

5. S. Zahedpour, **S. W. Hancock**, and H. M. Milchberg, "Ultrashort infrared 2.5–11 μm pulses: spatiotemporal profiles and absolute nonlinear response of air constituents," Opt. Lett. **44**, 843 (2019).

6. D. Patel, D. Jang, **S. W. Hancock**, H. M. Milchberg, and K.-Y. Kim, "Simplified single-shot supercontinuum spectral interferometry," Optics express **28**, 11023 (2020).

7. K. Y. Bliokh, E. Karimi, M. J. Padgett, M. A. Alonso, M. R. Dennis, A. Dudley, A. Forbes, S. Zahedpour, **S. W. Hancock**, H. M. Milchberg, S. Rotter, F. Nori, Ş. K. Özdemir, N. Bender, H. Cao, P. B. Corkum, C. Hernández-García, H. Ren, Y. Kivshar, M. G. Silveirinha, N. Engheta, A. Rauschenbeutel, P. Schneeweiss, J. Volz, D. Leykam, D. A. Smirnova, K. Rong, B. Wang, E. Hasman, M. F. Picardi, A. V. Zayats, F. J. Rodríguez-Fortuño, C. Yang, J. Ren, A. B. Khanikaev, A. Alù, E. Brasselet, M. Shats, J. Verbeeck, P. Schattschneider, D. Sarenac, D. G. Cory, D. Pushin, M. Birk, A. Gorlach, I. Kaminer, F. Cardano, L. Marrucci, M. Krenn, and F. Marquardt, "Roadmap on structured waves," arXiv:2301.05349 (2023).

8. **S. W. Hancock**, S. Zahedpour, A. Goffin, and H. M. Milchberg, "Spatio-temporal optical vortex (STOV) pulses," Proc. SPIE **12436**, 1243605 (2023).

9. **S. W. Hancock**, S. Zahedpour, A. Goffin, and H. M. Milchberg, "Spatiotemporal torquing of light," arXiv preprint arXiv:2307:01019 (2023).

Bibliography

1. L. Allen, M. W. Beijersbergen, R. J. C. Spreeuw, and J. P. Woerdman, "Orbital angular momentum of light and the transformation of Laguerre-Gaussian laser modes," Phys. Rev. A **45**, 8185 (1992).
2. M. Musigmann and J. Jahns, "Refractive–diffractive generation of ultrashort Airy–Bessel wave packets with orbital angular momentum: a comprehensive analysis," J. Opt. Soc. Am. B, JOSAB **33**, 574–582 (2016).
3. N. Papasimakis, T. Raybould, V. A. Fedotov, D. P. Tsai, I. Youngs, and N. I. Zheludev, "Pulse generation scheme for flying electromagnetic doughnuts," Phys. Rev. B **97**, 201409 (2018).
4. A. Vinçotte and L. Bergé, "Femtosecond Optical Vortices in Air," Phys. Rev. Lett. **95**, 193901 (2005).
5. H. He, M. E. J. Friese, N. R. Heckenberg, and H. Rubinsztein-Dunlop, "Direct Observation of Transfer of Angular Momentum to Absorptive Particles from a Laser Beam with a Phase Singularity," Phys. Rev. Lett. **75**, 826–829 (1995).
6. V. Bobkova, J. Stegemann, R. Droop, E. Otte, and C. Denz, "Optical grinder: sorting of trapped particles by orbital angular momentum," Opt. Express, OE **29**, 12967–12975 (2021).
7. Y. Yang, Y. Ren, M. Chen, Y. Arita, and C. Rosales-Guzmán, "Optical trapping with structured light: a review," AP **3**, 034001 (2021).
8. B. M. Heffernan, S. A. Meyer, D. Restrepo, M. E. Siemens, E. A. Gibson, and J. T. Gopinath, "A Fiber-Coupled Stimulated Emission Depletion Microscope for Bend-Insensitive Through-Fiber Imaging," Sci Rep **9**, 11137 (2019).
9. A. Goffin, I. Larkin, A. Tartaro, A. Schweinsberg, A. Valenzuela, E. W. Rosenthal, and H. M. Milchberg, "Optical Guiding in 50-Meter-Scale Air Waveguides," Phys. Rev. X **13**, 011006 (2023).
10. B. Miao, J. E. Shrock, L. Feder, R. C. Hollinger, J. Morrison, R. Nedbailo, A. Picksley, H. Song, S. Wang, J. J. Rocca, and H. M. Milchberg, "Multi-GeV Electron Bunches from an All-Optical Laser Wakefield Accelerator," Phys. Rev. X **12**, 031038 (2022).
11. G. A. Tyler and R. W. Boyd, "Influence of atmospheric turbulence on the propagation of quantum states of light carrying orbital angular momentum," Opt. Lett., OL **34**, 142–144 (2009).
12. T. Doster and A. T. Watnik, "Laguerre–Gauss and Bessel–Gauss beams propagation through turbulence: analysis of channel efficiency," Appl. Opt., AO **55**, 10239–10246 (2016).

13. C. Paterson, "Atmospheric Turbulence and Orbital Angular Momentum of Single Photons for Optical Communication," Phys. Rev. Lett. **94**, 153901 (2005).

14. A. E. Willner, K. Pang, H. Song, K. Zou, and H. Zhou, "Orbital angular momentum of light for communications," Applied Physics Reviews **8**, 041312 (2021).

15. G. Vallone, V. D'Ambrosio, A. Sponselli, S. Slussarenko, L. Marrucci, F. Sciarrino, and P. Villoresi, "Free-Space Quantum Key Distribution by Rotation-Invariant Twisted Photons," Phys. Rev. Lett. **113**, 060503 (2014).

16. M. Erhard, R. Fickler, M. Krenn, and A. Zeilinger, "Twisted photons: new quantum perspectives in high dimensions," Light Sci Appl **7**, 17146–17146 (2018).

17. J. Luís Martins, J. Vieira, J. Ferri, and T. Fülöp, "Radiation emission in laser-wakefields driven by structured laser pulses with orbital angular momentum," Sci Rep **9**, 9840 (2019).

18. K. O'Holleran, M. J. Padgett, and M. R. Dennis, "Topology of optical vortex lines formed by the interference of three, four, and five plane waves," Opt. Express, OE **14**, 3039–3044 (2006).

19. B. Miao, L. Feder, J. E. Shrock, A. Goffin, and H. M. Milchberg, "Optical Guiding in Meter-Scale Plasma Waveguides," Phys. Rev. Lett. **125**, 074801 (2020).

20. A. Longman and R. Fedosejevs, "Kilo-Tesla axial magnetic field generation with high intensity spin and orbital angular momentum beams," Phys. Rev. Res. **3**, 043180 (2021).

21. M. A. Porras, "Upper bound to the orbital angular momentum carried by an ultrashort pulse," Phys. Rev. Lett. **122**, 123904 (2019).

22. V. Denisenko, V. Shvedov, A. S. Desyatnikov, D. N. Neshev, W. Krolikowski, A. Volyar, M. Soskin, and Y. S. Kivshar, "Determination of topological charges of polychromatic optical vortices," Opt. Express, OE **17**, 23374–23379 (2009).

23. A. Richter, M. Bock, J. Jahns, and R. Grunwald, "Orbital angular momentum experiments with broadband few cycle pulses," in *Complex Light and Optical Forces IV* (SPIE, 2010), Vol. 7613, pp. 63–71.

24. N. Jhajj, I. Larkin, E. W. Rosenthal, S. Zahedpour, J. K. Wahlstrand, and H. M. Milchberg, "Spatiotemporal optical vortices," Phys. Rev. X **6**, 031037 (2016).

25. M. Le, G. A. Hine, and H. M. Milchberg, "Spatiotemporal optical vortices (STOVs) and relativistic optical guiding," in *Bulletin of the American Physical Society* (American Physical Society, n.d.).

26. N. Jhajj, "Hydrodynamic and electrodynamic implications of optical femtosecond filamentation," University of Maryland, College Park (2017).

27. S. W. Hancock, S. Zahedpour, A. Goffin, and H. M. Milchberg, "Free-space propagation of spatiotemporal optical vortices," Optica **6**, 1547–1553 (2019).

28. S. W. Hancock, S. Zahedpour, and H. M. Milchberg, "Transient-grating single-shot supercontinuum spectral interferometry (TG-SSSI)," Opt. Lett. **46**, 1013–1016 (2021).

29. A. Chong, C. Wan, J. Chen, and Q. Zhan, "Generation of spatiotemporal optical vortices with controllable transverse orbital angular momentum," Nat. Photonics **14**, 350–354 (2020).

30. S. W. Hancock, S. Zahedpour, and H. M. Milchberg, "Mode Structure and Orbital Angular Momentum of Spatiotemporal Optical Vortex Pulses," Phys. Rev. Lett. **127**, 193901 (2021).

31. S. W. Hancock, S. Zahedpour, and H. M. Milchberg, "Second-harmonic generation of spatiotemporal optical vortices and conservation of orbital angular momentum," Optica **8**, 594–597 (2021).

32. J. D. Jackson, *Classical Electrodynamics* (John Wiley & Sons, 2021).

33. M. W. Beijersbergen, R. P. C. Coerwinkel, M. Kristensen, and J. P. Woerdman, "Helical-wavefront laser beams produced with a spiral phaseplate," Optics Communications **112**, 321–327 (1994).

34. J. F. Nye, M. V. Berry, and F. C. Frank, "Dislocations in wave trains," Proceedings of the Royal Society of London. A. Mathematical and Physical Sciences **336**, 165–190 (1997).

35. I. Kimel and L. R. Elias, "Relations between Hermite and Laguerre Gaussian modes," IEEE Journal of Quantum Electronics **29**, 2562–2567 (1993).

36. P. A. Franken, A. E. Hill, C. W. Peters, and G. Weinreich, "Generation of Optical Harmonics," Physical Review Letters **7**, 118 (1961).

37. K. Dholakia, N. B. Simpson, M. J. Padgett, and L. Allen, "Second-harmonic generation and the orbital angular momentum of light," Phys. Rev. A **54**, R3742–R3745 (1996).

38. J. Courtial, K. Dholakia, L. Allen, and M. J. Padgett, "Second-harmonic generation and the conservation of orbital angular momentum with high-order Laguerre-Gaussian modes," Phys. Rev. A **56**, 4193–4196 (1997).

39. A. Nahata and T. F. Heinz, "Generation of subpicosecond electrical pulses by optical rectification," Opt. Lett., OL **23**, 867–869 (1998).

40. K. H. Yang, P. L. Richards, and Y. R. Shen, "Generation of Far-Infrared Radiation by Picosecond Light Pulses in LiNbO3," Appl. Phys. Lett. **19**, 320–323 (1971).

41. M. Bass, P. A. Franken, J. F. Ward, and G. Weinreich, "Optical Rectification," Phys. Rev. Lett. **9**, 446–448 (1962).

42. G. Cerullo and S. De Silvestri, "Ultrafast optical parametric amplifiers," Review of Scientific Instruments **74**, 1–18 (2003).

43. K. Kaneshima, N. Ishii, K. Takeuchi, and J. Itatani, "Generation of carrier-envelope phase-stable mid-infrared pulses via dual-wavelength optical parametric amplification," Opt. Express, OE **24**, 8660–8665 (2016).

44. R. Baumgartner and R. Byer, "Optical parametric amplification," IEEE Journal of Quantum Electronics **15**, 432–444 (1979).

45. J. M. Manley and H. E. Rowe, "Some General Properties of Nonlinear Elements-Part I. General Energy Relations," Proceedings of the IRE **44**, 904–913 (1956).

46. L. Bergé, S. Skupin, R. Nuter, J. Kasparian, and J.-P. Wolf, "Ultrashort filaments of light in weakly ionized, optically transparent media," Rep. Prog. Phys. **70**, 1633 (2007).

47. A. Couairon and A. Mysyrowicz, "Femtosecond filamentation in transparent media," Physics Reports **441**, 47–189 (2007).

48. *The Supercontinuum Laser Source* (n.d.).

49. K. Y. Kim, I. Alexeev, and H. M. Milchberg, "Single-shot supercontinuum spectral interferometry," Appl. Phys. Lett. **81**, 4124–4126 (2002).

50. C. Kolmeder, W. Zinth, and W. Kaiser, "Second harmonic beam analysis, a sensitive technique to determine the duration of single ultrashort laser pulses," Optics Communications **30**, 453–457 (1979).

51. K. W. DeLong, R. Trebino, J. Hunter, and W. E. White, "Frequency-resolved optical gating with the use of second-harmonic generation," J. Opt. Soc. Am. B **11**, 2206–2215 (1994).

52. C. Iaconis and I. A. Walmsley, "Spectral phase interferometry for direct electric-field reconstruction of ultrashort optical pulses," Opt. Lett. **23**, 792–794 (1998).

53. J. K. Wahlstrand, S. Zahedpour, Y.-H. Cheng, J. P. Palastro, and H. M. Milchberg, "Absolute measurement of the ultrafast nonlinear electronic and rovibrational response in H 2 and D 2," Phys. Rev. A **92**, 063828 (2015).

54. J. K. Wahlstrand, S. Zahedpour, A. Bahl, M. Kolesik, and H. M. Milchberg, "Bound-electron nonlinearity beyond the ionization threshold," Phys. Rev. Lett. **120**, 183901 (2018).

55. S. Zahedpour, J. K. Wahlstrand, and H. M. Milchberg, "Measurement of the nonlinear refractive index of air constituents at mid-infrared wavelengths," Opt. Lett., OL **40**, 5794–5797 (2015).

56. S. Zahedpour, S. W. Hancock, and H. M. Milchberg, "Ultrashort infrared 2.5–11 μm pulses: spatiotemporal profiles and absolute nonlinear response of air constituents," Opt. Lett. **44**, 843–846 (2019).

57. S. Zahedpour, S. W. Hancock, and H. M. Milchberg, "Direct Measurement of Linearly Imposed Spatiotemporal Optical Vortices (STOVs)," in *Frontiers in Optics + Laser Science APS/DLS (2019), Paper FW5F.5* (Optical Society of America, 2019), p. FW5F.5.

58. J. K. Wahlstrand, S. Zahedpour, and H. M. Milchberg, "Optimizing the time resolution of supercontinuum spectral interferometry," J. Opt. Soc. Am. B **33**, 1476–1481 (2016).

59. D. Patel, D. Jang, S. W. Hancock, H. M. Milchberg, and K.-Y. Kim, "Simplified single-shot supercontinuum spectral interferometry," Opt. Express **28**, 11023–11032 (2020).

60. F. Salin, P. Georges, G. Roger, and A. Brun, "Single-shot measurement of a 52-fs pulse," Appl. Opt. **26**, 4528–4531 (1987).

61. R. Trebino and D. J. Kane, "Using phase retrieval to measure the intensity and phase of ultrashort pulses: frequency-resolved optical gating," J. Opt. Soc. Am. A **10**, 1101–1111 (1993).

62. D. J. Kane and R. Trebino, "Single-shot measurement of the intensity and phase of an arbitrary ultrashort pulse by using frequency-resolved optical gating," Opt. Lett. **18**, 823–825 (1993).

63. J. N. Sweetser, D. N. Fittinghoff, and R. Trebino, "Transient-grating frequency-resolved optical gating," Opt. Lett. **22**, 519–521 (1997).

64. P. O'Shea, M. Kimmel, X. Gu, and R. Trebino, "Highly simplified device for ultrashort-pulse measurement," Opt. Lett. **26**, 932–934 (2001).

65. P. Baum, S. Lochbrunner, and E. Riedle, "Zero-additional-phase SPIDER: full characterization of visible and sub-20-fs ultraviolet pulses," Opt. Lett. **29**, 210–212 (2004).

66. M. Hirasawa, N. Nakagawa, K. Yamamoto, R. Morita, H. Shigekawa, and M. Yamashita, "Sensitivity improvement of spectral phase interferometry for direct electric-field reconstruction for the characterization of low-intensity femtosecond pulses," Appl. Opt. B **74**, s225–s229 (2002).

67. C. Dorrer, P. Londero, and I. A. Walmsley, "Homodyne detection in spectral phase interferometry for direct electric-field reconstruction," Opt. Lett. **26**, 1510–1512 (2001).

68. A. Monmayrant, M. Joffre, T. Oksenhendler, R. Herzog, D. Kaplan, and P. Tournois, "Time-domain interferometry for direct electric-field reconstruction by use of an acousto-optic programmable filter and a two-photon detector," Opt. Lett. **28**, 278–280 (2003).

69. E. M. Kosik, A. S. Radunsky, I. A. Walmsley, and C. Dorrer, "Interferometric technique for measuring broadband ultrashort pulses at the sampling limit," Opt. Lett. **30**, 326–328 (2005).

70. Z. Guang, M. Rhodes, M. Davis, and R. Trebino, "Complete characterization of a spatiotemporally complex pulse by an improved single-frame pulse-measurement technique," J. Opt. Soc. Am. B **31**, 2736–2743 (2014).

71. M. Louisy, C. Guo, L. Neoričić, S. Zhong, A. L'Huillier, C. L. Arnold, and M. Miranda, "Compact single-shot d-scan setup for the characterization of few-cycle laser pulses," Appl. Opt. **56**, 9084–9089 (2017).

72. S. P. Le Blanc, E. W. Gaul, N. H. Matlis, A. Rundquist, and M. C. Downer, "Single-shot measurement of temporal phase shifts by frequency-domain holography," Opt. Lett. **25**, 764–766 (2000).

73. J. P. Geindre, P. Audebert, A. Rousse, F. Fallies, J. C. Gauthier, A. Mysyrowicz, A. Dos Santos, G. Hamoniaux, and A. Antonetti, "Frequency-domain interferometer for measuring the phase and amplitude of a femtosecond pulse probing a laser-produced plasma," Opt. Lett. **19**, 1997–1999 (1994).

74. Y.-H. Chen, S. Varma, A. York, and H. M. Milchberg, "Single-shot, space-and time-resolved measurement of rotational wavepacket revivals in H 2, D 2, N 2, O 2, and N 2 O," Opt. Express **15**, 11341–11357 (2007).

75. L. Marrucci, C. Manzo, and D. Paparo, "Optical spin-to-orbital angular momentum conversion in inhomogeneous anisotropic media," Phys. Rev. Lett. **96**, 163905 (2006).

76. S. Carbajo, E. Granados, D. Schimpf, A. Sell, K.-H. Hong, J. Moses, and F. X. Kärtner, "Efficient generation of ultra-intense few-cycle radially polarized laser pulses," Opt. Lett. **39**, 2487–2490 (2014).

77. J. P. Heritage, R. N. Thurston, W. J. Tomlinson, A. M. Weiner, and R. H. Stolen, "Spectral windowing of frequency-modulated optical pulses in a grating compressor," Appl. Phys. Lett. **47**, 87–89 (1985).

78. A. M. Weiner, J. P. Heritage, and E. M. Kirschner, "High-resolution femtosecond pulse shaping," J. Opt. Soc. Am. B, JOSAB **5**, 1563–1572 (1988).

79. A. M. Weiner and D. E. Leaird, "Generation of terahertz-rate trains of femtosecond pulses by phase-only filtering," Opt. Lett., OL **15**, 51–53 (1990).

80. M. Takeda, H. Ina, and S. Kobayashi, "Fourier-transform method of fringe-pattern analysis for computer-based topography and interferometry," J. Opt. Soc. Am., JOSA **72**, 156–160 (1982).

81. A. M. Weiner, "Femtosecond optical pulse shaping and processing," Progress in Quantum Electronics **19**, 161–237 (1995).

82. W. R. Klein and B. D. Cook, "Unified Approach to Ultrasonic Light Diffraction," IEEE Transactions on Sonics and Ultrasonics **14**, 123–134 (1967).

83. A. Couairon, E. Brambilla, T. Corti, D. Majus, O. de J. Ramírez-Góngora, and M. Kolesik, "Practitioner's guide to laser pulse propagation models and simulation," Eur. Phys. J. Spec. Top. **199**, 5–76 (2011).

84. M. Kolesik and J. V. Moloney, "Nonlinear optical pulse propagation simulation: From Maxwell's to unidirectional equations," Phys. Rev. E **70**, 036604 (2004).

85. A. P. Sukhorukov and V. V. Yangirova, "Spatio-temporal vortices: properties, generation and recording," in (2005), Vol. 5949.

86. K. Y. Bliokh and F. Nori, "Spatiotemporal vortex beams and angular momentum," Phys. Rev. A **86**, 033824 (2012).

87. K. Y. Bliokh, "Spatiotemporal Vortex Pulses: Angular Momenta and Spin-Orbit Interaction," Phys. Rev. Lett. **126**, 243601 (2021).

88. A. Lotti, A. Couairon, D. Faccio, and P. Di Trapani, "Energy-flux characterization of conical and space-time coupled wave packets," Phys. Rev. A **81**, 023810 (2010).

89. C. F. Klingshirn, *Semiconductor Optics* (Springer Science & Business Media, 2012).

90. M. J. Gullans, J. D. Thompson, Y. Wang, Q.-Y. Liang, V. Vuletić, M. D. Lukin, and A. V. Gorshkov, "Effective field theory for Rydberg polaritons," Phys. Rev. Lett. **117**, 113601 (2016).

91. G. Nienhuis and L. Allen, "Paraxial wave optics and harmonic oscillators," Phys. Rev. A **48**, 656 (1993).

92. W. N. Plick, M. Krenn, R. Fickler, S. Ramelow, and A. Zeilinger, "Quantum orbital angular momentum of elliptically symmetric light," Phys. Rev. A **87**, 033806 (2013).

93. A. Couairon and A. Mysyrowicz, "Femtosecond filamentation in transparent media," Physics Reports **441**, 47–189 (2007).

94. P. Sprangle, C.-M. Tang, and E. Esarey, "Relativistic Self-Focusing of Short-Pulse Radiation Beams in Plasmas," IEEE Transactions on Plasma Science **15**, 145–153 (1987).

95. F. Salehi, A. J. Goers, G. A. Hine, L. Feder, D. Kuk, B. Miao, D. Woodbury, K. Y. Kim, and H. M. Milchberg, "MeV electron acceleration at 1 kHz with <10 mJ laser pulses," Opt. Lett., OL **42**, 215–218 (2017).

96. J. K. Wahlstrand, Y.-H. Cheng, and H. M. Milchberg, "Absolute measurement of the transient optical nonlinearity in N${}_{2}$, O${}_{2}$, N${}_{2}$O, and Ar," Phys. Rev. A **85**, 043820 (2012).

97. D. Faccio, A. Lotti, A. Matijosius, F. Bragheri, V. Degiorgio, A. Couairon, and P. D. Trapani, "Experimental energy-density flux characterization of ultrashort laser pulse filaments," Opt. Express, OE **17**, 8193–8200 (2009).

98. J. K. Wahlstrand, S. Zahedpour, and H. M. Milchberg, "Optimizing the time resolution of supercontinuum spectral interferometry," J. Opt. Soc. Am. B, JOSAB **33**, 1476–1481 (2016).

99. D. Jang, R. M. Schwartz, D. Woodbury, J. Griff-McMahon, A. H. Younis, H. M. Milchberg, and K.-Y. Kim, "Efficient terahertz and Brunel harmonic generation from air plasma via mid-infrared coherent control," Optica, OPTICA **6**, 1338–1341 (2019).

100. M. S. Soskin, V. N. Gorshkov, M. V. Vasnetsov, J. T. Malos, and N. R. Heckenberg, "Topological charge and angular momentum of light beams carrying optical vortices," Phys. Rev. A **56**, 4064–4075 (1997).

101. J. Courtial, K. Dholakia, L. Allen, and M. J. Padgett, "Second-harmonic generation and the conservation of orbital angular momentum with high-order Laguerre-Gaussian modes," Phys. Rev. A **56**, 4193–4196 (1997).

102. X. Fang, Z. Kuang, P. Chen, H. Yang, Q. Li, W. Hu, Y. Lu, Y. Zhang, and M. Xiao, "Examining second-harmonic generation of high-order Laguerre–Gaussian modes through a single cylindrical lens," Opt. Lett., OL **42**, 4387–4390 (2017).

103. V. Belyi, N. A. Khilo, N. S. Kazak, A. A. Ryzhevich, and A. Forbes, "Propagation of high-order circularly polarized Bessel beams and vortex generation in uniaxial," OE **50**, 059001 (2011).

104. K. Dai, W. Li, K. S. Morgan, Y. Li, J. K. Miller, R. J. Watkins, and E. G. Johnson, "Second-harmonic generation of asymmetric Bessel-Gaussian beams carrying orbital angular momentum," Opt. Express, OE **28**, 2536–2546 (2020).

105. R. Ni, Y. F. Niu, L. Du, X. P. Hu, Y. Zhang, and S. N. Zhu, "Topological charge transfer in frequency doubling of fractional orbital angular momentum state," Appl. Phys. Lett. **109**, 151103 (2016).

106. Y. Li, Z.-Y. Zhou, D.-S. Ding, and B.-S. Shi, "Sum frequency generation with two orbital angular momentum carrying laser beams," J. Opt. Soc. Am. B, JOSAB **32**, 407–411 (2015).

107. G. Gariepy, J. Leach, K. T. Kim, T. J. Hammond, E. Frumker, R. W. Boyd, and P. B. Corkum, "Creating High-Harmonic Beams with Controlled Orbital Angular Momentum," Phys. Rev. Lett. **113**, 153901 (2014).

108. S. Li, B. Shen, X. Zhang, Z. Bu, and W. Gong, "Conservation of orbital angular momentum for high harmonic generation of fractional vortex beams," Opt. Express, OE **26**, 23460–23470 (2018).

109. F. Kong, C. Zhang, F. Bouchard, Z. Li, G. G. Brown, D. H. Ko, T. J. Hammond, L. Arissian, R. W. Boyd, E. Karimi, and P. B. Corkum, "Controlling the orbital angular momentum of high harmonic vortices," Nat Commun **8**, 14970 (2017).

110. D. Gauthier, P. R. Ribič, G. Adhikary, A. Camper, C. Chappuis, R. Cucini, L. F. DiMauro, G. Dovillaire, F. Frassetto, R. Géneaux, P. Miotti, L. Poletto, B. Ressel, C. Spezzani, M. Stupar, T. Ruchon, and G. De Ninno, "Tunable orbital angular momentum in high-harmonic generation," Nat Commun **8**, 14971 (2017).

111. S. W. Hancock, S. Zahedpour, and H. M. Milchberg, "Orbital angular momentum conservation in second-harmonic generation with spatiotemporal optical vortices," in *Frontiers in Optics / Laser Science (2020), Paper FM7C.6* (Optical Society of America, 2020), p. FM7C.6.

112. S. W. Hancock, S. Zahedpour, and H. M. Milchberg, "Second-Harmonic Generation of Spatiotemporal Optical Vortices," in *OSA High-Brightness Sources and Light-Driven Interactions Congress 2020 (EUVXRAY, HILAS, MICS) (2020), Paper JM3A.21* (Optical Society of America, 2020), p. JM3A.21.

113. G. Gui, N. J. Brooks, H. C. Kapteyn, M. M. Murnane, and C.-T. Liao, "Second-harmonic generation and the conservation of spatiotemporal orbital angular momentum of light," Nat. Photon. **15**, 608–613 (2021).

114. Z.-Y. Chen, R. Hu, S. Zhang, and T. Yuan, "Relativistic high-order harmonic generation of spatiotemporal optical vortices," Phys. Rev. A **106**, 013516 (2022).

115. R. W. Boyd, in *Nonlinear Optics*, 3rd ed. (n.d.), pp. 69–133.

116. D. Eimerl, L. Davis, S. Velsko, E. K. Graham, and A. Zalkin, "Optical, mechanical, and thermal properties of barium borate," Journal of Applied Physics **62**, 1968–1983 (1987).

117. M. J. Dodge, "Refractive properties of magnesium fluoride," Appl. Opt. **23**, 1980 (1984).

118. R. C. Eckardt, H. Masuda, Y. X. Fan, and R. L. Byer, "Absolute and relative nonlinear optical coefficients of KDP, KD*P, BaB/sub 2/O/sub 4/, LiIO/sub 3/, MgO:LiNbO/sub 3/, and KTP measured by phase-matched second-harmonic generation," IEEE Journal of Quantum Electronics **26**, 922–933 (1990).

119. Y. Toda, S. Honda, and R. Morita, "Dynamics of a paired optical vortex generated by second-harmonic generation," Opt. Express, OE **18**, 17796–17804 (2010).

120. A. Weiner, "Effect of group velocity mismatch on the measurement of ultrashort optical pulses via second harmonic generation," IEEE Journal of Quantum Electronics **19**, 1276–1283 (1983).

121. H. Wang, C. Guo, W. Jin, A. Y. Song, and S. Fan, "Engineering arbitrarily oriented spatiotemporal optical vortices using transmission nodal lines," Optica, OPTICA **8**, 966–971 (2021).

122. J. Huang, J. Zhang, T. Zhu, and Z. Ruan, "Spatiotemporal Differentiators Generating Optical Vortices with Transverse Orbital Angular Momentum and Detecting Sharp Change of Pulse Envelope," Laser & Photonics Reviews **16**, 2100357 (2022).

123. L. L. Doskolovich, A. I. Kashapov, E. A. Bezus, and D. A. Bykov, "Spatiotemporal optical differentiation and vortex generation with metal-dielectric-metal multilayers," Phys. Rev. A **106**, 033523 (2022).

124. M. A. Porras, "Propagation of higher-order spatiotemporal vortices," Opt. Lett., OL **48**, 367–370 (2023).

125. K. Y. Bliokh, "Orbital angular momentum of optical, acoustic, and quantum-mechanical spatiotemporal vortex pulses," Phys. Rev. A **107**, L031501 (2023).

126. H. F. Elder and P. Sprangle, "Mode power spectrum for Laguerre–Gauss beams in Kolmogorov turbulence," Opt. Lett., OL **47**, 3447–3450 (2022).

127. S. M. Barnett, "Optical angular-momentum flux*," J. Opt. B: Quantum Semiclass. Opt. **4**, S7 (2001).

128. M. Panahi, R. Shomali, M. Mollabashi, and S. Rasouli, "Atmospheric coherence time measurement by four-aperture DIMM defocus velocity technique," Appl. Opt., AO **58**, 8673–8679 (2019).

129. S. W. Hancock, S. Zahedpour, A. Goffin, and H. M. Milchberg, "Spatio-temporal optical vortex (STOV) pulses," in *Complex Light and Optical Forces XVII* (SPIE, 2023), Vol. 12436, pp. 23–31.

130. A. S. Desyatnikov, D. Buccoliero, M. R. Dennis, and Y. S. Kivshar, "Spontaneous knotting of self-trapped waves," Sci Rep **2**, 771 (2012).

131. M. Mansuripur, "Spin and orbital angular momenta of electromagnetic waves in free space," Phys. Rev. A **84**, 033838 (2011).

132. L. Feder, B. Miao, J. E. Shrock, A. Goffin, and H. M. Milchberg, "Self-waveguiding of relativistic laser pulses in neutral gas channels," Phys. Rev. Res. **2**, 043173 (2020).

133. A. Goffin, J. Griff-McMahon, I. Larkin, and H. M. Milchberg, "Atmospheric Aerosol Clearing by Femtosecond Filaments," Phys. Rev. Appl. **18**, 014017 (2022).